National Technical University of Athens
School of Applied Mathematical and Physical Sciences

Department of Physics

Detection of Structural Alterations in Mammalian Tissues after Exposure to Proton Radiation

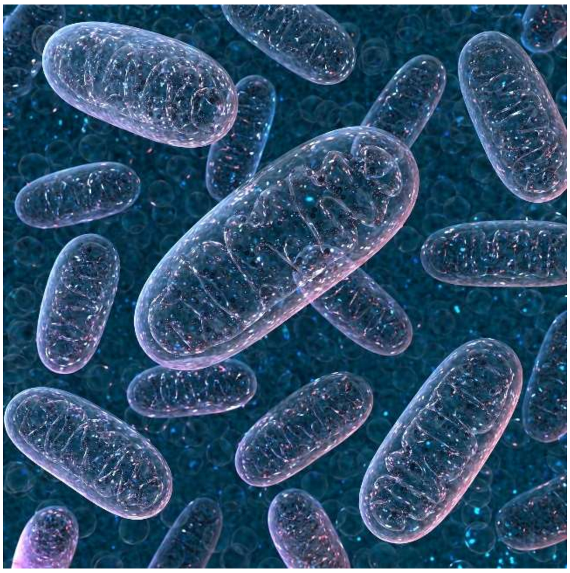

GRADUATE THESIS

FRAGKISKOS EMMANOUIL FYRIOS

Supervisor
Alexandros Georgakilas, Professor, NTUA

ATHENS 2024

ΕΘΝΙΚΟ ΜΕΤΣΟΒΙΟ ΠΟΛΥΤΕΧΝΕΙΟ

Σχολή Εφαρμοσμένων Μαθηματικών και Φυσικών Επιστημών

ΤΟΜΕΑΣ ΦΥΣΙΚΗΣ

Ανίχνευση Δομικών Αλλαγών σε Ιστούς Θηλαστικών ύστερα από Έκθεση σε Ακτινοβολία Πρωτονίων

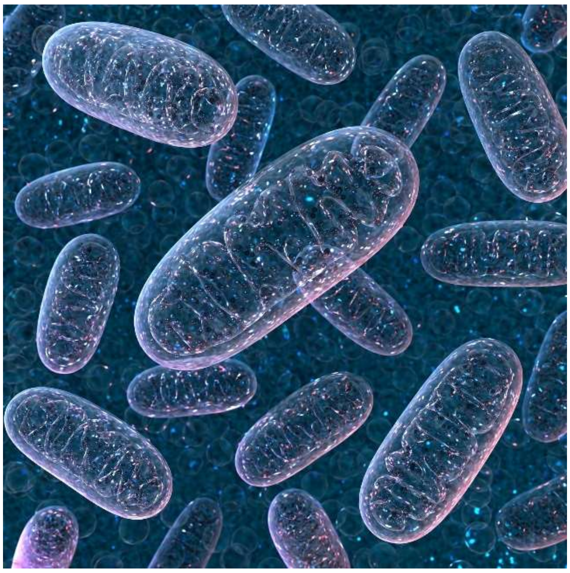

ΔΙΠΛΩΜΑΤΙΚΗ ΕΡΓΑΣΙΑ

ΦΡΑΓΚΙΣΚΟΣ ΕΜΜΑΝΟΥΗΛ ΦΥΡΙΟΣ

Επιβλέπων καθηγητής

Δρ. Αλέξανδρος Γεωργακίλας, Τομέας Φυσικής, ΕΜΠ

ΑΘΗΝΑ 2024

Acknowledgements

The present dissertation was elaborated in the Department of Physics of the School of Applied Mathematical and Physical Sciences, NTUA. Most of the work was conducted in collaboration with the Laboratory of Histology-Embryology, Medical School of the National Kapodistrian University of Athens with co-supervisors Assist. Prof. Sofia Havaki and Dr Ioanna Tremi, as well as with the Department of Radiation Oncology of the Perelman School of Medicine, University of Pennsylvania, Philadelphia, USA.

Thus, many people have contributed to the completion of this graduate thesis and I would like to acknowledge each one of them personally.

First and foremost, I am deeply appreciative of the assistance of my supervisor *Dr. Alexandros Georgakilas* for his support throughout all of my work. He is the one that guided me to select this interesting theme and encouraged me to apply my knowledge and acquire new skills in areas at the borderlines of physics, biology and computer science. Furthermore, he gave me the opportunity to come in contact with his collaborators from the University of Pennsylvania and, for this opening, I thank him a lot.

The present thesis would have never been completed without the precious help of *Dr. Sofia Havaki* and *Dr. Ioanna Tremi*, members of the Laboratory of the Histology and Embryology of the Medical School of Athens. I warmly thank them for educating me and patiently correcting me and answering my questions in matters of biology, morphometry and electron microscopy. I would also like to express my gratitude for sharing with me their great knowledge on the bibliography of the subjects as well as guiding me in every step of the writing process of the thesis. Their help, support and availability has been invaluable.

Many experiments mentioned in the context of this thesis were performed by the team of Dr. Koumenis at the Department of Radiation Oncology of UPenn. For this reason, I would like to thank Dr. Koumenis, Dr Michelle Kim, Dr Anastasia Velalopoulou and the whole research team for giving me the opportunity to be a part of their work.

I would also like to thank all of my professors during all the years of my academic course for their dedication and their love for their work. With their help, I managed to overcome any difficulties and approach the wonderful field of physics at its very essence. It is to their knowledge and guidance that I owe my current position as an applied physics graduate.

I would like to give special thanks to my friends and fellow students Vassilis Rangos, Iliani Papouli, Panagiotis Matsades, Mikela Almadi, Raphael Sevastopoulos, Georgia Tsoutsikou, Lydia Stainchaouer and Theotokis Plohoros. Besides their invaluable help in many scientific topics concerning our studies, they have been true inspiration for me. During the five years of our academic course, I was witnessing us grow and evolve together as scientists and personalities, complementing each other's deficiencies, overcoming obstacles and having a wonderful time. Without their presence, these five years would have been colorless and tedious.

Last but not least, I cannot express my gratitude towards my family for supporting me and encouraging me to not give up in the difficult situations. Their kindness and willingness to help me in every way possible made it feasible for me to focus on my studies without distractions and have a wonderful academic experience overall. I would also like to apologize to them, if sometimes I was too much focused…

Abstract

The use of ionizing radiation in cancer therapy has been a major medical achievement and radiotherapy has repeatedly been proven a promising tool for the clinical practice. However, important challenges, such as the protection of normal tissues surrounding the tumor, are yet to be overcome, urging for the advancement of the current radiotherapy techniques. Proton radiation has been noted for its beneficial biological effects, compared to electrons or X-rays, as it presents a sharp Bragg peak and therefore it can more effectively target the cancerous tumor. At the same time, there is multiple evidence suggesting that when radiation is delivered in ultra-high dose rates (FLASH), it tends to have additional protective benefits to normal tissues, compared to conventional dose rates. The precise effects that FLASH proton radiotherapy has on the normal tissues though, is still a field under research.

In the present thesis, the effects of FLASH proton radiotherapy on the mitochondria of healthy cells are investigated and compared with those of the conventional dose rate. For this purpose, TEM microscope images of the small intestinal tissue of rodents are analyzed. In addition, a machine learning algorithm is trained upon the image dataset, in order to perform segmentation of mitochondria out of unseen images of cells. Chapter one provides the necessary theoretical background in radiation physics, radiotherapy, biology and radiobiology, electron microscopy and machine learning. Chapter two presents the materials and methods used for the experiments, as well as the detailed approach followed for the analysis of the image data and the training of the segmentation model. In the third chapter, the results are presented and discussed, while the last chapter is a conclusion. Finally, two appendices are attached, for the result tables and the programming code.

Περίληψη

Η χρήση της ιοντίζουσας ακτινοβολίας στη θεραπεία του καρκίνου αποτελεί ένα σημαντικό ιατρικό επίτευγμα και η ακτινοθεραπεία έχει επανειλημμένα αποδειχθεί ένα πολλά υποσχόμενο εργαλείο για την κλινική πρακτική. Ωστόσο, σημαντικές προκλήσεις, όπως η προστασία των υγιών ιστών που περιβάλλουν τον όγκο, δεν έχουν ακόμη ξεπεραστεί, δημιουργώντας την ανάγκη για πρόοδο των σημερινών τεχνικών ακτινοθεραπείας. Η ακτινοβολία πρωτονίων έχει ιδιαίτερα ευεργετικές βιολογικές επιδράσεις, σε σύγκριση με τα ηλεκτρόνια ή τις ακτίνες Χ, καθώς παρουσιάζει μια απότομη κορυφή Bragg και ως εκ τούτου μπορεί να στοχεύσει πιο αποτελεσματικά τον καρκινικό όγκο. Ταυτόχρονα, υπάρχουν πολλαπλά στοιχεία που υποδηλώνουν ότι όταν η ακτινοβολία χορηγείται σε εξαιρετικά υψηλούς ρυθμούς δόσης (FLASH), τείνει να έχει πρόσθετα προστατευτικά οφέλη για τους υγιούς ιστούς, σε σύγκριση με τους συμβατικούς ρυθμούς δόσης. Ωστόσο, οι ακριβείς επιδράσεις που έχει η ακτινοθεραπεία με πρωτόνια FLASH στους υγιούς ιστούς, είναι ακόμα ένα πεδίο υπό έρευνα.

Στην παρούσα διατριβή, διερευνώνται οι επιδράσεις της ακτινοθεραπείας πρωτονίων FLASH στα μιτοχόνδρια υγιών κυττάρων και συγκρίνονται με αυτές του συμβατικού ρυθμού δόσης. Για το σκοπό αυτό, αναλύονται εικόνες μικροσκοπίου TEM από ιστό λεπτού εντέρου τρωκτικών. Επιπλέον, ένας αλγόριθμος μηχανικής μάθησης εκπαιδεύεται στα δεδομένα των εικόνων, προκειμένου να αναγνωρίζει τα μιτοχόνδρια σε άγνωστες εικόνες κυττάρων. Στο πρώτο κεφάλαιο παρέχεται το απαραίτητο θεωρητικό υπόβαθρο στην ακτινοφυσική, την ακτινοθεραπεία, τη βιολογία και τη ραδιοβιολογία, την ηλεκτρονική μικροσκοπία και τη μηχανική μάθηση. Στο δεύτερο κεφάλαιο παρουσιάζονται τα υλικά και οι μέθοδοι που χρησιμοποιήθηκαν για τα πειράματα, καθώς και με λεπτομέρεια η προσέγγιση που ακολουθήθηκε για την ανάλυση των δεδομένων εικόνας και την εκπαίδευση του μοντέλου μηχανικής μάθησης. Στο τρίτο κεφάλαιο παρουσιάζονται και συζητούνται τα αποτελέσματα, ενώ το τελευταίο κεφάλαιο αποτελεί συμπέρασμα. Τέλος, επισυνάπτονται δύο παραρτήματα, για τους πίνακες των αποτελεσμάτων και για τον κώδικα προγραμματισμού.

Table of Contents

Chapter 1: Theoretical Background

1.1. Basic Radiation Physics

The term radiation refers to the propagation of energy in the form of waves or particles through a medium or space. Radiation can be either in the form of waves (rays) or it can be of particle nature. Some common types of radiation based on the propagating medium are electromagnetic radiation, which includes radio waves, microwaves, infrared, visible light, ultraviolet x-rays and gamma rays, acoustic radiation, particle radiation (such as alpha, beta, proton radiation, etc.) and gravitational waves.

Radiation is often also classified as ionizing and non-ionizing depending on the amount of energy it carries. The distinctive point is often given at 10 electron volts (eV). Radiation carrying more than 10 eV is able to ionize atoms and break most of the chemical bonds that play a role in biology, having a critical impact on living organisms [1].

1.1.1. Types of ionizing radiation

Ionization of matter from radiation can be either *direct* or *indirect*. Directly ionizing radiation deposits energy in the medium in a direct way through the Coulomb interactions between the radiative charged particles and the electrons of the atoms in the medium.

Indirectly ionizing radiation is usually photons or neutrons which ionize matter through a two-step process: Firstly, charged particles are released in the medium which in turn interact with the orbital electrons of the medium through Coulomb forces [1].

Ionizing radiation can be either electromagnetic or particulate. Particulate ionizing radiation includes alpha particles, beta particles, positrons, neutrons and protons, while electromagnetic ionizing radiation includes gamma rays and x-rays. For the purpose of this thesis, we will focus more on particulate radiation.

Alpha particles are practically nuclei of helium atoms. They consist of two neutrons and two protons and they are positively charged. Naturally, they are usually emitted by unstable atoms with a low neutron-to-proton ratio. *Beta particles* are high-energy electrons emitted from the nucleus of radionuclides. They have negative charge, in contrast to positrons which bear a positive one [2]. Lastly, *protons* are fundamental hadrons with a positive charge. All of the charged particles mentioned above are most often characterized as directly ionizing radiation because the ionization comes as a result of the Coulomb forces that are involved. Charged particles can be produced naturally by radioactive decays, artificially by accelerating devises or through indirect interaction of electromagnetic radiation with matter [1]. Beta particles are generally more penetrative than alpha particles because of their lower mass and lower charge, but they don’t reach further than the human skin [1]. Alpha particles result in more ionizations but they lose their energy rapidly and they have even smaller depth of penetration. Protons cause less damage than alpha particles and they are less penetrative than beta particles [1].

Gamma rays is high-energy electromagnetic radiation with frequencies greater than 30×10^{18} Herz and energy greater of 10^6 eV, while *x-rays* have lower energies ranging from 100 eV to 10^6 eV. Generally, gamma rays originate from internal nucleic processes while x-rays are emitted from outside of the nucleus. X-rays can be emitted either as a *characteristic x-ray* of an atom (as an electron of an outer shell fills the vacancy of an inner shell) or from accelerating electrons, in which case they are called *Bremsstrahlung radiation* [3]. In contrast, gamma rays are usually emitted from a process called *gamma decay*, in which an excited nucleus decays to a lower state producing energy. They can also be emitted as a product of electron-positron annihilation and other particle physics processes as well as from cosmic sources [4].

1.1.2. Radiation dose and relevant quantities

In the context of radiobiology, some important physical quantities are defined as follows.

- *Exposure* is the ability of radiation to produce ionization in air, under standard temperature and pressure. It is defined as

  $$X = \frac{\Delta Q}{\Delta m_{air}}$$

  Where ΔQ is the collected charge and Δm_{air} is the mass of the air and its S.I. unit is C/kg. This quantity only refers to the ionization of air and cannot be applied to biological tissue.

- *Absorbed dose* is critical for organisms. It refers to the amount of energy in joules absorbed per unit mass of target and it is defined as

  $$D = \frac{\Delta E}{\Delta m}$$

  Its unit in S.I. is 1 grey (1Gy = 1 J/kg).

- *Equivalent Dose* represents the health effects of ionizing radiation on tissues in a stochastic way. It is defined as the product of the radiative dose and a quality factor w_R, dependent on the type of radiation.

  $$H_T = D w_R$$

  Its unit in S.I. is 1 Sievert (1 Sv).

- *Effective dose* is the sum of the equivalent doses multiplied by a weighting factor for each different tissue. It is used to estimate the risk of radiation in each different tissue/organ and it is measured in sievert.

  $$E = \Sigma w_T \times H_T$$

1.1.3. Interaction of radiation with matter

Charged particles can interact with the atoms of the medium mainly through collisions. This can be either *elastic scattering* or *inelastic scattering*. The main difference between them is that, in elastic scattering, the total kinetic energy and momentum are conserved quantities, while in the inelastic case, energy can be transferred to another particle or in the form of a photon.

Electron interactions

Electrons can either interact with the nucleus or with the atomic electrons of the target material. In the case of inelastic scattering from the atomic electrons, some of the energy of the incident electron is transferred to an atomic electron, which remains bound to the atom (excitation, not ionization). The extra energy is then released in the form of an X-ray. If the incident and the atomic electrons collide elastically, the atomic electron usually experiences ionization, getting enough energy to escape the atom. This secondary electron might produce additional ionizations. When incident electrons interact inelastically with the atomic nucleus, it is slowed down and changing its direction, emitting Bremsstrahlung radiation in the form of X-rays. In elastic electron-nucleus collisions, the incident electron simply bounces off, without losing energy, due to its far smaller mass [5].

Protons and other heavy charged particles

When heavy charged particles travel through a medium, thousands of orbiting electrons are attracted to them due to their charge. This causes both excitations and ionizations to the atoms in the medium. As they interact with the electrons, they slow down, attracting even more electrons, until they completely lose their kinetic energy. After reaching a threshold kinetic energy of 0.01 MeV, heavy charged particles are able to interact with the nucleus, resulting in various nuclear reactions. They can also experience Bremsstrahlung but it has minimal effect because of their large mass [5].

Neutrons

Due to their zero charge, neutrons mainly interact with the atomic nucleus. When a neutron has high kinetic energy, it might undergo elastic collision with a proton of the nucleus, releasing it from the atom. Neutrons are more likely to interact elastically with light nuclei, like hydrogen and less likely with heavy ones, such as lead.

When neutrons are sufficiently slow (thermal neutrons, 0.025 eV), they can participate in nuclear reactions, like radiative capture, transmutation or fission [5].

On the other hand, electromagnetic radiation can generally interact with matter in three ways: Through the photoelectric effect, the Compton scattering and the pair production. We will briefly look at each of the above.

Photoelectric effect

This is an atomic phenomenon in which a photon is absorbed by an orbital electron of an atom of the medium resulting in its ionization. In order for the electron to be ejected from the atom, it is necessary for the photon to have energy greater than the binding energy E_b of the electron. The following formula gives the kinetic energy K_e of the ejected electron.

$$K_e = hv - E_b$$

Where hv is the energy of the incoming photon. In most cases, the vacancy left from the ejected electron is filled with an electron of an outer shell, which upon descending, emits energy in the form of a characteristic x-ray as mentioned above [1]. These x-rays are called characteristic because each element has unique energy levels and as a result, emitted x-rays can be used for their identification. Sometimes, especially when the target is biological material, the emitted x-ray can be reabsorbed by another electron of the atom resulting in a secondary ionization. This is known as the *Auger effect* [1].

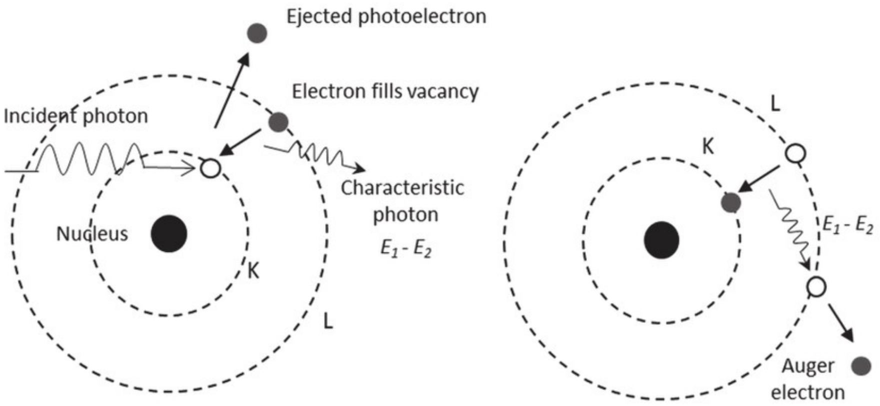

Figure 1.1. Schematic representation of the photoelectric effect, characteristic x-ray production and Auger effect. [4]

Compton scattering

In this interaction, the incident photon is scattered by a free electron or at least by an electron whose energy is considerably small compared to that of the photon. The photon transfers part of its energy to the electron and it is re-emitted in a different angle θ. The electron acquires kinetic energy and velocity at a different angle φ. The amount of energy transfer depends both on the initial energy of the photon and on the angle θ.

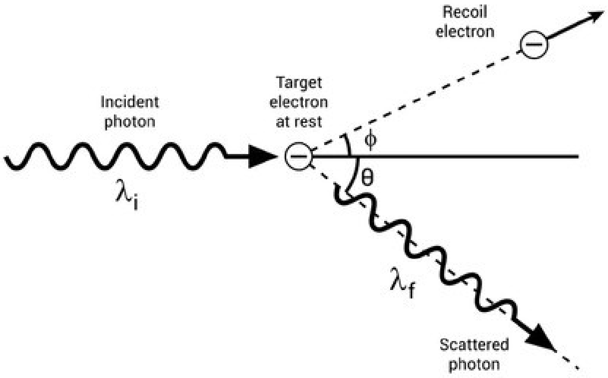

Figure 1.2. The Compton effect [3]

Pair production

It is the process in which a high-energy photon, travelling at the vicinity of the nucleus, produces a pair of an electron and a positron. For the production to occur, it is necessary that the energy of the photon is equal to at least two electron masses, which is approximately 1.022 MeV. The produced positron, after losing its energy, annihilates with an electron, creating a pair of gamma rays.

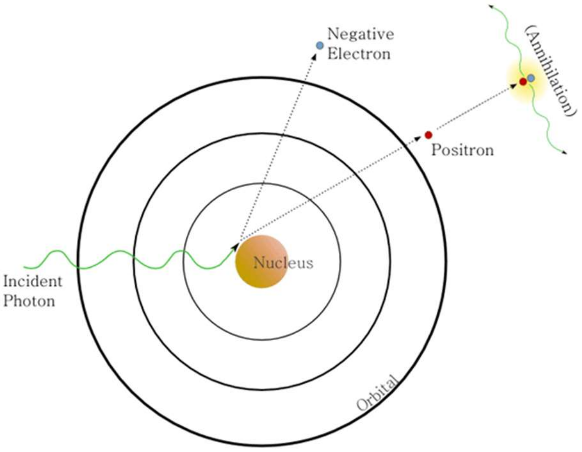

Figure 1.3. Schematic representation of pair production [4]

1.2. Physical and Biological Characteristics of Particle Therapy

Radiation therapy (radiotherapy) has extensively been used in cancer treatment for many decades. Ionization radiation damages the genetic material of cancerous and normal cells, resulting in prolonged abnormal cell function which finally may lead to cell death. Beams of electromagnetic radiation and especially x-rays have been tested for years and are considered the ‘conventional’ treatment method in clinical practice [7]. Charged particle therapy on the other hand, is a relatively new development, emerged in the late twentieth century. It offers significant advantages compared to the conventional method, achieving more effective tumor control while sparring the surrounding normal tissue. Proton therapy is the most widely used type of charged particle radiotherapy, with carbon ion therapy being developed in recent years [6]. In the following section we will focus our interest on proton beam radiotherapy.

1.2.1. Proton Beam Radiotherapy

Physical characteristics of proton therapy

The main physical difference between electromagnetic and particle radiotherapy is the distribution of dose as a function of depth. While photons deliver the maximum dose upon entering the tissues, protons and other charged particles deposit most of the dose at the end of their trajectory, when they decelerate [7]. This is known as the “Bragg Peak” and is shown in figure 1.4.

The existence of the Bragg peak is of utmost importance for clinical practice as the steep and localized nature of dose deposition allows for a targeted delivery of radiation over the tumor. In contrast, conventional x-ray beams, bearing no mass or charge, penetrate deeper inside the tissue depositing energy at an exponential rate along the whole length of their path. Consequently, proton beams can deliver the same amount of dose in the tumor with much less irradiation of the surrounding normal tissues compared to the conventional method, resulting in important health benefits [7].

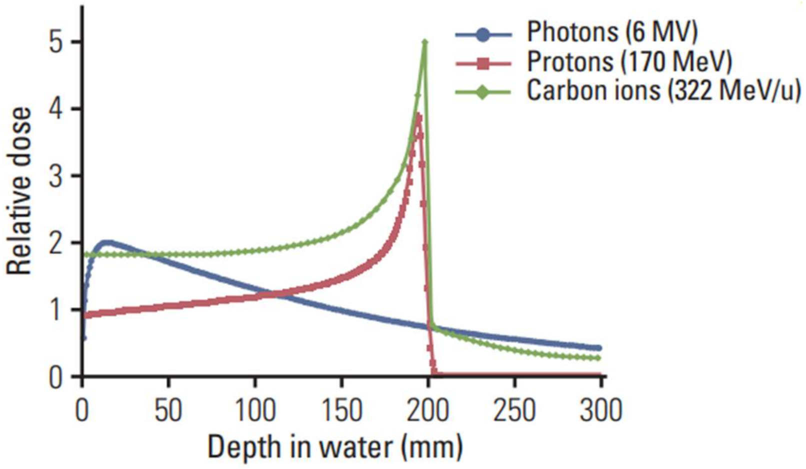

Figure 1.4. The Bragg peak of proton beam and carbon ion beam compared with the dose distribution of electromagnetic radiation. [6]

The shape of the Bragg peak varies with the type of the charged particle and it is dependent on the energy spreading of the beam, its range straggling and its lateral sharpness, all of which being inversely proportional to the mass of the particle [6]. Additionally, depending on the size and the depth of the tumor, the Bragg peak can be adjusted and broadened. This is termed as "spread out Bragg peak" (SOBP) and it is the sum of several individual Bragg peaks at staggered depths. A typical SOBP is shown in figure 1.5.

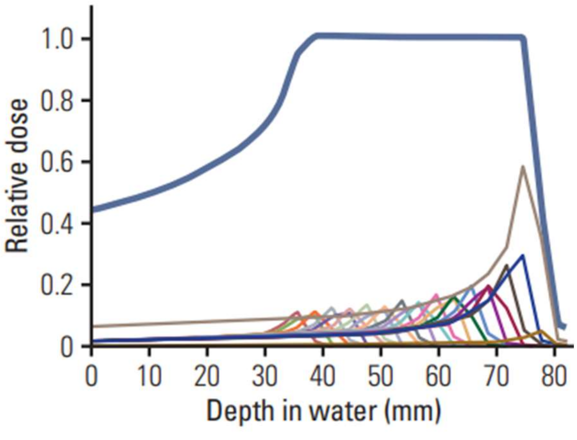

Figure 1.5. SOBP of carbon ion beam [6]

Biological characteristics of proton therapy

In the context of radiobiology two crucial concepts are used in order to explain the effects of radiation in living matter. These are the *linear energy transfer* (LET) and the *relative biological effectiveness* (RBE).

Linear energy transfer refers to the energy transferred in the medium per unit length of the track. Travelling charged particles ionize atoms along their track. These ionizations are localized and differ for each type of particle. So, for example, proton beams have a higher LET compared to photons but a lower LET compared to carbon ions, which are considered high-LET beams. Proton beams cause a uniform and sparse ionization across their track, in contrast to the equivalent of carbon ion beams, which is more dense and thus more biologically active [6].

From the aforementioned, it has been clear that in case of different types of radiation, even when the absorbed dose is the same, the produced biological effects differ. For example, 1 Gy of carbon ion beams produces a greater biological effect than 1 Gy of X-rays [6]. The concept of *relative biological effectiveness* compares the biological effect of different types of radiation with that of x-rays. X-rays were selected as the point of reference because of their wide use. RBE is defined as the ratio D_{250}/D_r where D_{250} and D_r are the doses of 250 kV x-rays and test radiation required for equal biological effect [6]. The quantity labeled as 'biological effect' is most often the death of half of the cells in a test group.

LET and RBE are closely related, with the latter being a function of the first. More specifically, RBE initially increases approximately linearly with increasing LET, before it reaches a turning point and starts to decrease (Fig. 1.6) The decrease beyond the turning point is due to energy wasting as the ionizing events are closer than the diameter of the DNA double helix [6].

In the case of proton beams, the generally used value of RBE is 1.1. irrespective of fractionation, tissue type, or radiation quality [6]. This value is constant alongside the track of the proton beam and thus it is the same for normal tissues and the tumor. However, as shown in figure 1.7, the actual value of RBE is changing with LET, which in turn gets its maximum value close to the end of the trajectory of the protons. As a result, the maximum value of RBE is observed at the distal part of the range of the proton beam [6].

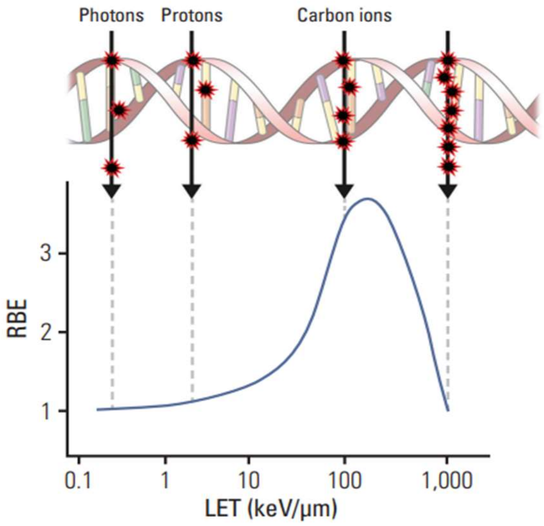

Figure 1.6. RBE as a function of LET. RBE values of the most important radiation types are noted. [6]

Beam delivery systems

The proton beam used in radiotherapy is mainly produced by accelerator systems. In conventional x-ray therapy, linear accelerators are used to accelerate electrons which form a beam. In proton therapy however, the limited size of a linear accelerator cannot produce a sufficiently strong electric field in order to accelerate the heavier protons. Thus, circular accelerators are being used, such as cyclotron, synchrotron and synchrocyclotron [6]. In therapeutic applications, protons are accelerated in energies ranging from 70 to 250 MeV [7].

Particle beams can be delivered with two different methods: *Passive system beam scattering* and *active system beam scanning*. The first method makes use of a modulator, a collimator, and a range compensator to create an SOBP at the desired depth and of dimensions that match the volume size of the target. The lateral and longitudinal spreading of the beam is achieved by the modulator, while the collimator and the compensator are further shaping the beam to conform it with the target [7]. The second method is more precise and clinically more effective [7], as the peak position can be moved within the target, like a scanner, by controlling the beam energy in the accelerator or by changing the beam's penetration using absorbers [6]. For each beam, the treatment is delivered in "layers," defined by their energy. Cumulatively, contributions from multiple beams produce the desired pattern of dose [7]. The two beam delivery systems are shown in figure 1.7.

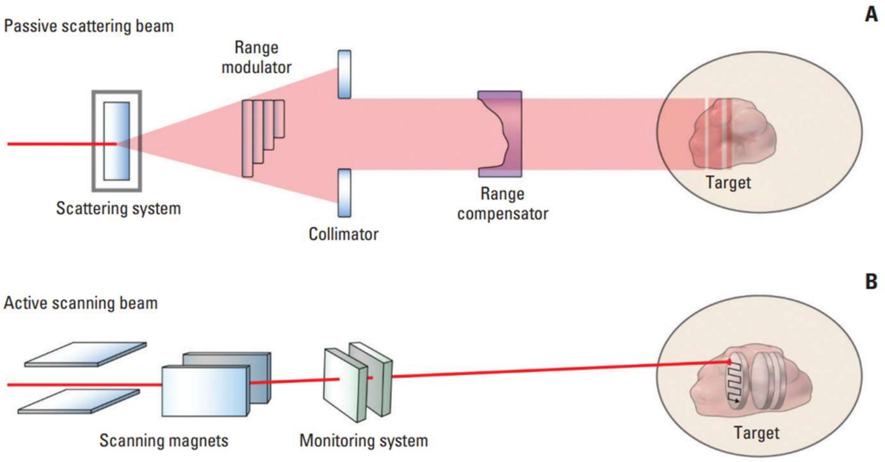

Figure 1.7. Scheme of passive scattering beam (A) and active scanning beam (B). [6]

1.2.2. FLASH Radiotherapy

The term FLASH radiotherapy refers to the delivery of ultra-high dose rate radiation, usually ≥ 40 Gy/s, significantly higher than the rate used in conventional methods (~5 Gy/min) [8]. It is a very recent development in cancer therapy as research interest started in 2014 and since then it has given really promising results. Its main advantage over conventional dose rate therapy is that it possesses a normal tissue sparing capability while maintaining tumor cytotoxicity [9]. This ability of FLASH radiotherapy is known among the scientific community as the “FLASH effect”.

The FLASH effect was first reported in 1964 but it wasn’t particularly investigated till the recent years [9]. Experiments in mice have shown that irradiation with FLASH dose rate results in significantly less damage to normal tissues of the lungs, the brain and the skin compared to the conventional rates of the same total dose [8,10,11,12]. It is worth noting that in the long-term, FLASH irradiated cells exhibited functioning more like the non-irradiated cells than like the ones which were irradiated conventionally [9].

Apart from sparing normal tissues, FLASH effect has also been reported to have high control of the tumor. This means that despite the limited effect of FLASH radiotherapy over normal tissues, its anti-tumor properties are comparable to those of conventional rate therapy. In studies involving breast, head and neck cancer treatment in mice, FLASH proved to be as effective as conventional radiotherapy, without some post-radiation side-effects such as fibrosis and inflammation [9, 10, 11]. FLASH radiotherapy has also been applied successfully to a human patient with CD30+ T-cell cutaneous lymphoma and it also has been compared with conventional dose-rate radiotherapy. The results showed no significant differences between the two, with both of them having the same acute and late effects, such as skin irritation [12]. However, further research should take place before FLASH radiotherapy is used in clinical practice; mainly in case of tumors other than superficial skin ones.

The mechanism behind the FLASH effect is not yet fully understood but the most prevailing explanation is the oxygen depletion hypothesis. Upon irradiation, apart from the direct damage, the DNA molecule undergoes indirect damage through water radiolysis and subsequent generation of reactive oxygen species (ROS) which attack the DNA. In the case of low-LET radiation, 60-70% of DNA damage is caused by ROS [9]. Therefore, it is obvious that the shortage of oxygen molecules results in less DNA damage, something which explains why hypoxic environments (like tumors) are radioresistant. In the case of FLASH, the oxygen depletion hypothesis suggests that, due to the short exposure time frame, local oxygen is depleted faster than reoxygenation can occur, leading to a state of hypoxia which increases radioresistance and protects the normal tissues [9]. The reason why this phenomenon does not also increase the radioresistance of cancer cells is still under investigation, however it is often attributed to the different morphology of ROS and free radicals that are generated in tumor environments [9].

Currently, most of FLASH radiotherapy experiments are performed using electron beams on linear accelerators. However, this type of radiation is limited in treating effectively mainly superficial cancers due to its low tissue penetration [9]. The advantages of proton radiotherapy, analyzed in the previous section, make it clear that proton FLASH radiotherapy should be researched further. Current *in vitro* studies are ambiguous on whether FLASH effect is still present in FLASH proton therapy [9]. Recently reviewed data revealed that only one in ten studies demonstrated the FLASH effect in protons [13]. However, it is worth noting that all of these experiments were performed at aerobic conditions, something which might be the reason for not observing the FLASH effect. As a result, further in vitro studies need to take place, in varied oxygen levels. On the other hand, *in vivo* studies are more promising, with experiments in gastrointestinal and thoracic tissue of mice demonstrating the expected normal tissue sparring and tumor control of the FLASH effect [14,15]. Another study examining the effect of proton beam FLASH on brain tumor of mice showed no significant differences between FLASH (100 Gy/s) and conventional dose rate (1Gy/s) therapies for the same single fraction of radiation (10 Gy) [16]. Nevertheless, additional insight on FLASH proton beam therapy should be acquired, and this is something that the current study aims to do.

1.3. Cell Biology and Histology

Histology is the science interested in the microscopic structure of biological material and the ways in which individual components are structurally and functionally related [17]. Its scope stands at the borders of biochemistry, molecular biology, physiology and pathology, giving a unique perspective to the biological and medical fields. Nowadays, techniques such as electron microscopy, cell cloning and molecular genetics allow for precise and in-depth experiments, making histology a rapidly evolving field [17].

Probably the most fundamental concept of histology is cell theory. Cells are the basic building blocks of biological matter. They are separated from their environment by their cell membrane and they are specialized so as to perform certain functions. According to their specialization, the basic types of cells are: epithelial cells, supporting cells, contractile cells, nerve cells, germ cells, blood cells, immune cells and hormone-secreting cells. This categorization is not absolute and one cell may belong to more than one type [17].

Cells arranged together in an organized way in order to perform higher level functions form a *tissue* (Greek: “ιστός”) (see figure 1.8). Tissues might consist of cells of the same type, in which case the tissue is called simple, or of cells of more than one type, in which case it is called compound. For example, nervous tissue contains nerve cells, support cells, epithelial cells and immune cells [17]. Ascending one level higher, tissues grouped together in an anatomically distinct way, form *organs* (e.g. the heart, kidney or brain). Organs which have similar or related functional roles are often referred to as systems. Thus, for example, there is the musculoskeletal system, nervous system, alimentary system, etc. The relationship between cells, tissues, organs and systems is presented in figure 1.9.

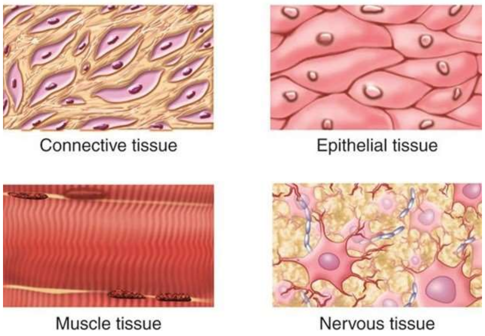

Figure 1.8. Different types of tissues.[18]

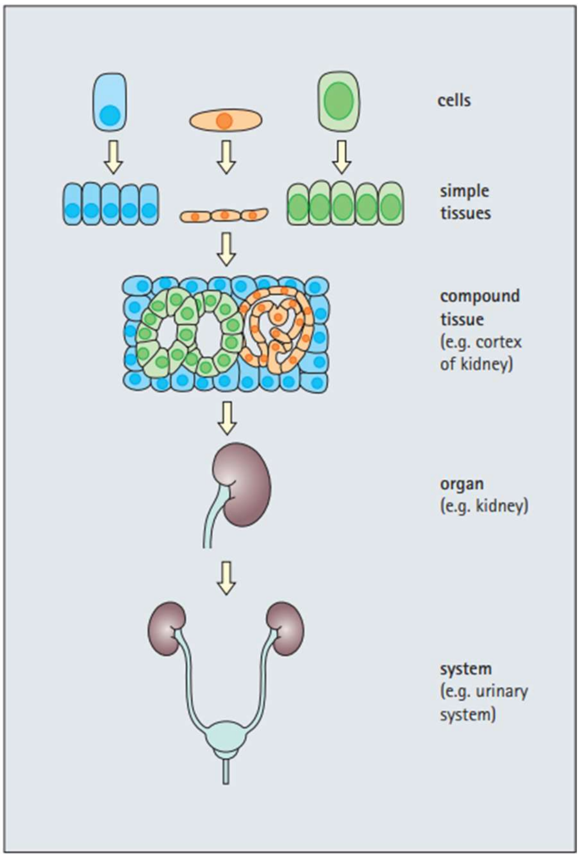

Figure 1.9. The hierarchical structure of human anatomy [17].

1.3.1. Cell Structure

All types of cells share some common defining characteristics. Cells are composed of specific subcellular compartments, which can be organelles, specific structures that take on sets of tasks within the cell, or they can be local regions of the cell defined by the concentration of molecules or distinct physical characteristics and proportions. Subcellular structures include the nucleus, the cytoskeleton, the endoplasmic reticulum, the ribosomes, the Golgi apparatus, and the mitochondria. Each cell is surrounded by its *cell membrane*, which separates it from the environment and contains the various *organelles*. Organelles are specialized functional compartments of the cell which have their own membranes and are surrounded by a proteinaceous fluid termed *cytosol.* The shape and fluidity of the cell is determined by the *cytoskeleton*, an arrangement of internal filamentous proteins such as actin and microtubules [17]. Below, we are going to present a brief overview of the different subcellular structures and their function.

Cell Membrane

It is composed of a lipid bilayer containing specialized proteins for the transportation of material in and out of the cell and its communication with the environment. The main lipid structure is formed spontaneously on water, as lipid molecules have one hydrophilic end and one hydrophobic end, tending to form bilayers. Because of this composition, cell membrane is fluid, allowing diffusion of membrane proteins and facilitating the mobility of the cell, as well as eliminating breaks and tears. It is also highly selective to its permeability, allowing water, oxygen and small molecules to enter the cytosol, while blocking charged ions such as N^+ and K^+ [17]. Membrane proteins have various functions, such as transporting molecules in and out of the cell, attaching cytoskeletal filaments to the membrane, as well as cells to the extracellular matrix, or receiving chemical signals (e.g. hormone receptors) [17].

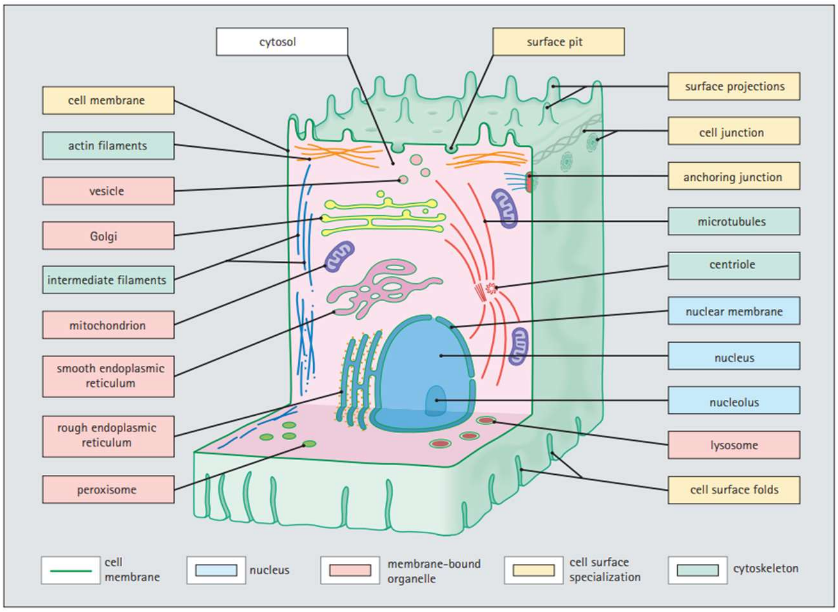

Figure 1.10 Cell structure [17]

Cytosol and Cytoskeleton

Cytosol is the dense fluid matrix in which all organelles are found. Apart from organelles, it contains the cytoskeleton and numerous free *ribosomes*, particles which are involved in protein synthesis. Inside the cytosol there exist also various nutritious enzymes and products of metabolism [17].

Cytoskeleton is formed by protein filaments; it defines the shape and maintains the stability of the cell. The filamentous proteins become attached to cell membranes and create a dynamic three-dimensional scaffolding of the cell that performs multiple tasks, such as shaping the cellular architecture, enabling cell mobility, transporting material inside the cytosol and compartmentalizing the cell [17].

Nucleus

It is the larger single-membraned organelle in the cell and contains the genetic material (DNA). It is usually spherical or ovoid in shape with a diameter of around 5-10 μm. Nucleus contains a smaller spherical compartment, the nucleolus, which synthesizes ribosomal subunits. DNA inside the nucleus is tightly packed around proteins called 'histones', forming *nucleosomes*. These nucleosomes, in turn, wound into filaments, creating a structure called *chromatin*. Chromatin can be further condensed into distinct chromosomes. The distribution of chromatin is not the same everywhere, being less dense in the regions where an unfolding exists, for example in case of DNA transcription. As a result, in microscopy photos of the nucleus, the less dense regions appear brighter ('euchromatin') while the denser ones bear a darker tone ('heterochromatin') [17].

Mitochondria

Mitochondria are the main energy production sites of the cells. They have cylindrical shape measuring 0.5-2 μm in length. Mitochondria are believed to have evolved from procaryotic organisms, symbiotics to the human cells, as they have their own DNA and protein synthesis system [17].

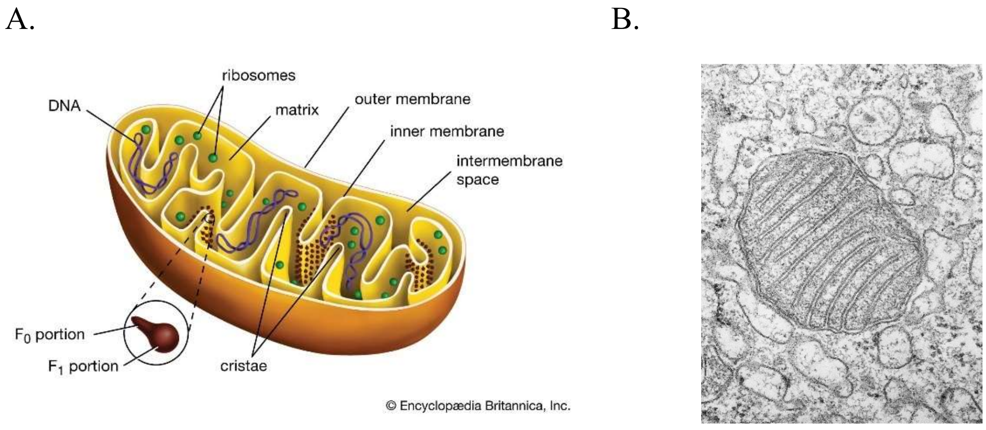

© Encyclopædia Britannica, Inc.

Figure 1.11. Schematical illustration (A) and TEM micrograph (B) of a mitochondrion. [17,19]

Each mitochondrion bears an outer and an inner membrane. The inner membrane is folded into pleats (cristae), increasing its surface area. It is highly impermeable to small ions and it is the place where ATP, the ‘energy coin’ of the cell, is generated by the mitochondrion through oxidative phosphorylation. It also contains the mitochondrial DNA, ions and enzymes. The outer membrane is responsible for the transportation of molecules. One of its most important properties is that it can release large mitochondrial proteins into the cytosol, through transmembrane pores. The release of these proteins, triggered by a variety of stimuli, begin a series of actions that lead to cell death (apoptosis) [17]. Given that the mitochondria act as transducers of certain stimuli that lead to cell death, they are a good measure of the health condition of the entire cell.

Endoplasmic Reticulum (ER) and Golgi

ER and Golgi are two different regions of an intercommunicating membrane-bound system that takes part in the biosynthesis and transport of proteins and lipids inside the cell. Their shape resembles a multiple-times-folded flattened membrane. ER can be of two forms, *smooth* and *rough* endoplasmic reticulum. Smooth ER is responsible for lipid synthesis and processing of proteins, while in rough ER peptides are translated with the aid of ribosomes attached to its surface, hence the name ‘rough’. Lastly, Golgi is responsible for further processing the proteins after smooth ER, as well as for the modification and sorting of macromolecules [17].

Autophagosomes

Autophagosomes are organelles in the macroautophagic pathway. They are membraned vesicles that form around cellular components, such as damaged organelles or proteins, to sequester them for degradation. They are involved in a process called autophagy, in which cells recycle their own contents to maintain homeostasis [17].

1.3.2. The Digestive Tract

Digestive tract is a part of the human alimentary system responsible for the digestion of food material and the absorption of the end products of it. It comprises the stomach, the small intestine and the large intestine. The digestive tract can be seen as a muscular tube, lined on its interior by specialized epithelial cells, which have both absorptive and secretory function. The patterns of the epithelial cells on the three main organs of the digestive tract differ, as shown in figure 1.11. In its exterior, the tract is covered by an outer layer of flat mesothelium where it runs through the peritoneal cavity. Various secretory organs, such as the pancreas and the liver, lie partly or completely outside of it. These organs produce secretions which are vital for the proper digestive function [17].

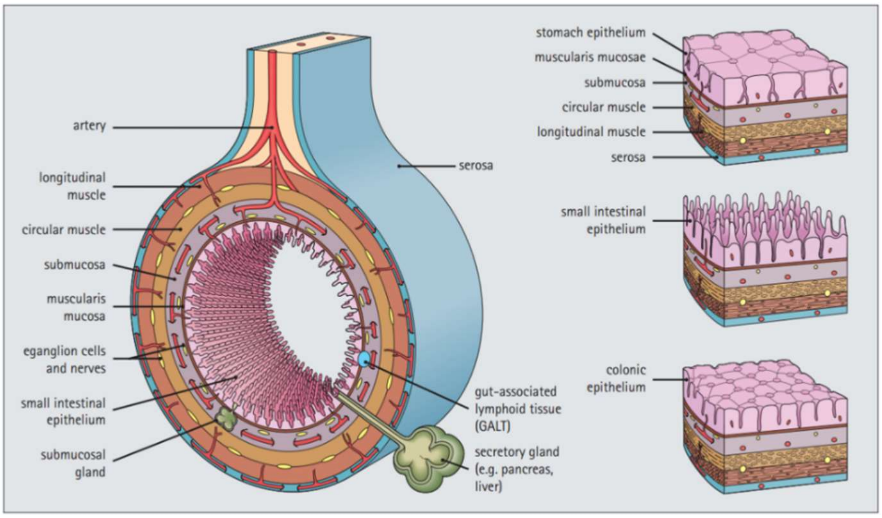

Figure 1.12. Illustration of the basic structure of the digestive tract [17]

The epithelium of the tract is supported by a variable layer which is called lamina propria and it is composed of supporting cells, nerve cells, blood vessels and cells of the immune system. In the deep aspect of lamina propria lies a thin muscle layer, muscularis mucosae. On the outer side of muscularis mucosae, lies the submucosal layer which also contains vessels and nerves that supply and drain their equivalent in lamina propria. The mucosa and, partially, the submucosa contain lymphoid tissue which provides the immunological defense against antigens ingested in the digestive tract [17].

Exterior to the submucosal layer, two layers of smooth muscle exist, traditionally called circular and longitudinal layers. Their purpose is to facilitate the movement of the luminal contents along the tract through peristalsis. In certain areas, localized thickening of the circular muscle is observed, called *sphincter*. Sphincters act as valves, preventing the contents of the lumen to pass or to change direction of motion.

Lastly, the outer shell of the tract is called adventitia and it is composed of loosely arranged fibroblasts and collagen. When adventitia is covered by mesothelium (as in the case of the small intestine), it is called *serosa* [17] (see also fig 1.12).

In order to maximize the efficiency of absorption and secretion processes, the digestive passage forms folds and glands in its interior so as to increase its surface area. In this way, more epithelial cells come in contact with the lumen. Increase in surface area can be achieved by intrusions or inversions of the lining epithelium or by formation of complex glands on the tract wall. The gut has a great collection of nerves and ganglion cells that in some areas (mainly the surrounding muscles and the submucosal layer) take the form of an interconnected network-like plexus. The autonomic impulses in these nerves mediate visceral reflexes and sensations such as hunger and rectal fullness [17]. The present thesis focuses on the morphometric analysis of intestinal tissues and most specifically, the small intestine.

1.3.3. Small Intestine

The food material, after being partially digested in the stomach, goes through the pyloric sphincter and continues to the small intestine. There, enzymes are secreted to complete the digestion, while the basic products of digestion (such as sugars, fats and amino acids) are absorbed. The small intestine starts at the *pylorus* and ends at the *ileocaecal valve*, which connects it with the large intestine. In life, the small intestine measures about 3 m in length, while in autopsy, where muscles are relaxed, it can reach up to 6 m. It is divided into three regions, *duodenum*, *jejunum* and *ileum*, although their limits are not strictly defined. The three regions of the small intestine perform different functions. Duodenum mainly receives secretions from glands (e.g. liver and exocrine component of the pancreas), jejunum is the main absorptive site and ileum is characterized by a greatly developed lymphoid tissue [17].

The mucosa and submucosa of the small intestine are shaped in numerous folds or *plicae* that are arranged circularly around the lumen. The surface of the plicae is further arranged into *villi*, smaller protrusions into the intestine (see fig, 1.13). At the base of the villi, there are tubular glands called ‘crypts’ that extend down to the muscularis mucosae. The epithelium of the small intestine has three functional regions, the villi, the crypts and the neck zone, which is the area where the villi and the crypts merge. Many types of cells are involved in the formation of the epithelium, including enterocytes, mucous cells, endocrine cells, Paneth cells, etc. and they are distributed inhomogeneously [17].

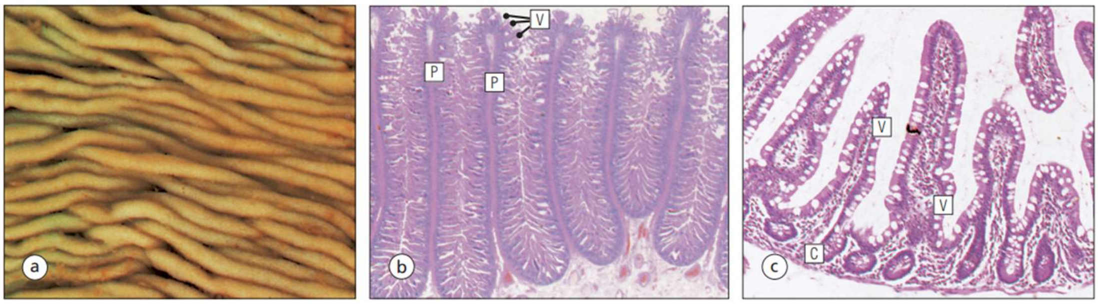

Figure 1.13. The architecture of the small intestine. A) Macroscopic view of the plicae. B) Micrograph of the plicae (P) in which the villi can be seen. C) Closer view of the villi (V) and the crypts (C).[17]

The main cells in the villi, which are also the cells that we will focus our interest on in the present thesis, are the *enterocytes* (see Figure 1.14). They are tall columnar cells with oval-shaped nucleus in the lower third of their length. Enterocytes are absorptive in nature. Their surface is highly specialized, with each cell bearing 2000-3000 densely packed microvilli. Microvilli are coated with a glycoprotein, the *glycocalyx*, which contains a number of proteins important in digestion and transport. Beneath their surface, enterocytes contain lysosomes and smooth endoplasmic reticulum, while, as we approach the nucleus, ribosomes, mitochondria, Golgi and rough ER prevail. The lateral walls of enterocytes are the sites of Na^+ and K^+ ATPase activity and they are separated from the microvillus surface by desmosomes and tight junctions [17].

Apart from enterocytes, in the epithelium lie several other types of cells. *Mucous cells* are mostly found in the upper part of the crypts or can be scattered among enterocytes of the villi. They are most frequent in the ileum and jejunum parts while their number decreases in the duodenum. *Paneth cells* are found at the base of the crypts. Their main function is to protect against infections by secreting a substance called 'defensine'. *Endocrine cells* are located on the lower part of the crypts as well as the villi and they produce a number of hormones and peptides. Lastly, a number of unspecialized stem and intermediate cells can be found in the lower third of the crypts, waiting to develop in order to replace the mucous cells and enterocytes of the villi, as these cells have a short lifespan of about five days. In many cases of illnesses of the small intestine, stem cells are particularly numerous [17].

Figure 1.14. TEM image of small intestinal tissue. The nuclei of the various enterocytes can be seen.

1.4. Radiation Damage on cells and tissues

1.4.1. Effects of Ionizing Radiation on cells and tissues

When biological matter is irradiated, it undergoes physiological changes as a result of ionization. The most severe consequence of IR is cell death. Cell death can be classified in two types, based on the time that the cell disintegrates after exposure: *Interphase death*, where disintegration happens before cell enters into the first mitosis after irradiation, and *reproductive/mitotic death*, where the cell dies several divisions after exposure [20]. Both types of cell death can be caused by either necrosis or apoptosis. Necrosis refers to the irreversible destruction of cell membranes and metabolism as a result of extreme damage from IR. Apoptosis, on the other hand, is an intrinsic self-destructing mechanism of the cell, which is triggered by specific proteases and endonucleases. The cause of cell death depends on the dose of irradiation, with lower doses of radiation usually inducing apoptosis, while necrosis is caused mainly by higher doses [20, 21]. In addition, necrosis and apoptosis can be distinguished by their morphological features. Apoptosis is characterized by shrinkage and fragmentation of the nucleus, disintegration of the Golgi complex and dilation of the endoplasmic reticulum. Mitochondria also experience alterations during apoptosis, like swelling and disappearance of cristae [20,22]. Necrosis, on the other hand, is characterized by vacuolization of the Golgi complex, lysosomal rupture, mitochondrial swelling, disorganization of cytoskeleton and breaking of the plasma membrane [20].

The effects of IR on plasma membrane can be varied. Radiation-induced membrane perturbations are primarily characterized by changes in the organization and composition of the cell glycocalyx, leading to altered amounts and distributions of negatively charged membrane components, such as sialic acid and calcium-binding sites. Ionizing radiation typically causes a temporary reduction in surface negative charges, which however recover within an hour. Exposure to radiation can also modify calcium localization within cell membranes, affecting intracellular communication and the structure of intercellular contacts like gap junctions. These alterations in cellular morphology, surface micromorphology, and intercellular connections contribute to disrupted cell communication, increased genetic instability, and potential cellular transformations, such as tumorigenesis [20]. Finally, a common effect of radiation in epithelial cells is the loosening of contact with each other and the growing of lateral and basal projections. *Tight junctions* (TJ) of the epithelial and endothelial cells undergo changes or break completely. This may lead to aberrant cell proliferation, adhesion, function and migration [23].

Cellular organelles also undergo morphological changes in case of exposure to ionizing radiation. As far as the nucleus is concerned, studies on irradiated cells show changes in nuclear shape (such as swelling and irregularity of the border [23]), chromatin condensation along with formation of nuclear bodies (ring-like chromatin aggregates), as well as alterations on the nuclear envelope [20]. Post-IR effects on mitochondria include swelling, elongation, branching and an increase in size resulting in the creation of giant forms. Some studies indicate that the total number of mitochondria also changed dynamically after irradiation, while vacuolization and disruption of outer and inner membranes and cristae of mitochondria are also frequently observed after exposure [20, 24]. IR may also cause enlargement of the Golgi complex, degranulation and fragmentation of the endoplasmic reticulum and redistribution of the cytoskeletal filaments [23, 20]. In addition, an increase in the number and volume of lysosome-like vacuoles in the enterocytes has been observed [25]. Last but not least, irradiation may lead to abnormal levels and fluctuations many brush border enzymes, such as lactase, sucrase, maltase, etc. Ionizing radiation could be activating or altering various intracellular signaling pathways, leading to tissue pathophysiological changes and increased cell death [23].

Specifically for the small intestine, the effects of ionizing radiation might include partial or complete loss of integrity of the intestinal epithelium (which is the earliest responding tissue in the intestine) as well as damage on the haemopoietic and immune cells. Apart from depletion of the epithelium, connective tissue and vessels are affected, with fibrosis being a common pathological alteration. Fibrosis is characterized by accumulation of a dense extracellular matrix in the submucosa, muscular propria and subserosa regions [23].

Under normal circumstances, the crypts which lie under the villi of the small intestine, contain a significant number of stem cells. Their purpose, as discussed in 1.3.3, is to replicate and replace the specialized cells of the villi. In case of exposure to ionizing radiation, due to the death of enterocytes and muscular cells, rapid repopulation takes place. In addition, radiation prevents stem cells from reproducing by causing mitotic inhibition. As a result, a significant loss of stem cells is observed after irradiation [23]. This has a profound impact on the shape of the crypts and the villi. More specifically, a decrease in the circumference of the crypts and the height of the villi is observed, along with swelling and increase of bacteria in the irradiated area. In addition, changes in the length, diameter and frequency of the microvilli of enterocytes is observed [23]. Beside the epithelial cells, other types of cells undergo apoptosis and changes in their morphology as well, such as fibroblasts and lymphocytes [23].

It is important to note that not all cells react to radiation in the same way as in the small intestine. In general, lymphatic tissue and red bone marrow cells are among the most radiosensitive, leading to hypoplasia and hemolysis following exposure greater than 2 Gy. At even higher doses, brain function could be affected too and cerebral cell death may occur. In addition, studies on animal fetus indicate that radiation can affect the implantation of the embryo in the wall of the uterus, although further data should be gathered from human embryos [26].

1.4.2. Effects of Ionizing Radiation on Biological Molecules

Ionizing radiation affects biological macromolecules either directly or indirectly, through radiolysis of water and the subsequent creation of high-energy species (i.e., high-energy molecules). Upon irradiation of cellular water, reactive oxygen species (ROS) (e.g. hydrogen peroxide (H_2O_2), hydroxyl radical ($^{\cdot}OH$)) and reactive nitrogen species (RNS) (e.g. nitric oxide ($^{\cdot}NO$), peroxynitrite ($ONOO^-$)) are generated rapidly. These species are very reactive with biomolecules, such as the DNA, therefore they are extremely harmful to the cell. The effects from these chemical reactions occur in a time window which ranges from 0.01 ps to several minutes or hours. Direct radiation damage, on the other hand, is even more rapid, on the range of 10^{-14}-10^{-12} s and it refers to the breaking of S-H, O-H, N-H and C-H bonds [27]. Reactive species may also be formed via the activation of endogenous ROS-producing systems. Directly created ROS and RNS are more reactive and affect a wide range of biomolecules, while those produced by endogenous processes tend to be more selective. Early, rapid biochemical processes cumulate and they may affect the cell later on, manifesting their effects after minutes or hours [28].

Effects of IR on Nucleic Acids

The effects of ionizing radiation on nucleic acids have been known for many decades and have been extensively researched. DNA damaging inflicted by radiation include the deleterious alteration of bases and sugars, single- and double-strand breaks, cross link formation and DNA-clustering. Among the products of radiolysis, $^{\cdot}OH$ is the most destructive to nucleic acids, as well as the most abundant. $^{\cdot}OH$ radicals, along with nucleic acid-binding enzymes, cause DNA strand breakages, as they interact with H molecules, resulting in damage to deoxyriboses. Nucleobases are also affected by $^{\cdot}OH$, resulting in oxidative modification and abasic sites, though not on immediate strand breaks. Recent studies show that hydrated electrons also play a crucial role in the cumulative effects of ionizing radiation on DNA [28, 29].

After radiation-induced damage, cell responds immediately to repair itself. A complicated network of sensor, transducer and effector proteins is activated, initiating a cytoprotective response. Sensor and transducer proteins are able to locate DNA damage sites and initiate a series of biochemical reactions [29].

Effects of IR on Lipids

Ionizing radiation can induce damage on the lipid layer of the cell membrane. Though radiation is capable of directly damaging lipids, there is indication that indirect damage induced by water radiolysis products is a more prominent threat. The main consequence of IR is the cause of lipid peroxidation, especially that of unsaturated fatty acids, leading to increased membrane permeability, disruption of ion gradient and altered activity of membrane proteins. In addition, studies on cell membrane indicate the induction of apoptosis at 5-10 Gy [28, 30].

Lipid peroxidation leads to the formation of lipid hydroperoxides (LOOH), the amount of which determine the biological response of the cell [30]. Moderate levels of LOOH activate the oxidative stress response which might lead to apoptosis. Higher levels of LOOH result in global damage of the cell membrane and the organelles, triggering lysis of the membrane and necrosis. Cells are known to possess natural mechanisms to reduce LOOH levels, however, IR can inactivate the detoxifying enzymes involved, leading to an intense disruption of cellular redox metabolism [28].

Another effect of IR on lipids is the alteration of the sphingolipid metabolism. Exposure to IR might lead to relocalization of some enzymes involved in the production of sphingolipid ceramides, resulting in increased intracellular levels of them. The large accumulation of ceramides within membrane lipid rafts alters the membrane properties, forming large, ceramide-enriched membrane platforms. These platforms contain enzymes that are relocalized on irradiation, changing the molecular dynamics of the cell [28].

Effects of IR on Proteins

Apart from nucleic acids and lipids, ionizing radiation can induce changes in the expression and activity of proteins as well. Recent studies have shown that protein expression and protein-protein interaction are affected by doses as low as 1 Gy, contrary to the traditionally held 10 Gy threshold [28]. At 2-8 Gy inactivation of redox-sensitive enzymes, such as catalase, is observed. The most important effect of IR on proteins though is the induction of oxidative or reductive post-translational modifications (PMT). Oxidation of proteins can be of several types, such as oxidative cleavage of the protein backbone and amino-acid side chains, carbonylation and direct amino-acid oxidation (e.g., for Cysteine and Methionine) [28].

In the case of the *radical cleavage of the protein backbone and amino-acid chains*, $^{\bullet}$OH radicals, generated via radiation, initiate cleavage of the protein backbone and react with all of the amino-acids on the chain at an extremely high rate. In a similar way, $^{\bullet}$OH abstracts hydrogen atoms from aliphatic amino-acid side chains at all carbon sites. These reactions can lead to fragmentation of the protein chain [28]. *Carbonylation*, on the other hand, refers to the process of post-translational addition of carbonyl moieties to amino-acid side chains, as a result of radiation-generated ROS, usually occurring via metal catalysis. Carbonylation produces a variety of modified amino acids that are capable of inducing damages in the protein backbone [30]. It is believed to be a selective and irreversible process and it is involved in the pathophysiology of many diseases, including chronic lung disease, diabetes and neurodegenerative disorders [28]. *Methionine and Cysteine oxidation* occurs when radiation generates reactive oxygen species (ROS) that oxidize methionine or cysteine, forming products like methionine sulfoxide (MetO) and sulfenic acid. This oxidation can affect protein function, signaling pathways, and may contribute to diseases like Parkinson’s [28].

The effects of IR-induced reductive processes on proteins are less investigated than the oxidative equivalent. Reducing radicals generated by radiation, such as hydrogenated electrons (e_{aq}^-) and $H^{\cdot}$ can modify proteins by targeting sulfur-containing amino acids like methionine and cysteine. These modifications include radical formation, amino acid conversion and potential protein-lipid damage [28].

1.5. Basics of Transmission Electron Microscopy (TEM)

Transmission electron microscopy (TEM) is a microscopy technique in which the image is generated when a beam of electrons is transmitted through a sample. The first TEM microscope was invented in 1930s by Ernst Ruska and Max Knoll and since then it has been irreplaceable in biological research, due to its near-atomic-level resolution; much greater than that of its optical counterparts.

The exceptional resolution of TEM microscopes is due to the smaller de Broglie wavelength of electrons compared to photons. Because of this, they are able to capture extreme levels of detail and as they can achieve magnification of objects up to 2 million times [1]. TEM microscopes find applications in various fields, including cancer biology and virology, material science, nanotechnology, semiconductor research, etc.

1.5.1. Principles of operation

The TEM microscope (see Figure 1.15), instead of light, makes use of a high voltage coherent electron beam of about 60-120 kV for biological applications. The electrons are emitted from the heating *cathode filaments* of an electron gun at the top of the TEM system and then travel through an ultra-high vacuum tube (10^{-1}-10^{-5} Pa). The cathode ray then passes through an *anode* and *alignment coils* which accelerate and focus the beam. A *condenser aperture* excludes the high angle electrons and a magnetic *condenser lens* induces a helical convergence to the beam before it reaches the specimen. The electron beam then hits the very thin specimen (around 60-90 nm) which is placed upon a grid-like stage. There, they either scatter or pass through it and reach at a *fluorescent screen* at the bottom of the microscope. In this way, an image is created where the regions less dense in electrons are represented in a lighter tone, while the denser regions bear a darker shade [1].

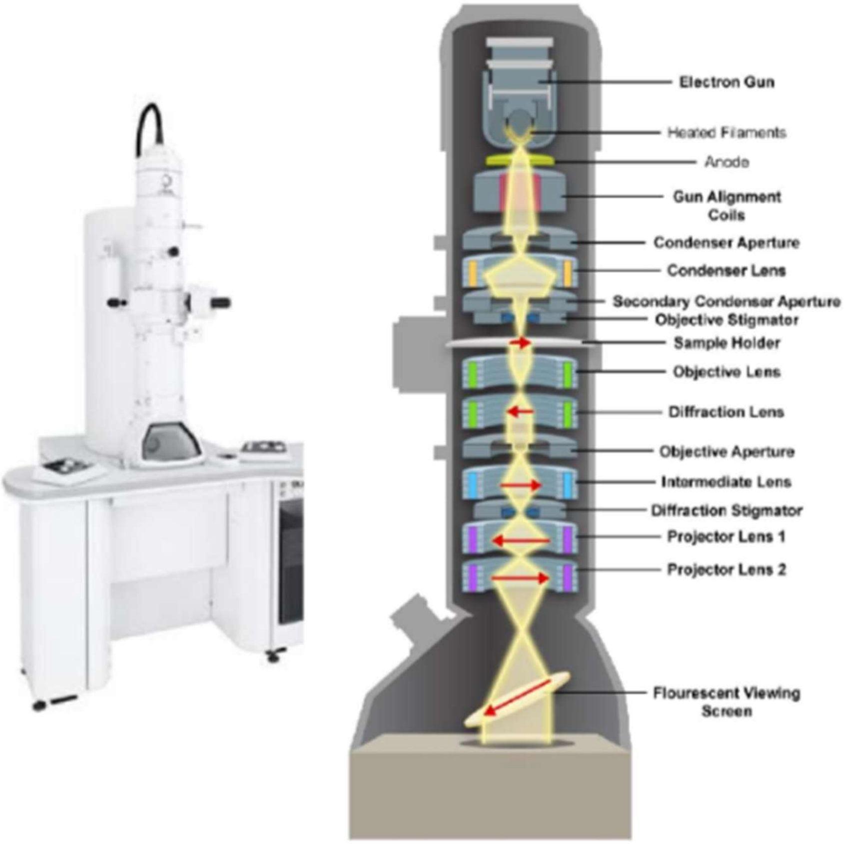

Figure 1.15 The architecture of a TEM microscope [1].

1.5.2. Imaging Process and Preparation of Samples

The image produced by the electron beam is focused on the *objective lens*. A *diffraction lens* then applies Brag scattering on the electrons while the *objective aperture* is used to select or exclude the portion of the sample that produced the scattering. The *intermediate* and *projector lenses* magnify and calibrate the image before it reaches the fluorescent screen, where it is visualized. This image, apart from direct studying, can also be photographed with a digital camera and be exported as a TIFF file [1].

Living matter consists of approximately 80% of water, so, without the necessary preparation of the specimen, every trace of liquid would be removed in the high vacuum of the tube. Additionally, as biological matter consists mainly of light elements, such as carbon and hydrogen, the high-speed electrons do not interact strongly with its atoms. These reasons create the need for sampling preparation. Conventional sample preparation consists of chemical fixation, sample dehydration (at room temperature or at 4 ^{o}C) and embedding with epoxy or acrylic resin. Alternative methods to chemical fixation include cryofixation via vitrification, where the sample undergoes freezing through various techniques [1].

1.6. Principles of Morphometry

Morphometry, in general terms, is the analysis of *form*, encompassing the size and shape of an object, in a quantitative way. The objects analyzed are usually organisms and morphometry gives insight of varied biological interest, such as developmental changes, the impact of radiation or mutations on shape, registering the fossil record, etc. The purpose of morphometric analysis is to statistically test hypotheses about the factors that affect shape and from this data to deduce something of their ontogeny or function.

In the context of morphometry, one might analyze length, width, mass, angles, area and ratios. For the analysis of the data and the visualization of the shape alterations, various statistical methods can be used. These can be bar graphs and other diagrams showing the statistics of the quantity under study. Morphometry can be useful in exploring patterns of variations, relative alterations, population means as well as deviations of individuals from it. For the purposes of the present thesis, morphometry is used to study the ultrastructural changes induced by ionizing radiation on the mitochondria of rat intestinal tissues.

1.7. Basics of Machine Learning

1.7.1. General background

The field of machine learning (ML) belongs to the more general field of *Artificial Intelligence*. Artificial intelligence encompasses any technique that enables computers to perform tasks that mimic human behavior and problem-solving skills. As such, it is concerned with a variety of problems, including reasoning, learning, planning, perception and communication [31]. ML, specifically, refers to a method of computer learning, where the computer automatically learns meaningful relationships and patterns from examples and observations, without the need of explicit human intervention. This is achieved through the application of algorithms that iteratively extract information from problem-specific training data, finding hidden insights and patterns without having been previously programmed to do so [20]. Proven successful and reliable, especially in tasks involving high-dimensional data, machine learning faces rapid development and shows a performance that excels human capabilities in many areas. For this reason, it finds various applications in a vast number of fields, such as molecular biology, clinical practice, speech and image data analysis, electronic marketing and many others [31,32].

Machine learning is generally divided into three types: *supervised* learning, *unsupervised* learning and *reinforcement* learning. In the case of supervised learning, computers are called to learn how to predict the class or the value of unknown data after undergoing training with an observed set of data. To achieve this, we provide the computer model with a set of input-output pairs that calibrate its parameters and serve as examples for future, unknown data [31]. Unsupervised learning, on the other hand, is the task where computers identify unknown patterns in data, like groups or classes, without any pre-existing knowledge of the output labels. The goal is to find structural information of interest, like common properties or data representations between elements, based entirely on the input [31]. Lastly, in reinforcement learning, rather than supplying input-output pairs, we outline the current state of the system, define a goal and offer a set of permissible actions along with their environmental constraints. The machine learning model then autonomously navigates the process of reaching the goal, using trial and error to maximize the reward [31]. Supervised learning methods, based on the type of their output, are classified as *regression methods*, when the output is numerical, and as *classification methods* when the output is categorical and include linear and SVM regression, decision trees, random forests, k-neighbors classification, Bayesian methods, neural networks etc. Unsupervised learning methods, based on their goal, are divided into *clustering* (in which the model searches for groups/clusters of elements with common properties) and *dimensionality reduction methods* (in which the number of features or variables is reduced, while preserving the essential information) and include k-means, UMAP and others [32]. A taxonomy of the different methods of ML can be seen in figure 1.14.

1.7.2. Artificial neural networks and deep learning

Inspired by the way that biological neurons process information, artificial neural networks is a family of machine learning algorithms of flexible structure that can find applications in all three types of ML. They consist of mathematical representations of interconnected processing units called artificial neurons. Their function mimics that of their biological counterparts, as they transmit signals in the way brain synapses do. These signals are multiplied by weights that are constantly adjusted during the learning process. Subsequent neurons only process signals that have exceeded a certain threshold, determined by an activation function. The neural network is structured in layers: An input layer receives the data input, an output layer produces the output and a number of intermediate hidden layers creates a non-linear mapping between input and output. The number of layers and neurons, the learning rate and the activation function are called *hyperparameters* of the system and cannot be learned by the model itself; they have to be decided manually in order to be optimal for each situation [31].

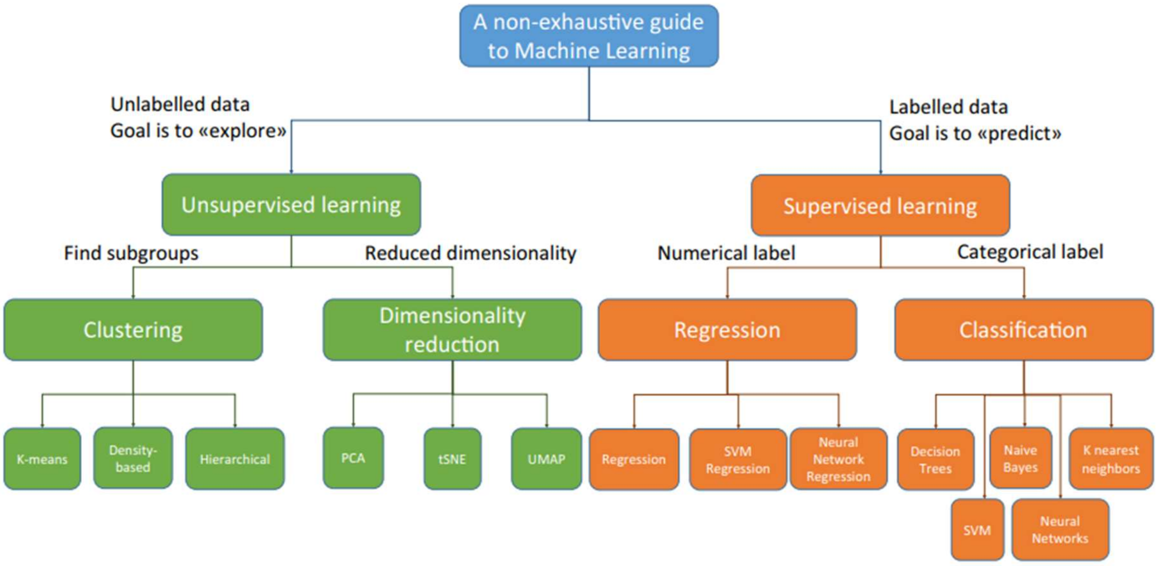

Figure 1.16. Taxonomy of the main machine learning algorithms [32].

Neural networks, based on their architecture, can be of various types, such as recurrent neural networks, long short-term memory networks, gated recurrent networks, convolutional neural networks, generative models and others [32]. Deep neural networks (DNNs) usually refer to neural networks with more than one hidden layers, organized in deep complex architectures. In addition, DNNs consist of more advanced neurons than simple neural networks, meaning that they use advanced operations, such as convolutions or multiple activation functions, between the 'synapses', instead of a simple activation function [31]. Due to these features, DNNs are able to automatically discover complex representations for the corresponding learning tasks, a process known as *deep learning*. The basic difference of deep learning algorithms from other ML algorithms, known as *shallow machine learning*, is that they are considered "black box" models because they involve multiple layers of processing, making it difficult to interpret how exactly they arrive at their predictions. The complexity of these models often obscures the internal decision-making process, making them less transparent and harder to explain. In contrast, in shallow machine learning, the decision-making processes are relatively transparent and easy to understand and therefore they are considered "white box" models [31].

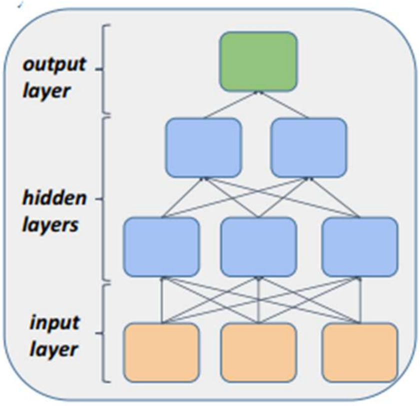

Figure 1.17. Basic architecture of a neural network [31]

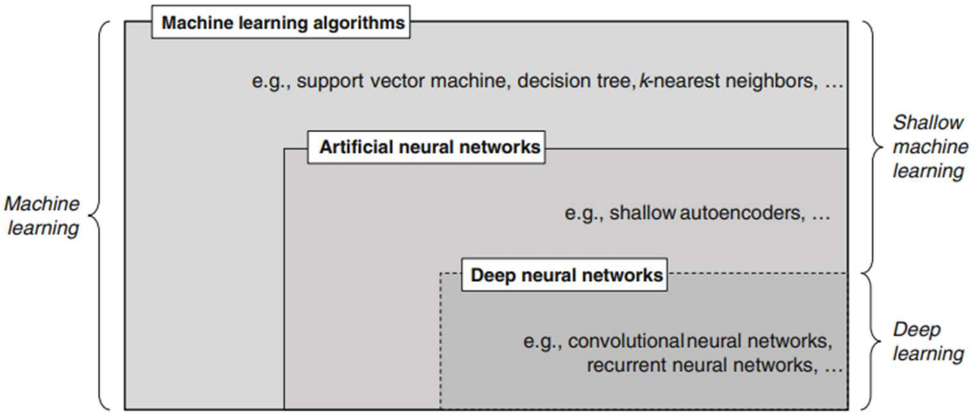

Figure 1.18. Venn diagram showing the relationship between machine learning, neural networks and DNNs.[31]

Deep learning is suitable for addressing problems with large and high dimensional data, like text, image, video, speech and audio. In these domains, DNNs outperform shallow ML algorithms and exhibit superhuman performance. However, in problems with a lower number of dimensions, or limited train data availability, shallow ML can provide superior results, in addition of being more easily explainable. Furthermore, tasks that require strong AI capabilities, such as actual understanding or intentionality, have proven unsolvable in the context of deep learning [31].

1.7.3. Analytical model building

In this section, we analyze briefly the main process behind building a machine learning model. In general, this process consists of the following steps: data input, pre-processing of the data and feature extraction, model building and training, and evaluation of the model performance [33].

For a supervised machine learning model, as the one of interest for the present thesis, input data consist of input-output pairs. The first thing after loading the data is to inspect them. This is a crucial step as it gives us a more solid understanding of the nature of the data and the ability to visualize them, if they are images e.g. Furthermore, we have to ensure that there are no missing or misaligned data and that the inputs correspond to the correct outputs, otherwise the model training will fail.

Loaded data need to be in a form which is compatible with the requirements of the ML model. In addition, not all features of the data are useful for the specific task of interest. This is why data pre-processing and feature extraction are important. With a series of custom functions, data are transformed in a way that keeps (‘extracts’) all the crucial information for the training, while extra information is discarded. These transformations usually come with a significant decrease in the size of the data, making them easier to handle. Resizing and normalization might also be applied to conform the data with the model requirements. In cases where the number of input data is insufficient, or where we want to provide the model with a more spherical approach on the data, *data augmentation* can be applied. This refers to series of transformations, like rotations and flips, that extract extra useful information from the data, not accessible in their original form [31,33].

In the classical approach of building an ML model, the next step is usually the *test-train split*. The original number of available data is divided into train and test sets, with a ratio defined by the programmer. The train data will be used as training examples for the model to learn, while test data will be given to the model after training is completed, in order to evaluate its performance [33].

In the building phase, one should choose and implement the architecture of the model, which can be either customized or imported from an existing source. There are different architectures suitable for different tasks and with variable degrees of complexity. After defining the model, it can be trained by fitting on the train data set. An important step in this point is the *definition of the hyperparameters* of the model. These are parameters, such as the learning rate and the activation function, that should be imported manually in the system, as they practically define its foundations. The optimization of the hyperparameters can be done during an optimization routine, letting the model try different values of them and seeing which ones give the best results [31,33].

After training the model, the test data set is given to it as input, in order to evaluate it. Specialized evaluation functions compare the output of the model with the ground truth outputs of the test set, giving an assessment of its performance [31,33].

1.8. Aim of Study

In the present study, healthy intestinal tissues from mice were exposed to proton beam radiation (both conventional and flash) and then after processing they were photographed with a TEM microscope. Tissues were processed and studied at three different time points post IR, namely 30 minutes, 4 hours and 18 hours. The aim of this study was twofold. Firstly, mitochondrial damage was estimated and compared for conventional and flash radiotherapy. To do this, morphometric analysis is performed, extracting the mean population and area of healthy and damaged mitochondria for each condition.

Secondly, an attempt was made to build and train a machine learning model in order to automatically segment the mitochondria out of a given electron micrograph. For this purpose, a deep learning neural network model was utilized and fed with the dataset analyzed on the first part. The aim was to create an automatic model for segmentation that could be used for future biological analysis.

Chapter 2: Materials and Methodology

2.1. Irradiation Procedure

All animal studies performed for the purposes of this project were reviewed and approved by the Institutional Animal Care and Use Committee of University of Pennsylvania. Female 13-week-old C57BL/6J mice (Jackson Labs, Bar Harbor, ME) were used and they were anesthetized using isoflurane in medical air. The mice were subjected to 15 Gy whole abdominal FLASH PRT (130 Gy/s) versus standard PRT (0.88 Gy/s), using a 230 MeV (range ~32.0 g/cm2) proton beam generated by an IBA Proteus Plus Cyclotron (Louvain-La-Neuve, Belgium) to a fixed research beam line [34]. The irradiation field was square, 20 x 20 mm. Field uniformity was verified with radiographic film (EBT3, Ashland Advanced Materials, Bridgewater, NJ, USA). Dose was measured with a calibrated NIST-traceable Advanced Markus Chamber (PTW, Freiburg, Germany). All the aforementioned radiative experiments were performed by Dr. Michele M. Kim, Assistant Professor of Radiation Oncology at the Hospital of the University of Pennsylvania.

The total number of experimental conditions that were analyzed was 14. Experiment was performed twice in order to enhance the reliability of the results. Each experiment had seven conditions. One condition was always the *control group*, where no irradiation had been taken place, and the other six conditions corresponded to irradiated tissues fixed at different time-points (30 minutes, 4 hours and 18 hours post

IR). Irradiated tissues were exposed to either conventional dose rate proton radiation or ultra-high dose rate (FLASH) proton radiation (see below Table 2.1).

	Conventional Dose Rate			FLASH			Control
GROUP 1	30 min	4 h	18 h	30 min	4 h	18 h	No IR
GROUP 2	30 min	4 h	18 h	30 min	4 h	18 h	No IR

Table 2.1. The different post-IR timepoints measured in the experiment. Along with the two not irradiated control groups, there is a total of 14 conditions.

2.2. Transmission Electron Microscopy

2.2.1. Operation

The observation and photography of the samples was performed using the JEOL JEM 2100plus TEM, operated at 80 kV and equipped with a CMOS Camera Gatan OneView.

2.2.2. Tissue Sample Preparation

The intestinal tissues were excised at 30 minutes, 4 hours, and 18 hours post IR and were immediately fixed for 2 hours, at room temperature, by immersion in 2.5% glutaraldehyde (in 0.01M PBS) for downstream analyses of morphological changes. Following fixation, the tissues were accordingly washed in 0.01M PBS. Finally, they were cut into smaller cubes (1-2 mm) and stored in 0.01M PBS, in tubes at 4 ºC. Tissue fixation was performed by Dr. Anastasia Velalopoulou, Research Associate at Dr. Koumenis Lab (Department of Radiation Oncology, Perelman School of Medicine, University of Pennsylvania). After fixation, the standard procedure for TEM processing of tissues was followed, i.e., dehydration, infiltration and embedding in epoxy resin. Epoxy blocks were then cut into thin sections (~80 nm thickness), which were mounted on copper grids, stained with uranyl acetate and lead citrate, and finally observed and photographed with the JEM 2100plus TEM. The TEM tissue processing, as well as the TEM observation and photography was performed by Dr. Ioanna Tremi and Assist. Prof. Sofia Havaki, at the Laboratory of Histology – Embryology, Medical School of Athens, National and Kapodistrian University of Athens.

2.3. Morphometry and Data Acquisition

The morphometric analysis was done by using the *Image J* software (see Figure 2.1). Image J is a powerful tool for analyzing photographs and extracting features from images. The analysis performed can be seen as three separate tasks: mitochondria classification, mask creation and measurement of areas.

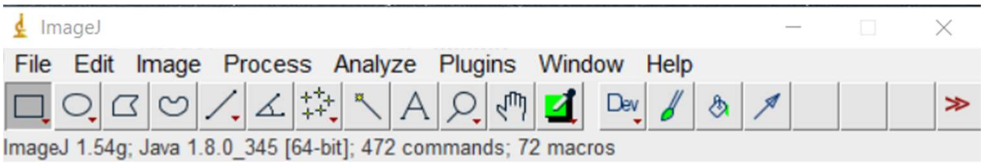

ImageJ 1.54g; Java 1.8.0_345 [64-bit]; 472 commands; 72 macros

Figure 2.1. The Image J toolbar, showing its different functions

2.3.1. Mitochondria classification

In each electron micrograph, the total number of mitochondria was counted. Then, each mitochondrion was classified as either healthy or damaged, based on their morphological features. As a general rule, mitochondria that were considered as damaged, had a more swelled phenotype, they appeared larger, they sometimes didn’t have well preserved structure, and they also had fragmented outer membrane or cristae which resulted in “white areas” (see Figure 2.2). Mitochondria can be recognized, among other organelles and vesicles, by their size and shape, as well as by their cristae and characteristic double membrane. The total number of cells in each electron micrograph was also counted and registered along with all the aforementioned measurements in an excel file.

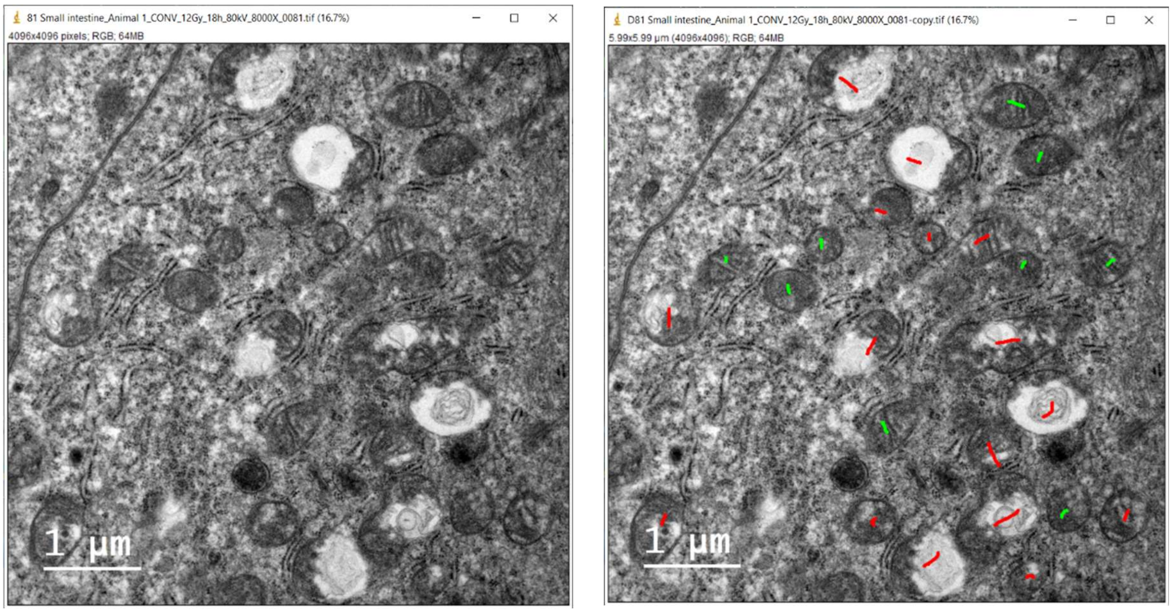

Figure 2.2. Representative electron micrographs of mouse intestinal tissues (small) 18h post IR. Damaged mitochondria are noted in red, while healthy ones in green (right).

2.3.2. Mask creation and Area measurements

Using the 'freehand selection' tool of Image J, the periphery of each mitochondrion was carefully outlined. By right clicking inside the selection and selecting 'add to overlay', the outline was fixed on the background of the image (see Figure 2.3). After selecting and adding to overlay all the mitochondria out of an image, a binary mask could be created (see Figure 2.4) by clicking *Edit->Selection->Create Mask*. The mask would be used to extract area features, as explained below, and then saved in order to be used later in the training and testing of the machine learning model.

In order to measure the area, scaling was necessary. In general, images came in various size scales that could be seen in the down left or down right corner of it. With the use of 'straight line' tool, one could draw a line of the same length as the scale bar noted in the image. Then, by clicking *Analyze->Set Scale*, a new tab appears where, in the section 'Known Distance', one should put the scale indicated in the image (see Figure 2.5). In this way, the length of the drawn line in pixels corresponds to the actual length indicated by the scale of the image and the system is properly set up and ready for measuring the area.

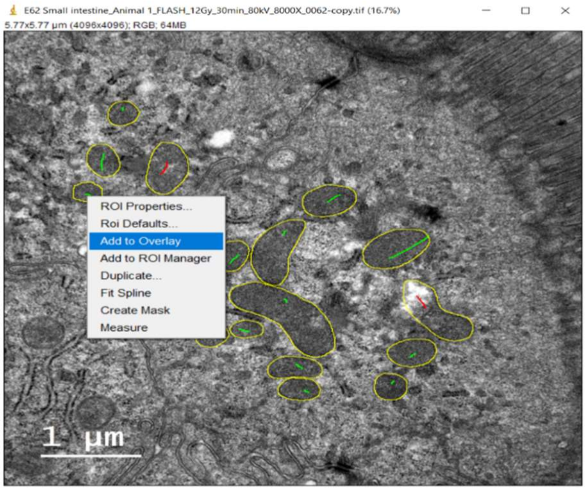

Figure 2.3. Selected peripheries of mitochondria. The process of adding them to overlay can be seen.

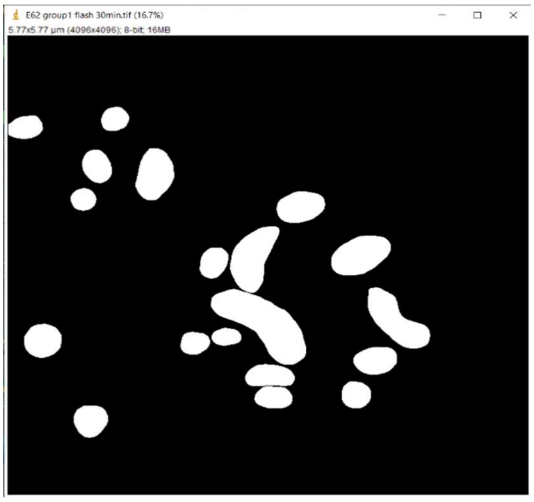

Figure 2.4. Example of a binary mask, generated with Image J

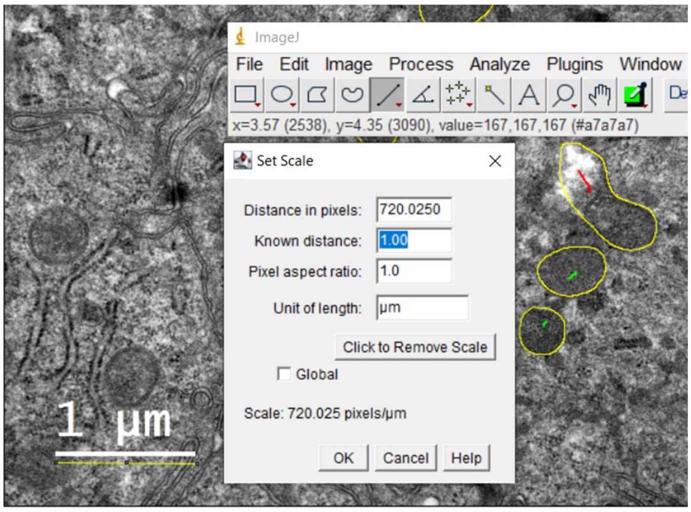

x=3.57 (2538), y=4.35 (3090), value=167,167,167 (#a7a7a7)

Distance in pixels: 720.0250
Known distance: 1.00
Pixel aspect ratio: 1.0
Unit of length: µm
☐ Global
Scale: 720.025 pixels/µm

Figure 2.5. Scaling: Drawing a line of the same length as the scale bar and setting the knowing distance indicated by the image.

After scaling the image, the macro shown in figure 2.6. was installed in the 'Plugins' section. By running this macro for the mask created in the previous step, we could get an output of the total area covered by the mitochondria contained in the image, as well as a file containing the list of the areas covered by each one of them separately.

Because we were interested in the total area covered by the healthy and the damaged mitochondria respectively, the same macro was applied to a second mask, which contained only the healthy mitochondria. In this way, the total area of the damaged mitochondria could also be found by a simple abstraction. This second mask was not saved, as it contained no additional information needed for the machine learning algorithm. Lastly, we were interested in the total area of the cytoplasm of the image. To measure this, all of the area containing cytoplasm was selected (by subtracting the nuclei and extracellular spaces) via the ‘freehand selection’ tool and then we clicked *Analyze->Measure* (see Figure 2.7). In the cases where the image appeared dim or blurred, brightness and contrast were adjusted through Image J as needed.

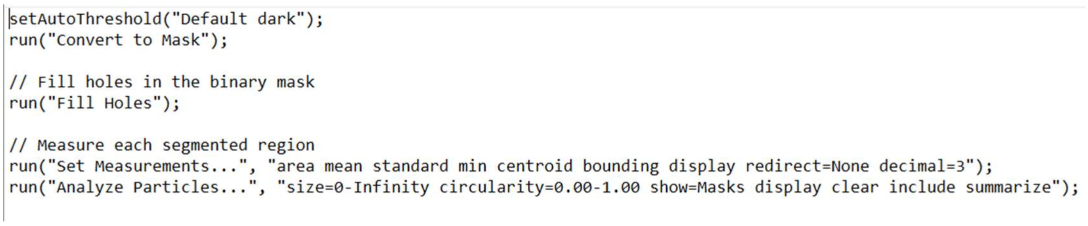

```
setAutoThreshold("Default dark");
run("Convert to Mask");

// Fill holes in the binary mask
run("Fill Holes");

// Measure each segmented region
run("Set Measurements...", "area mean standard min centroid bounding display redirect=None decimal=3");
run("Analyze Particles...", "size=0-Infinity circularity=0.00-1.00 show=Masks display clear include summarize");
```

Figure 2.6. The macro used in order to extract the areas of the mitochondria. After being installed in the Plugins section, it is run by clicking on its name.

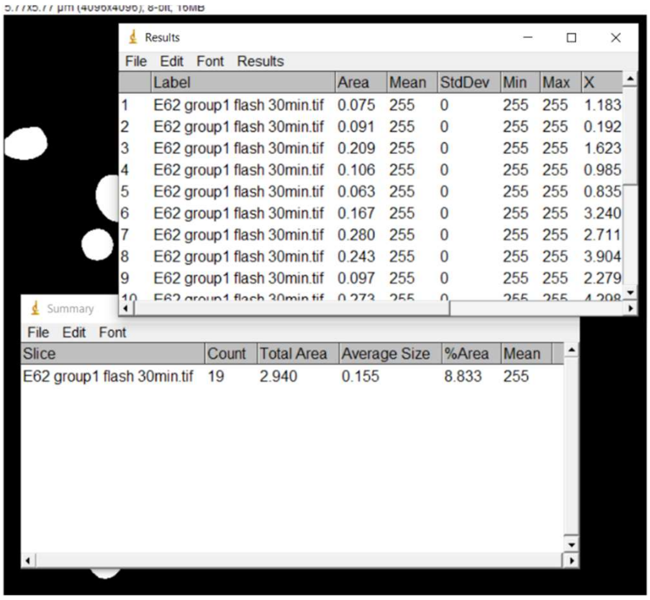

	Label	Area	Mean	StdDev	Min	Max	X
1	E62 group1 flash 30min.tif	0.075	255	0	255	255	1.183
2	E62 group1 flash 30min.tif	0.091	255	0	255	255	0.192
3	E62 group1 flash 30min.tif	0.209	255	0	255	255	1.623
4	E62 group1 flash 30min.tif	0.106	255	0	255	255	0.985
5	E62 group1 flash 30min.tif	0.063	255	0	255	255	0.835
6	E62 group1 flash 30min.tif	0.167	255	0	255	255	3.240
7	E62 group1 flash 30min.tif	0.280	255	0	255	255	2.711
8	E62 group1 flash 30min.tif	0.243	255	0	255	255	3.904
9	E62 group1 flash 30min.tif	0.097	255	0	255	255	2.279
10	E62 group1 flash 30min.tif	0.273	255	0	255	255	4.208

Slice	Count	Total Area	Average Size	%Area	Mean
E62 group1 flash 30min.tif	19	2.940	0.155	8.833	255

Figure 2.7. The output of the application of the macro to a mask. The up tab contains the areas of each of the mitochondria of the image and the down tab the total area that they cover

2.4. Statistical Analysis of the Data

The analysis that followed data acquisition was the same for each of the fourteen conditions of the data. Firstly, the average percentage of normal and damaged mitochondria per squared micrometer (μm^2) was calculated. To do this, the number of normal (or damaged) mitochondria per μm^2 was found for each micrograph and the percentage was measured as the sum of the number of normal (or damaged) over the sum of the total number of mitochondria per μm^2. The error was assumed to be the standard statistical error:

$$SE = \frac{st.deviation}{\sqrt{n}} \qquad (2.1)$$

Because the percentages were calculated as ratios of sums, the following formula was used for their variance, derived from first-order Taylor expansion:

$$Var = \left(\frac{\mu_1}{\mu_2}\right)^2 \left(\frac{\sigma_1^2}{\mu_1^2} + \frac{\sigma_2^2}{\mu_2^2} - 2\frac{Cov(\mu_1\mu_2)}{\mu_1\mu_2}\right) \qquad (2.2)$$

Where, $\mu_{1,2}$ are the mean values and $\sigma_{1,2}^2$ are the variances of the datasets that refer to the sums.

Secondly, the average area per mitochondrion was calculated, separately for healthy and damaged ones, for each condition. This was done by dividing the total area covered by the normal (or damaged) mitochondria over their number. Again, for the error, the expression (2.1) was used.

Because we had two groups of data at our disposal, each condition of the first group had an equivalent condition from the second group. In order to combine the information provided by the equivalent conditions from the two groups, their combined average percentage and area were calculated, using the basic statistical formula for the combined average of two datasets:

$$\bar{X} = \frac{n_1\overline{X_1} + n_2\overline{X_2}}{n_1 + n_2} \qquad (2.3)$$

Where $\overline{X_1}$, $\overline{X_2}$ are the averages of the two sets and n_1, n_2 the number of their elements. The combined standard errors were also calculated using the following formula:

$$SE = \sqrt{SE_1^2 + SE_2^2} \qquad (2.3)$$

Using these information, a series of graphs were plotted to better understand the results. Finally, in order to verify if any differences that existed in the percentage and area of normal and damaged mitochondria between the conventional and FLASH dose rates were statistically significant, a series of *t-tests* were performed. Those were performed separately for each condition, at thirty minutes, four hours and eighteen hours after exposure, with a significance level of $a = 0.1$.

2.5. Segmentation of Mitochondria using Machine Learning

The analysis performed on the previous steps resulted in a dataset of total 577 TEM images and their corresponding masks. Both the images and the masks had dimensions of 4096×4096 pixels, with the images being in RGB, while the masks being in binary format. All the images were saved as TIFF files.

The total number of images and masks from the 14 conditions were saved in two separate folders, each containing 577 items. The two folders were sorted (with their items renamed when necessary) in such a way that an image and its corresponding mask were found in the equivalent positions of their respective folders. Correct pairing between images and masks (labels) is a very crucial step for the success of the model and cannot be omitted.

The code for image segmentation was written in Python, using a Jupyter notebook (anaconda 3). Jupyter is an open-source web-based interactive platform for creating computational documents in various programming languages [35].

2.4.1. Importing the libraries and the data

Firstly, the following Python libraries were imported on our environment:

NumPy: Package used for scientific computing, providing various calculations and support for matrices and multi-dimensional arrays.

Matplotlib: Package for plotting graphs and diagrams in Python.

<u>Cv2 and Image</u>: Libraries for image processing.

<u>OS</u>: Module for interacting with the operating system, including file and directory operations.

Following this, the paths to the image and mask directories were defined, as seen in Figure 2.8.

```
import os
import cv2
from PIL import Image
import numpy as np
from matplotlib import pyplot as plt


image_directory = 'E:\\Electron Microscopy Photos\\diplomatiki\\Image_Folder'
mask_directory = 'E:\\Electron Microscopy Photos\\diplomatiki\\Mask_Folder'
```

Figure 2.8. Importing python libraries and defining data directories.

2.4.2. Data preprocessing

As part of data preprocessing, the original images and masks were resized to 256×256 pixels and converted in the proper format to be used by the model [36]. For these purposes, we first defined a SIZE parameter equal to 256, as well as two empty lists to contain the transformed data (*see Figure 2.9*).

For all TIFF files in the Image directory, the full path to the image was constructed. Afterwards, the image was read in color (number 3 indicates RGB). A check for if the image had been read correctly was added, to ensure that all images contain valuable information and to prevent bugging. After checking, the image array was converted to a PIL Image object and then resized to 256×256. Following resizing, it was converted to a NumPy array and appended at the ‘image_dataset’ list. Finally, after all images had been stored at ‘image_dataset’, the list itself was converted to a NumPy array of shape (577, 256, 256, 3), where the first argument refers to the number of images, the second and third at their dimensions and the fourth at the number of their channels.

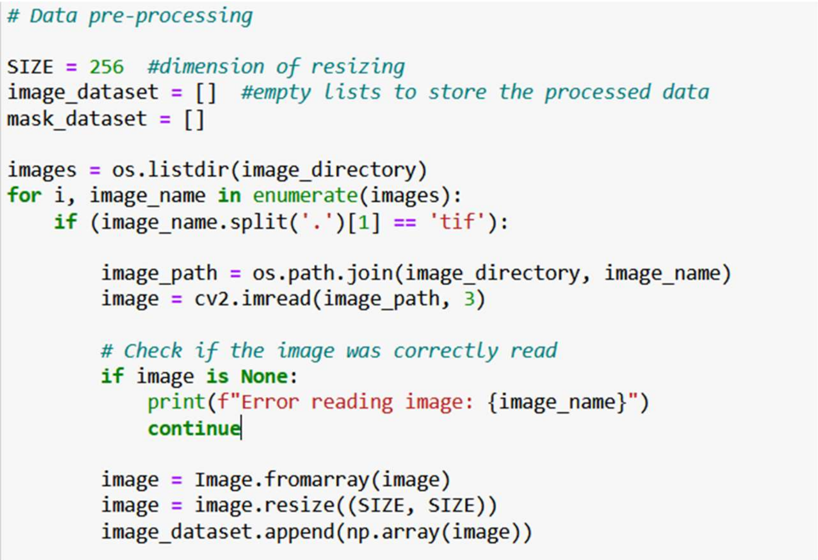

```python
# Data pre-processing

SIZE = 256  #dimension of resizing
image_dataset = []  #empty lists to store the processed data
mask_dataset = []

images = os.listdir(image_directory)
for i, image_name in enumerate(images):
    if (image_name.split('.')[1] == 'tif'):

        image_path = os.path.join(image_directory, image_name)
        image = cv2.imread(image_path, 3)

        # Check if the image was correctly read
        if image is None:
            print(f"Error reading image: {image_name}")
            continue

        image = Image.fromarray(image)
        image = image.resize((SIZE, SIZE))
        image_dataset.append(np.array(image))
```

Figure 2.9. Pre-processing of images

The exact same procedure was followed for pre-processing the masks, with the addition of an extra line to ensure that the mask is in binary format. Furthermore, after converting the mask list to a NumPy array, we expanded its dimensions by one along the third axis, because the code tends to omit the channel dimension (*see Figure 2.10*) [36]. As a result, the final array of the masks had the shape (577, 256, 256, 1).

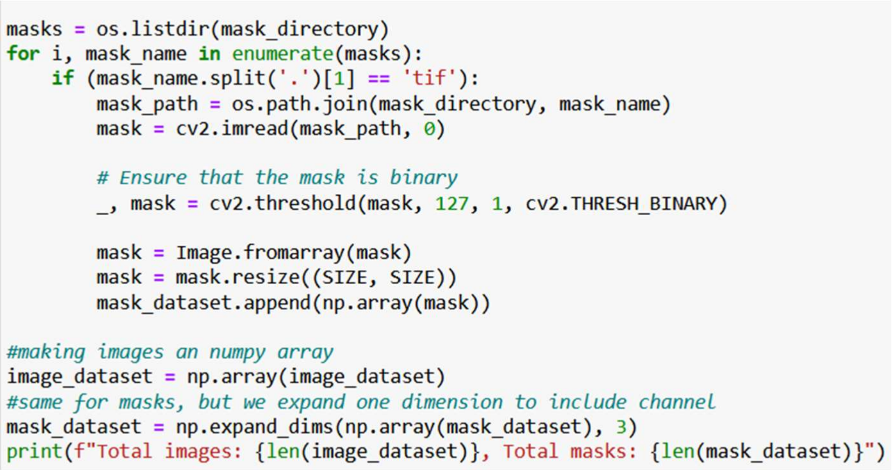

```python
masks = os.listdir(mask_directory)
for i, mask_name in enumerate(masks):
    if (mask_name.split('.')[1] == 'tif'):
        mask_path = os.path.join(mask_directory, mask_name)
        mask = cv2.imread(mask_path, 0)

        # Ensure that the mask is binary
        _, mask = cv2.threshold(mask, 127, 1, cv2.THRESH_BINARY)

        mask = Image.fromarray(mask)
        mask = mask.resize((SIZE, SIZE))
        mask_dataset.append(np.array(mask))

#making images an numpy array
image_dataset = np.array(image_dataset)
#same for masks, but we expand one dimension to include channel
mask_dataset = np.expand_dims(np.array(mask_dataset), 3)
print(f"Total images: {len(image_dataset)}, Total masks: {len(mask_dataset)}")
```

Figure 2.10. Pre-processing of masks. Notice the difference in reading the masks, having a zero value where images had a value of 3, indicating they are binary.

Due to the limited number of data that we had at our disposal for training the model, two tactics were followed to enhance the results: data augmentation and the use of a neural network architecture with pre-trained weights. A pre-trained network (often called a *backbone* in the context of machine learning) is a model already trained in a broad dataset to recognize various patterns, edges, textures, and shapes. This knowledge is transferable and can be applied to different tasks. Therefore, instead of training our model from scratch, we used this pre-trained network and fine-tuned it by training it on our data. In this way, features could be more easily extracted than if we had used a brand-new model architecture from the beginning.

In order to use the pre-trained model, an additional library was installed and imported, that of *segmentation models*. *Segmentation models* library contains pre-built models and utilities for image segmentation tasks. The backbone architecture chosen is called '*resnet34'* and it is a residual network with thirty-four layers [36]. To prepare our data to be used by the network, a preprocessing function from *segmentation models* library was used. This function performed normalization of the data, specifically for the requirements of the backbone model (*see Figure 2.11*).

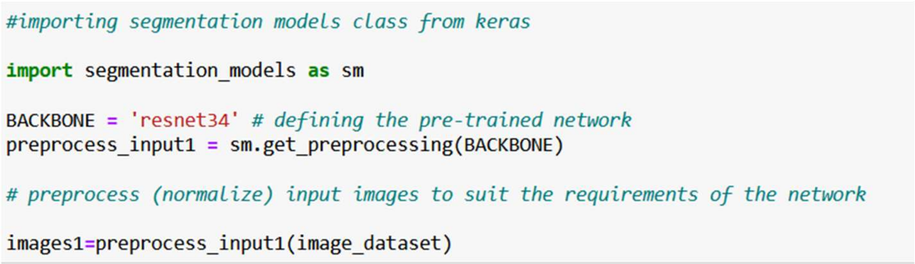

```
#importing segmentation models class from keras

import segmentation_models as sm

BACKBONE = 'resnet34' # defining the pre-trained network
preprocess_input1 = sm.get_preprocessing(BACKBONE)

# preprocess (normalize) input images to suit the requirements of the network

images1=preprocess_input1(image_dataset)
```

Figure 2.11. Preparing the data to enter the pre-trained 'resnet34'.

Following this, with the aid of *train_test_split* function, we split our dataset in training and testing sets with a test size ratio of 0.25. In figure 2.12, *X_train* corresponds to the image training set, *X_test* to the image test set and *y_train, y_test* are the equivalent for the masks. Testing sets were used both for validation of training performance and for visualizing the final results.

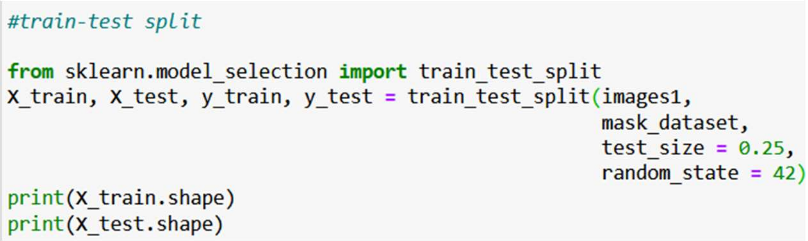

```
#train-test split

from sklearn.model_selection import train_test_split
X_train, X_test, y_train, y_test = train_test_split(images1,
                                                    mask_dataset,
                                                    test_size = 0.25,
                                                    random_state = 42)
print(X_train.shape)
print(X_test.shape)
```

2.12. Test-train split

Lastly, to ensure that our images and masks correspond correctly to each other, we performed a sanity check. For a random image of the *X_train* set, we plotted it alongside its corresponding mask from *y_train* set. The result can be shown in the following figure 2.13.

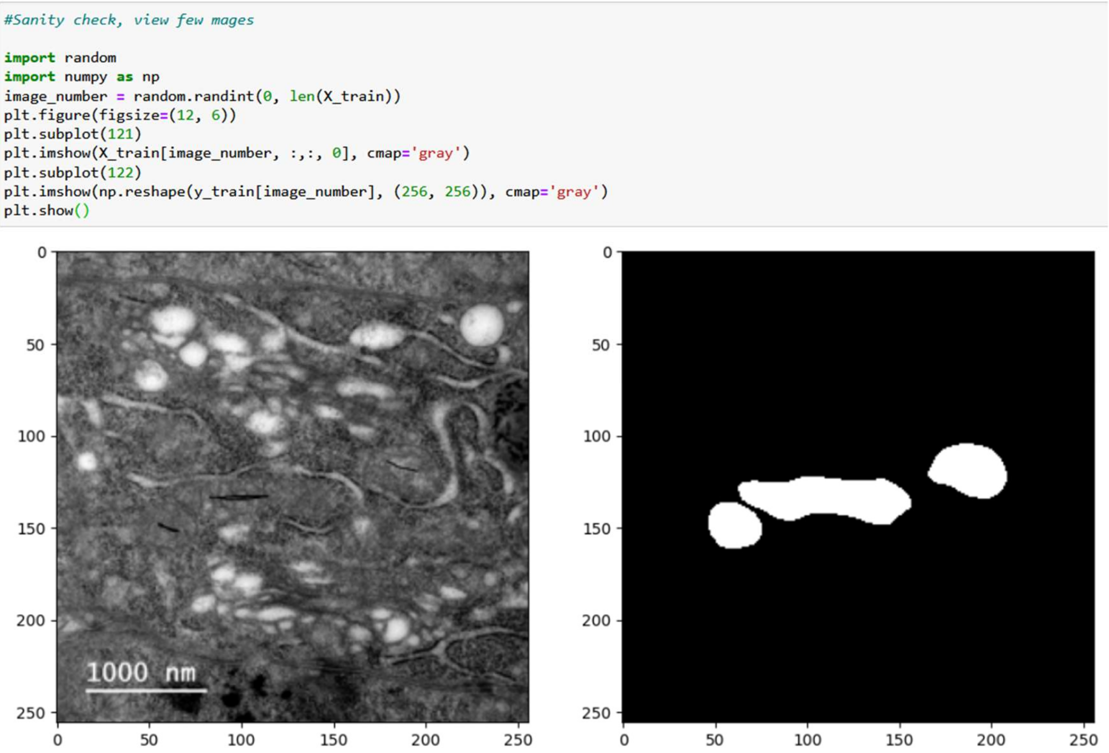

```
#Sanity check, view few mages

import random
import numpy as np
image_number = random.randint(0, len(X_train))
plt.figure(figsize=(12, 6))
plt.subplot(121)
plt.imshow(X_train[image_number, :,:, 0], cmap='gray')
plt.subplot(122)
plt.imshow(np.reshape(y_train[image_number], (256, 256)), cmap='gray')
plt.show()
```

Figure 2.13. Sanity Check after pre-processing. The mask corresponds correctly to the image.

2.4.3. Data augmentation

Data augmentation is the process of artificially enhancing the diversity of existing data with the use of various modifications on them. It is a common practice to increase the performance of the model in cases where the dataset is limited.

To perform data augmentation, *ImageDataGenerator* class was imported. This is a python class allowing for real-time data augmentation. It generates batches of augmented images from the original data and uses this extra data to feed the segmentation model. Setting a constant seed (see figure 2.14) is important because it ensures that *ImageDataGenerator* produces the same augmented images each time the code runs -in a different scenario the model would be unable to learn.

Using two python dictionaries, we specified the parameters for augmenting the input images and masks [36]. We used random rotation up to 90°, horizontal and vertical shift up to 30%, shear transformations with an intensity of 0.5, zooming in or out up to 30%, horizontal and vertical random flipping. Any new pixels created from transformations were filled with reflections from the borders (*fill_mode='reflect'*). Augmentations for masks were identical with those for the images, with the exception of the application of a *lamda function*. This function ensures that all pixel values in the mask (including those generated from augmentations) are either 0 or 1 (see Figure 2.14).

```
seed=24
from keras.preprocessing.image import ImageDataGenerator

img_data_gen_args = dict(rotation_range=90,
                         width_shift_range=0.3,
                         height_shift_range=0.3,
                         shear_range=0.5,
                         zoom_range=0.3,
                         horizontal_flip=True,
                         vertical_flip=True,
                         fill_mode='reflect')

mask_data_gen_args = dict(rotation_range=90,
                         width_shift_range=0.3,
                         height_shift_range=0.3,
                         shear_range=0.5,
                         zoom_range=0.3,
                         horizontal_flip=True,
                         vertical_flip=True,
                         fill_mode='reflect',
                         preprocessing_function = lambda x: np.where(x>0, 1, 0).astype(x.dtype)) #Binarize the output again.
```

Figure 2.14. Defining the parameters for augmenting the images and the masks.

The generators for images and masks were then defined as *image_data_generator* and *mask_data_generator*. These were fitted in the train and test sets of images and masks, always with the same seed value. The four resulting generators (train and validation for images and the same for masks) were as seen in figure 2.15.

A function for combining generators was then defined and used to combine the image and mask train generators, as well as the two validation generators. This resulted in one generator for training and one for validation.

In order to check that the results from data augmentation were all valid, a batch of augmented images and corresponding masks were visualized.

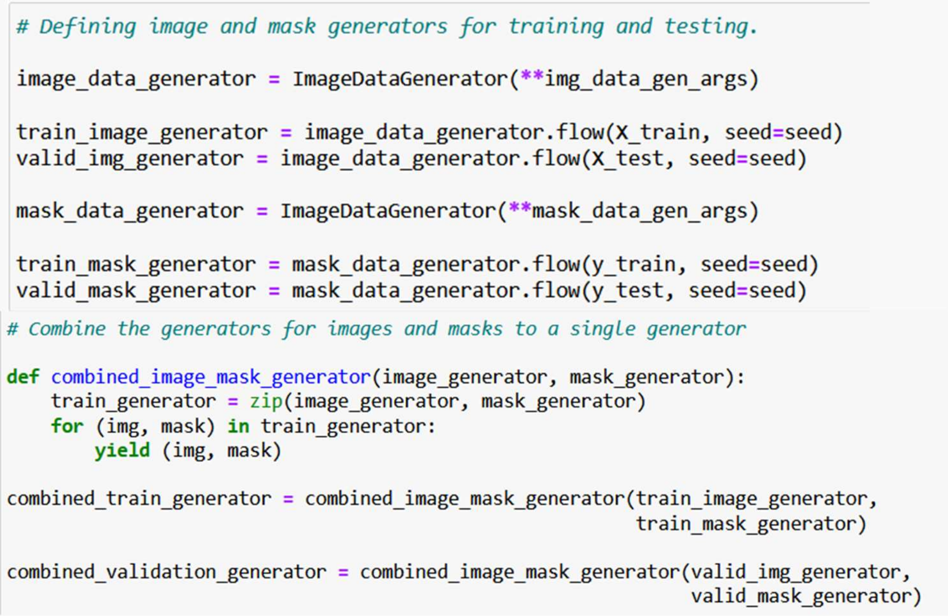

```
# Defining image and mask generators for training and testing.

image_data_generator = ImageDataGenerator(**img_data_gen_args)

train_image_generator = image_data_generator.flow(X_train, seed=seed)
valid_img_generator = image_data_generator.flow(X_test, seed=seed)

mask_data_generator = ImageDataGenerator(**mask_data_gen_args)

train_mask_generator = mask_data_generator.flow(y_train, seed=seed)
valid_mask_generator = mask_data_generator.flow(y_test, seed=seed)
```

```
# Combine the generators for images and masks to a single generator

def combined_image_mask_generator(image_generator, mask_generator):
    train_generator = zip(image_generator, mask_generator)
    for (img, mask) in train_generator:
        yield (img, mask)

combined_train_generator = combined_image_mask_generator(train_image_generator,
                                                         train_mask_generator)

combined_validation_generator = combined_image_mask_generator(valid_img_generator,
                                                              valid_mask_generator)
```

Figure 2.15. Implementation of the image and mask generators for augmentation. The first four generators are combined in two, one for training and one for testing/validation.

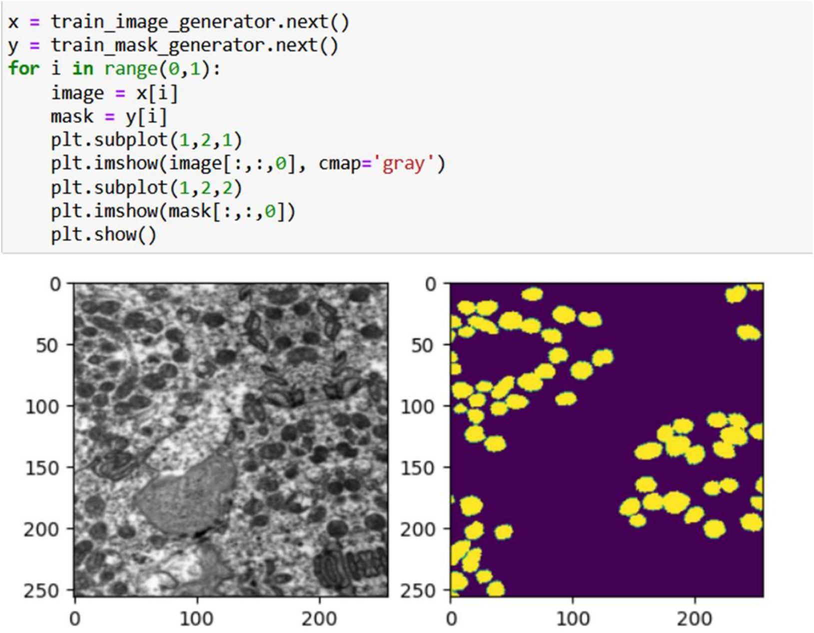

```
x = train_image_generator.next()
y = train_mask_generator.next()
for i in range(0,1):
    image = x[i]
    mask = y[i]
    plt.subplot(1,2,1)
    plt.imshow(image[:,:,0], cmap='gray')
    plt.subplot(1,2,2)
    plt.imshow(mask[:,:,0])
    plt.show()
```

Figure 2.16. Plotting of an artificial image and its mask as a result of augmentation

2.4.4. Implementation and training of the model (U-Net)

The deep learning model used for the segmentation of mitochondria had a U-Net architecture. U-Net is a special type of convolutional neural network designed for image segmentation. It features a symmetrical encoder-decoder structure with a series of convolutional layers. The encoder (or contracting path) progressively reduces the spatial dimensions of the input image, while increasing its depth, extracting high-level features. The decoder (or expansive path) then reconstructs the image to its original dimensions by up sampling and combining these features with corresponding high-resolution features from the encoder via skip connections. This combination helps preserve spatial details and enhances the accuracy of the segmentation. Due to the shape of its architecture (with the encoder and decoder paths), it resembles the shape of ‘U’ (*see also figure 2.17*) [37].

An implementation of the U-Net architecture exists in the *segmentation models* library and can be downloaded from there. Upon defining it, the backbone network was put as argument, trained in the *ImageNet* dataset, a large-scale image database used for training and evaluating machine learning models.

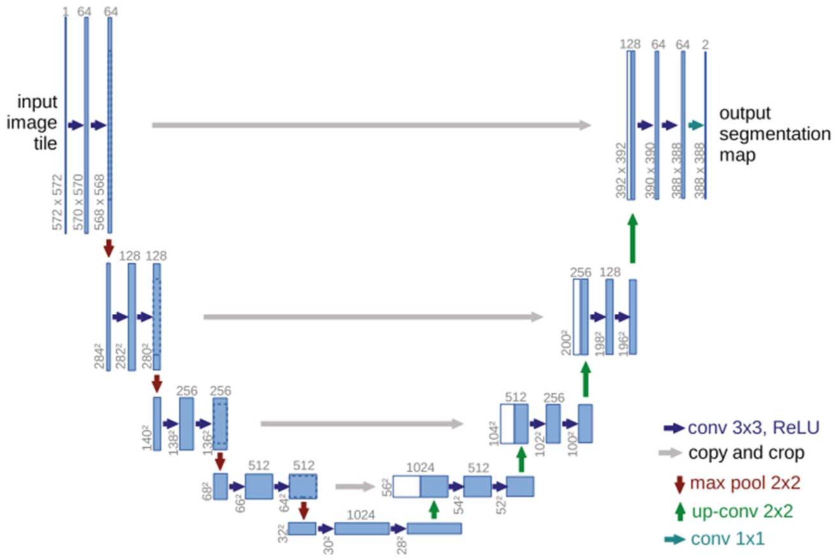

Figure 2.17. Representation of the U-Net model architecture [38].

The model was compiled with *Adam* optimization. Adam is an adaptive optimizer that manipulates the learning rate of the model during training. For the loss function, a combination of binary cross-entropy (BCE) and the Jaccard index was used [36]. Loss function is the hyperparameter of the model suitable for balancing pixel-wise classification and overlapping measures. For the evaluation of training, the metric used was Intersection over Union (IoU) which measures the overlap between predicted and ground truth masks. After compilation, the model was fitted on the training data. For the training and validation, the two data generators from the previous steps were used. The U-Net model was trained for fifty epochs (iterations over the entire training dataset), with fifty batches of images for training and validation per epoch (*see below Figure 2.18*).

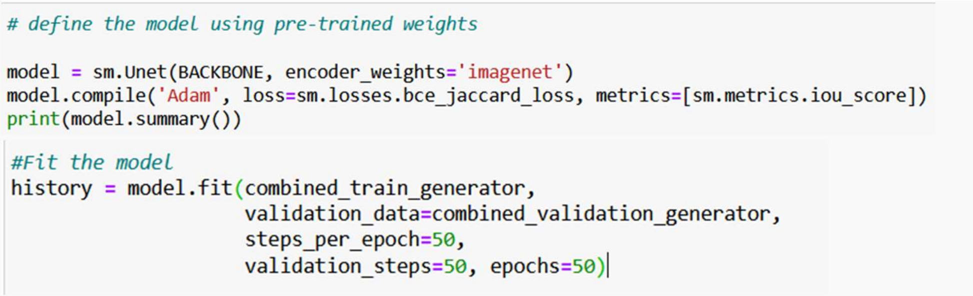

```
# define the model using pre-trained weights

model = sm.Unet(BACKBONE, encoder_weights='imagenet')
model.compile('Adam', loss=sm.losses.bce_jaccard_loss, metrics=[sm.metrics.iou_score])
print(model.summary())
```

```
#Fit the model
history = model.fit(combined_train_generator,
                    validation_data=combined_validation_generator,
                    steps_per_epoch=50,
                    validation_steps=50, epochs=50)
```

Figure 2.18. Model loading, compilation and training for 50 epochs.

Except of this model with the pre-trained weights, two more trainings were performed on a simple U-Net without a residual network, one with data augmentation and one without. In this way, the contribution both of the backbone and of the data augmentation could be made clear.

2.4.5. Model evaluation

For better visualization of the training procedure, the training and validation accuracy and loss curves were plotted by measuring them at each epoch. The code used for these tasks is shown in Figures 2.19 and 2.20.

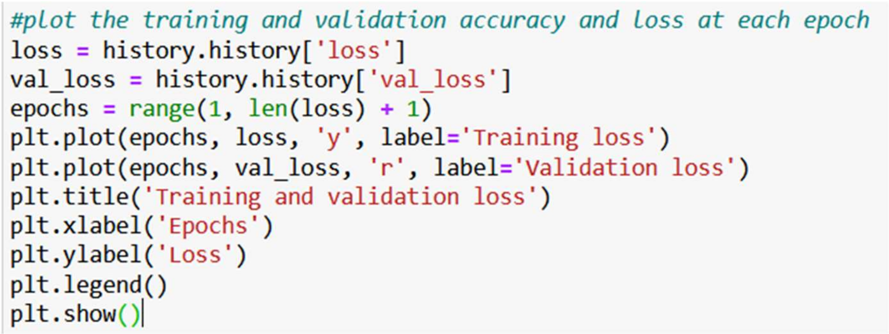

```
#plot the training and validation accuracy and loss at each epoch
loss = history.history['loss']
val_loss = history.history['val_loss']
epochs = range(1, len(loss) + 1)
plt.plot(epochs, loss, 'y', label='Training loss')
plt.plot(epochs, val_loss, 'r', label='Validation loss')
plt.title('Training and validation loss')
plt.xlabel('Epochs')
plt.ylabel('Loss')
plt.legend()
plt.show()
```

Figure 2.19. Code for plotting the training and validation loss curve

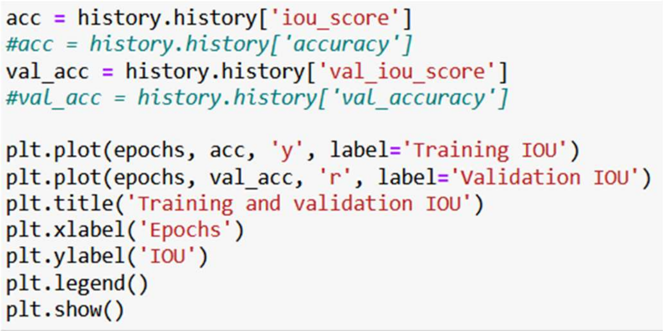

```
acc = history.history['iou_score']
#acc = history.history['accuracy']
val_acc = history.history['val_iou_score']
#val_acc = history.history['val_accuracy']

plt.plot(epochs, acc, 'y', label='Training IOU')
plt.plot(epochs, val_acc, 'r', label='Validation IOU')
plt.title('Training and validation IOU')
plt.xlabel('Epochs')
plt.ylabel('IOU')
plt.legend()
plt.show()
```

Figure 2.20. Plotting the training and validation accuracy via the IoU value.

For image segmentation tasks, traditional accuracy is not a good metric. That is because it might be overestimated due to the prevailing background class of the masks (the black pixels is the background class, in contrast with the white mitochondria). Therefore, the metric of Intersection over Union is used for evaluation. This metric measures the intersection of covered areas between the two classes and divides it by their union. In our code, IoU was implemented as shown in figure 2.21. A threshold of 0.5 was used to binarize the output predictions [36].

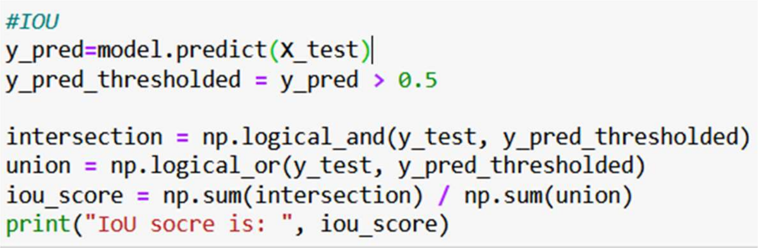

```
#IOU
y_pred=model.predict(X_test)
y_pred_thresholded = y_pred > 0.5

intersection = np.logical_and(y_test, y_pred_thresholded)
union = np.logical_or(y_test, y_pred_thresholded)
iou_score = np.sum(intersection) / np.sum(union)
print("IoU socre is: ", iou_score)
```

Figure 2.21. Intersection over Union on the predictions of the model.

Finally, a code for visualizing the results was added. The code shown in figure 2.22 takes a random image from the X_test dataset and plots it alongside its ground truth label (its true mask) and the prediction made by the model. The predicted label is binarized with a threshold which can be adjusted, based on the effectiveness of the model.

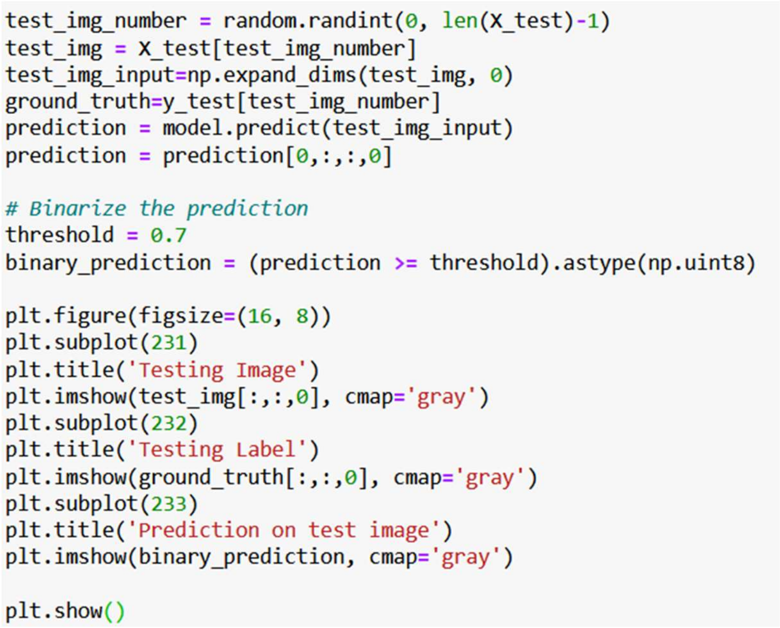

```
test_img_number = random.randint(0, len(X_test)-1)
test_img = X_test[test_img_number]
test_img_input=np.expand_dims(test_img, 0)
ground_truth=y_test[test_img_number]
prediction = model.predict(test_img_input)
prediction = prediction[0,:,:,0]

# Binarize the prediction
threshold = 0.7
binary_prediction = (prediction >= threshold).astype(np.uint8)

plt.figure(figsize=(16, 8))
plt.subplot(231)
plt.title('Testing Image')
plt.imshow(test_img[:,:,0], cmap='gray')
plt.subplot(232)
plt.title('Testing Label')
plt.imshow(ground_truth[:,:,0], cmap='gray')
plt.subplot(233)
plt.title('Prediction on test image')
plt.imshow(binary_prediction, cmap='gray')

plt.show()
```

Figure 2.22. Code for plotting the test image, its ground truth label and predicted label

Chapter 3: Results and Discussion

3.1. Statistics from the morphometric analysis

3.1.1. Percentage of mitochondria per μm^2

Conventional dose rate

From the analysis of the electron micrographs of the small intestinal tissue, the percentage of normal and damaged mitochondria per squared micrometer was plotted, at thirty minutes, four hours and eighteen hours after exposure (*Figure 3.1*). For comparison, the percentages of the non-irradiated control group are presented on the same graph.

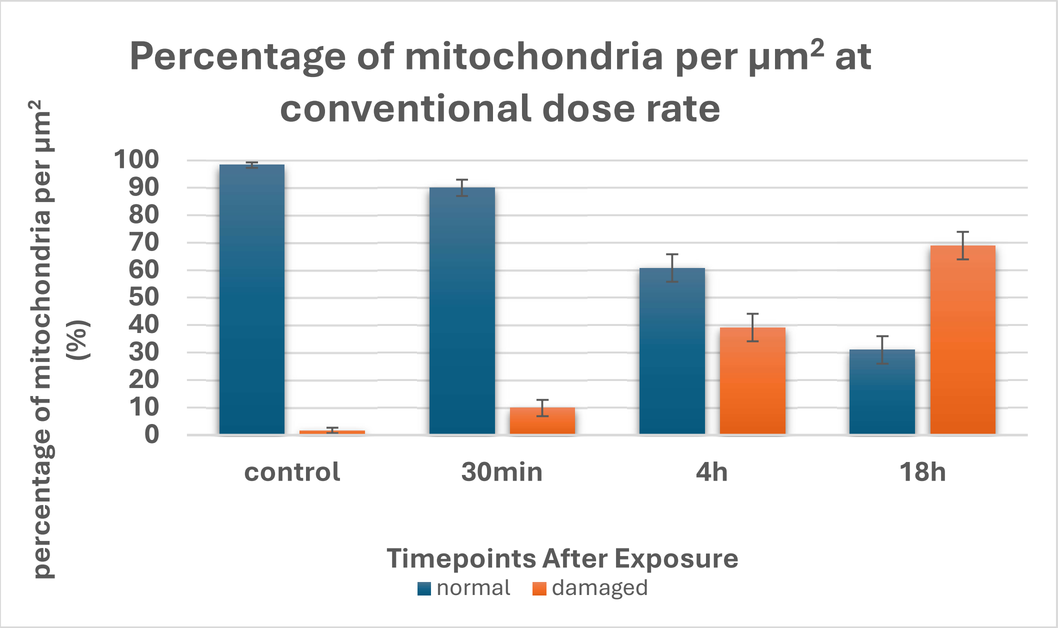

Figure 3.1. Percentage of normal and damaged mitochondria per μm^2 for the control group and the three timepoints after exposure at conventional dose rate.

The analytical values of all the measurements for the graphs can be found on Appendix 1. In figure 3.2, representative electron micrographs are presented, for the control group as well as for each timepoint after exposure with conventional dose rate protons.

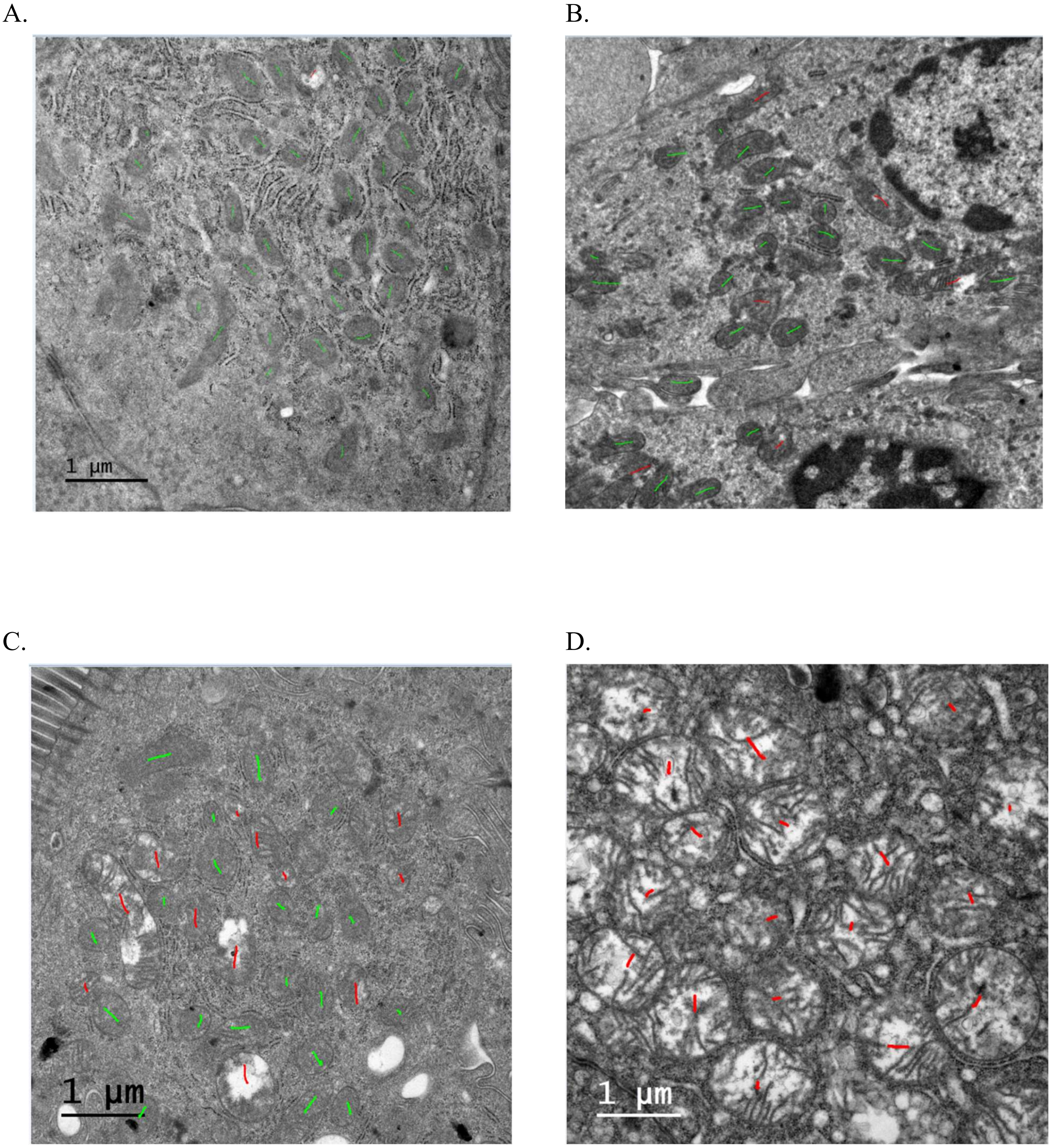

Figure 3.2. Representative electron micrographs for each experimental condition. (A) Control group, (B) 30 minutes after exposure to conventional dose rate proton radiation, (C) 4 hours after exposure to conventional dose rate proton radiation and (D) 18 hours after exposure to conventional dose rate proton radiation.

FLASH

The equivalent graph was plotted for the FLASH dose rate and is shown in Figure 3.3. In Figure 3.4, some representative electron micrographs are presented, from the control group as well as for each of the three timepoints after exposure to FLASH radiation.

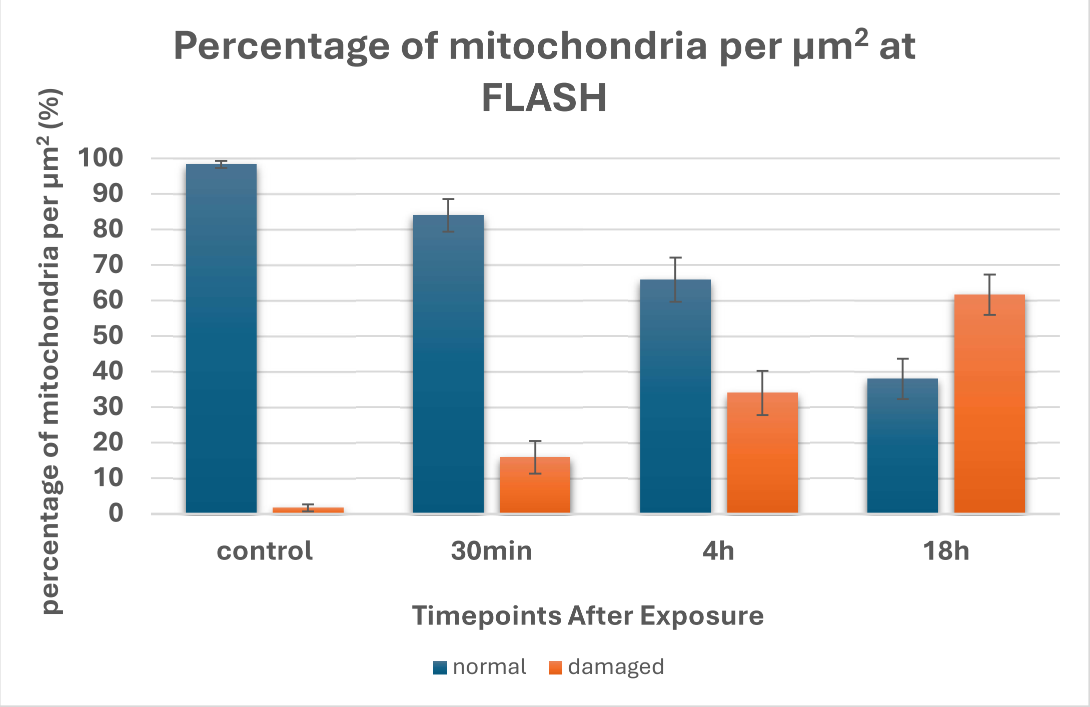

Figure 3.3. Percentage of normal and damaged mitochondria per m² for the control group and the three timepoints after exposure to FLASH proton radiation.

Comparison of conventional and FLASH 30 minutes post-exposure

In order to get a better understanding of the results, the condition from graphs 3.1 and 3.3 that corresponds to the 30-minute post-exposure timepoint was re-plotted in Figure 3.5.

From a quick look on this diagram, one could deduce that there is no significant difference in the percentage of damaged mitochondria between the samples irradiated with conventional dose rate and FLASH radiation. In both cases, normal mitochondria greatly outnumber the damaged ones, but the percentages seem equivalent for the two radiation dose rates. To test whether the difference between them was statistically significant we performed a t-test [39], with parameters the average percentage of damaged mitochondria, its standard error and the number of samples (images) for each dose rate.

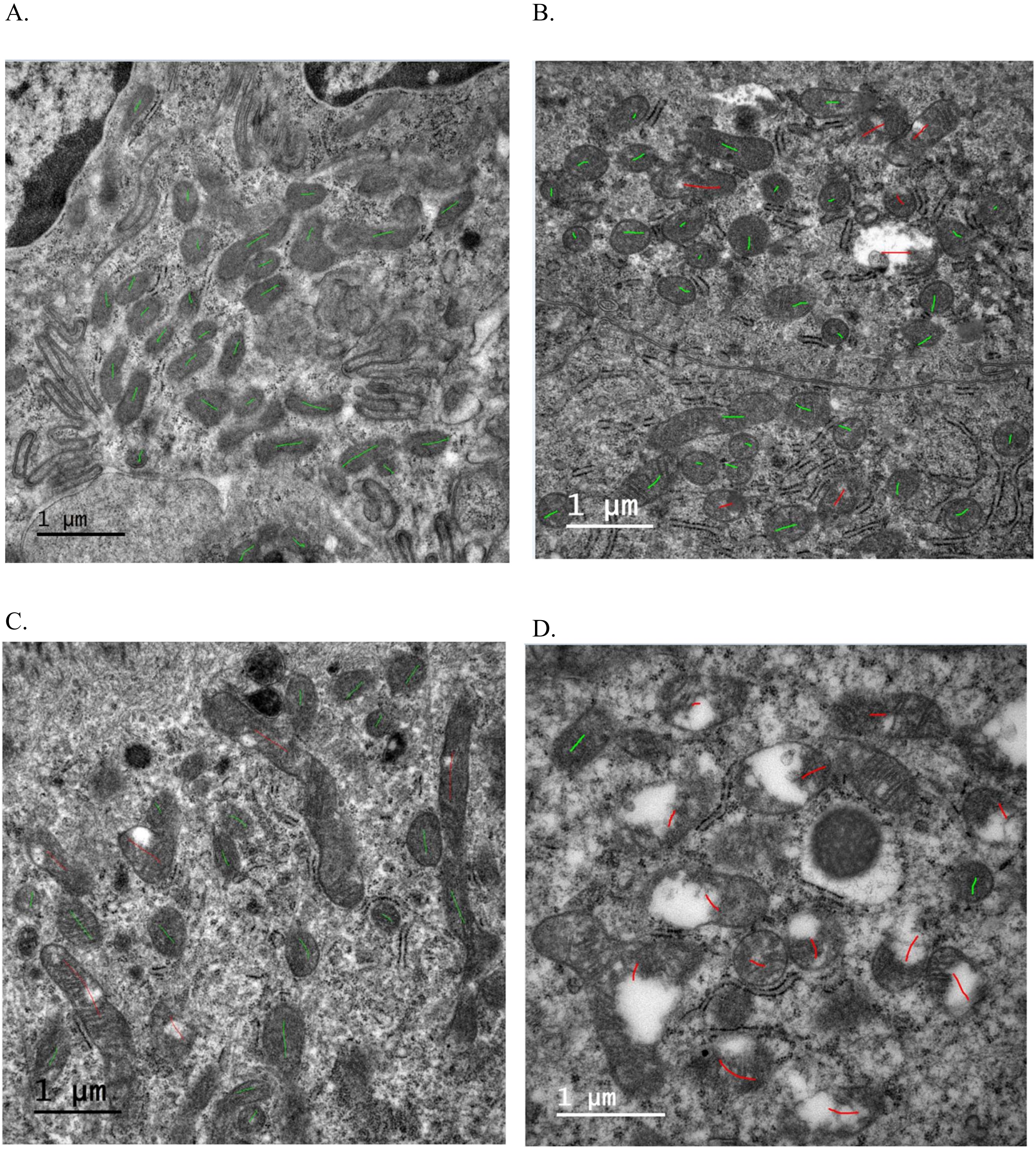

Figure 3.4. Representative electron micrographs for each experimental condition. (A) Control group, (B) 30 minutes after exposure to FLASH proton radiation, (C) 4 hours after exposure to FLASH proton radiation and (D) 18 hours after exposure to FLASH proton radiation.

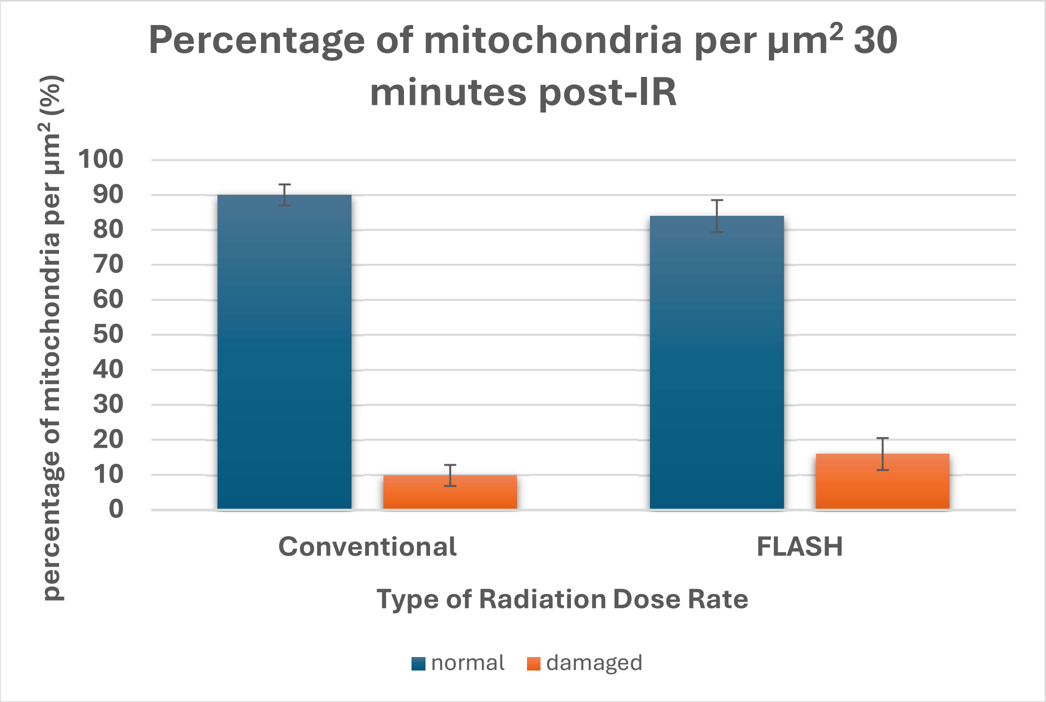

Figure 3.5. Comparison of normal and damaged mitochondria between conventional dose rate and FLASH 30 minutes after exposure.

The resulting p-value showed **no** statistically significant difference between the percentages.

Comparison of conventional and FLASH 4 hours post-exposure

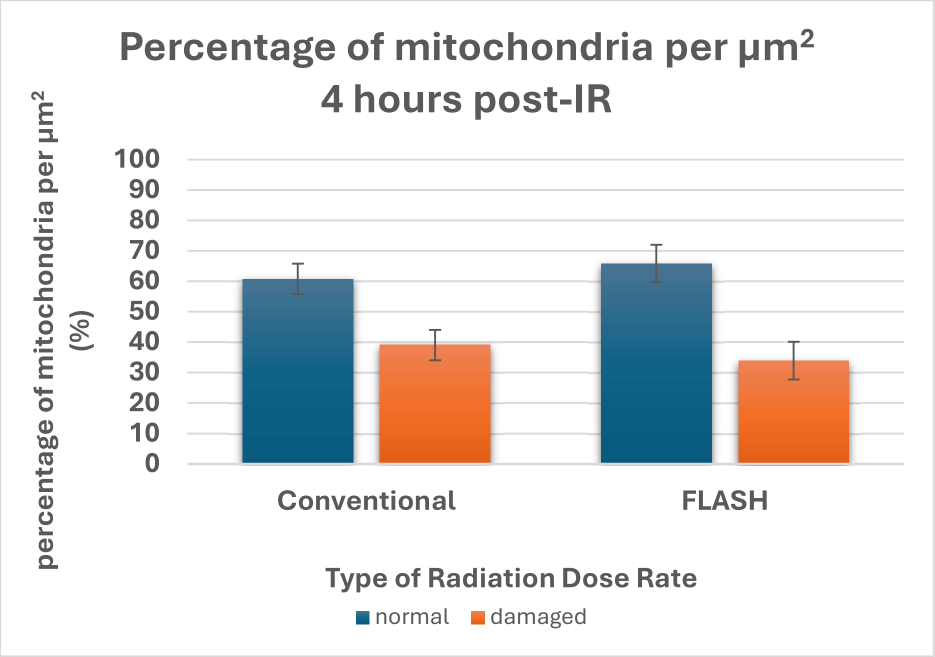

Figure 3.6. Comparison of normal and damaged mitochondria between conventional dose rate and FLASH 4 hours after exposure.

In figure 3.6 the percentages of normal and damaged mitochondria for the two dose rates are compared, four hours after the exposure. The percentages of normal mitochondria are still higher than these of the damaged ones, but their difference has significantly decreased compared to the thirty-minute timepoint.

Although it might seem that the percentage of damaged mitochondria at FLASH is slightly lower than that at conventional dose rate, the t-test [39] showed no statistically significant difference between the two.

Comparison of conventional and FLASH 18 hours post-exposure

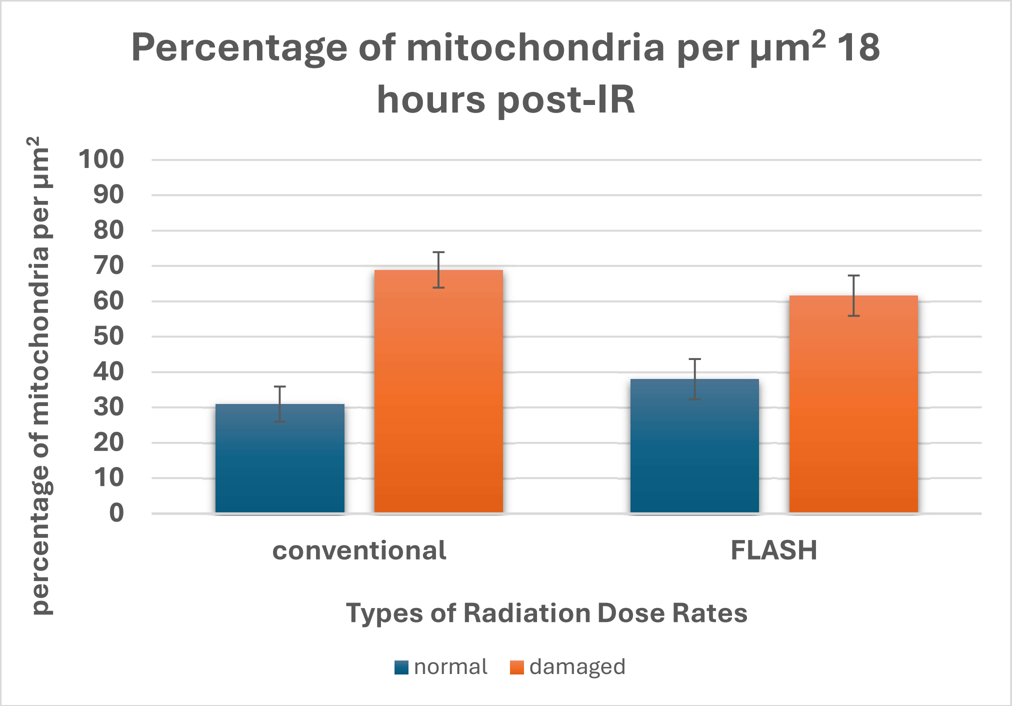

Figure 3.7. Comparison of normal and damaged mitochondria between conventional dose rate and FLASH 18 hours after exposure.

As shown in Figure 3.7, eighteen hours after exposure, the damaged mitochondria outnumber the normal ones for both radiation dose rates.

Whether the percentages differ significantly between the two rates is again a hypothesis to be tested. Neither in this case, however, the results were encouraging. The t-test [39] showed no statistically significant difference for the percentages of damaged mitochondria between the two dose rates.

General Overview

The above results indicate that mitochondrial response in conventional and ultra-high dose rate irradiation (FLASH) does not present any significant differences at any timepoint up to eighteen hours post-IR. In both cases, the percentage of damaged mitochondria is continuously increasing, reaching sixty to seventy percent at eighteen hours after exposure. This result is in contrast to a recent study investigating the effects of proton radiation on mitochondria in normal human lung fibroblasts [40]. According to this study, FLASH irradiation (100 Gy/s) showcased increased survival and minimal mitochondrial damage, compared to conventional dose rate irradiation (0.33 Gy/s). The total dose delivered was 15 Gy at ambient oxygen concentration (21%), the exact same conditions as in our experiment. Furthermore, another study in mouse embryonic fibroblast cells, showed decreased apoptosis and necrosis for FLASH radiation (29% decrease), relative to conventional dose rate radiation (14.25% decrease) [41]. Considering the relationship between damaged mitochondria and induced cell death [42], decreased levels of apoptosis are linked to lower damage of the mitochondrial outer membrane (and subsequently less morphological alterations). These findings have led scientists to believe that mitochondrial sparing at FLASH irradiation could be a possible explanation for the mechanism behind FLASH effect [42].

The fact that our observations are not in accordance with the above findings may be due to several reasons. It is generally accepted that the protective effects of FLASH are not uniform across all types of cells and tissues [41], so a more extended investigation of ultra-high dose rate radiation on the small intestinal epithelium is needed. In addition, while there are indications suggesting that FLASH effect is still present in normoxic environments [42], general consensus claims that it is more prominent in hypoxic environments [9, 13]. Since our experiment was performed in ambient oxygen, the expected FLASH effect could have been masked. Differences in the timing of the assessment between the present and the aforementioned studies could have also played a role in determining the outcome. More specifically, it is possible that the timepoint of eighteen hours post-IR has been quite early for the final assessment, and the differences between conventional and FLASH could have been more obvious in a later timepoint. Furthermore, the method followed in the present thesis for evaluating normal and damaged mitochondria was exclusively morphometrical, while other studies considered genetic, chemical and electrophysiological factors to determine whether a mitochondrion could be considered damaged or not [42]. Finally, TEM microscopy, although a very powerful technique for qualitative research, it bears limitations in quantifying these findings. As a result, further studies need to take place for the evaluation of the percentage of normal and damaged mitochondria in FLASH and conventional dose rate, with more experimental variables and additional, more quantitative techniques along with TEM microscopy.

3.1.2. Average area of mitochondria

Conventional dose rate

Using the image analysis software (ImageJ), the average area per mitochondrion was measured for normal and damaged mitochondria, for all the electron micrographs of the control conditions and of the different timepoints after exposure to conventional rate radiation. Following this, the combined average of the two groups of our data was calculated for each condition. The results are shown in Figure 3.8. The errors were assumed to be the standard statistical errors. For an analytical representation of the calculated values of averages and errors, see table 2 on Appendix 1.

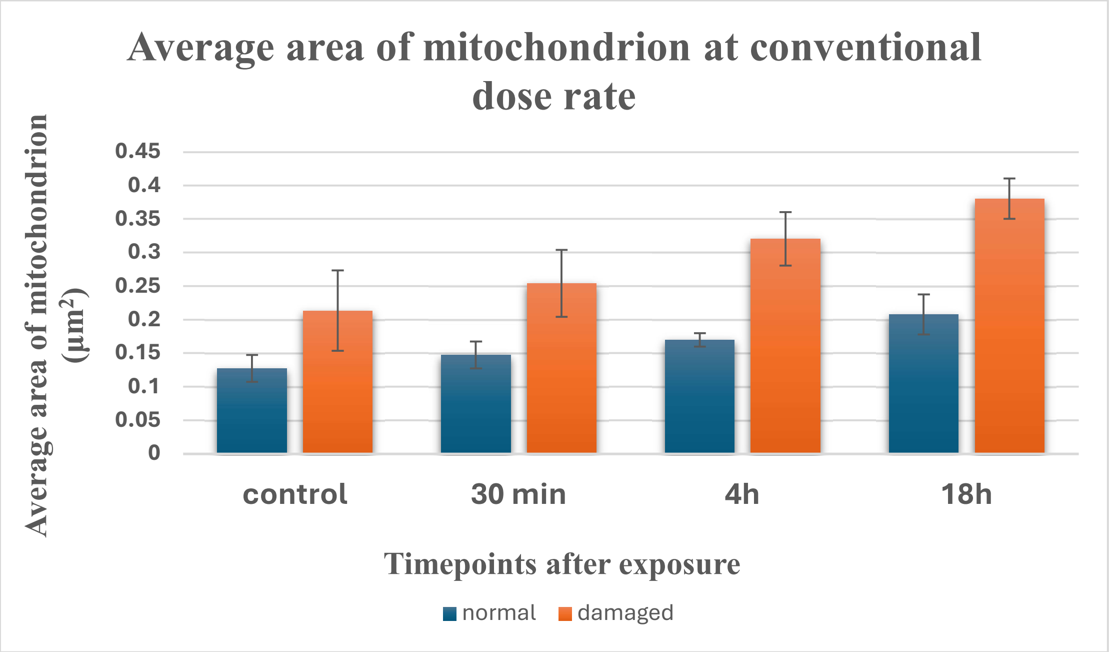

Figure 3.8. Average area of normal and damaged mitochondria for the control group and the three timepoints after exposure to conventional dose rate radiation.

FLASH

The equivalent graph for FLASH radiation was plotted below, in Figure 3.9.

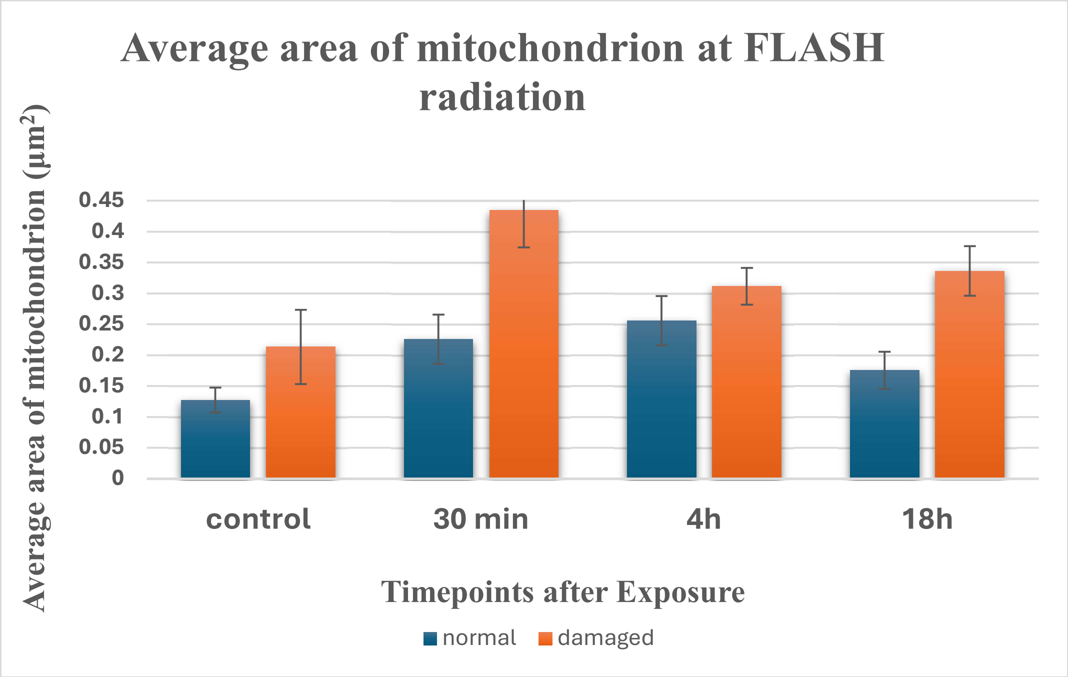

Figure 3.9. Average area of normal and damaged mitochondria for the control group and the three timepoints after exposure to FLASH radiation.

From the two figures 3.8 and 3.9, it seems that, while exposure to conventional radiation leads to a progressively increasing area for both normal and damaged mitochondria, with the timepoint at 18 hours showing the greatest 'swelling', this is not the case for FLASH. According to Figure 3.9, after exposure to FLASH radiation, mitochondria tend to augment their size quickly, reaching a maximum value for the area within thirty minutes and then decreasing once more. The comparison of conventional dose rate and FLASH for each of the post-exposure timepoints is done in the following sections.

Comparison of conventional and FLASH 30 minutes post-exposure

In Figure 3.10, the average areas of mitochondria for conventional dose rate and FLASH radiation are compared. Both normal and damaged mitochondria seem to experience a greater area increase in FLASH radiation. The difference between the area of normal and damaged however, appears to have increased too. For conventional dose rate, the average area of damaged mitochondria is 0.254 μm^2, 72% larger than that of the normal (0.147 μm^2), while for FLASH the damaged occupy approximately 92% more area than normal ones (0.435 μm^2 for damaged compared to 0.226 for normal).

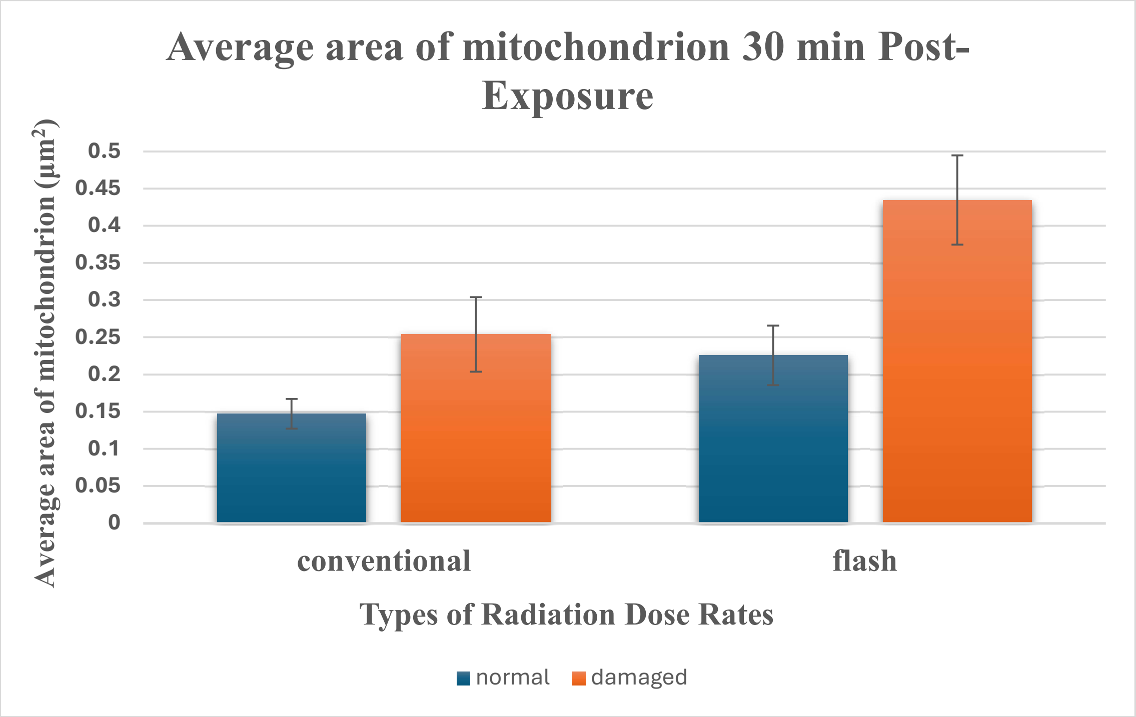

Figure 3.10. Comparison of normal and damaged mitochondria areas between conventional dose rate and FLASH 30 minutes after exposure.

Knowing the average values for the area, their standard errors and the number of elements of the samples, a t-test [39] was performed to determine whether the average areas of damaged mitochondria differ significantly between the conventional dose rate and FLASH radiation. This gave a p-value of 0.043 so there is a significant difference between the areas of the damaged mitochondria.

We are also interested in the relative differences between the areas of normal and damaged mitochondria for each type of dose rate. In order to determine whether this difference is statistically significant, we performed a t-test with the null hypothesis,

$$\bar{A}_{n,conv} - \bar{A}_{d,conv} = \bar{A}_{n,FLASH} - \bar{A}_{d,FLASH} \qquad (3.5)$$

Where $\bar{A}_{i,j}$ is the average area of mitochondria for j type of radiation dose rate and i= {normal, damaged}. The differences of the two sides of equation (3.5) were calculated as $D_{conv} = \bar{A}_{n,conv} - \bar{A}_{d,conv} = 0.1067$ and $D_{FLASH} = \bar{A}_{n,FLASH} - \bar{A}_{d,FLASH} = 0.2087$.

The standard statistical errors of these differences were found to be equal to $SE_{conv} = 0.027$ and $SE_{FLASH} = 0.04$, so the combined error was $SE_{total} = 0.048$. These values gave a t-test score of

$$t_{value} = \frac{D_{FLASH} - D_{conv}}{SE_{total}} = 2.125.$$

Combining with the degrees of freedom for this case ($f = n_1 + n_2 - 2 = 126$), we got a p-value of 0.036 [43].

As a result, the differences are statistically significant and the damaged mitochondria indeed appear more enlarged in relation to the normal ones in FLASH, compared to conventional dose rate.

Comparison of conventional and FLASH 4 hours post-exposure

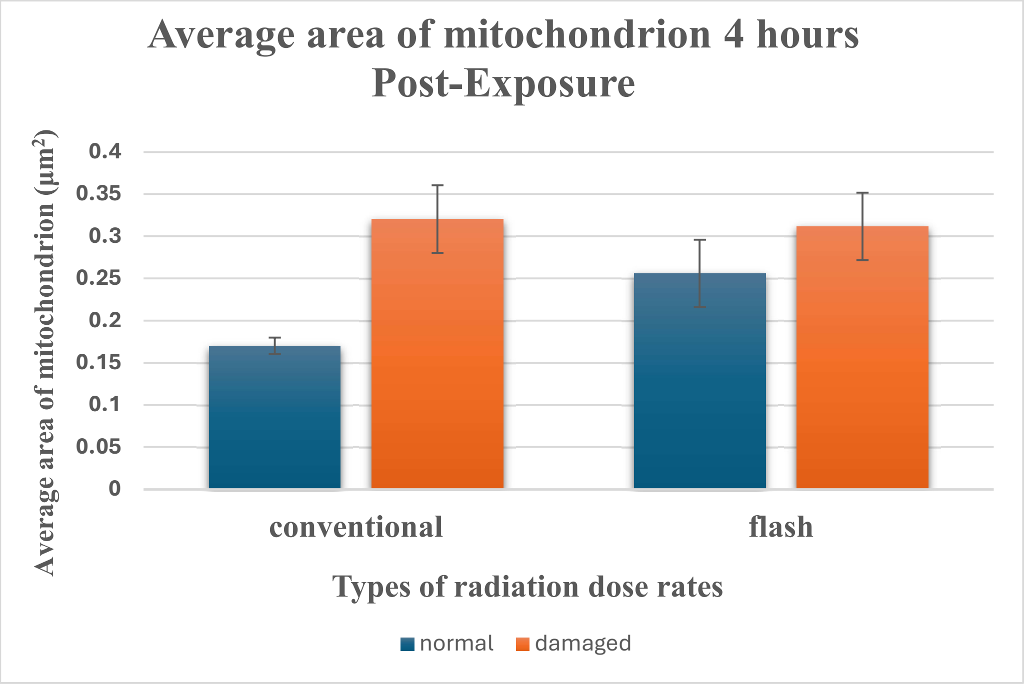

Figure 3.11. Comparison of normal and damaged mitochondria areas between conventional dose rate and FLASH 4 hours after exposure.

Figure 3.11 shows the average areas of mitochondria for the two dose rates 4 hours after exposure. The percentages of damaged mitochondria seem comparable, while the normal ones appear to have a larger average area in FLASH than in conventional dose rate. More specifically, the relative difference between the areas of normal and damaged mitochondria reach 88% for conventional dose rate and 21% for FLASH.

Using the t-test [39] on the average areas of the normal mitochondria, a p-value of 0.035 was acquired, meaning that the areas of normal mitochondria differ significantly between FLASH and conventional dose rate radiation.

In addition, as in the condition of 30 minutes post-IR, a second t-test was performed to compare the relative differences of normal and damaged mitochondria between FLASH and conventional dose rate. With parameter values as: ($D_{conv} = 0.15, D_{FLASH} = 0.056,\ SE_{total} = 0.033,\ t_{value} = 2.8,\ f = 164$), a p-value of 0.0057 was found [43], meaning a 0.57% probability for the null hypothesis. As a result, it is safe to reject it and assume that the relative area between normal and damaged mitochondria differs significantly in FLASH and conventional rate radiation.

Comparison of conventional and FLASH 18 hours post-exposure

Eighteen hours after the exposure, the average area of mitochondria was as shown in Figure 3.12. Both normal and damaged mitochondria appeared to have slightly smaller area when exposed to FLASH compared to conventional dose rate.

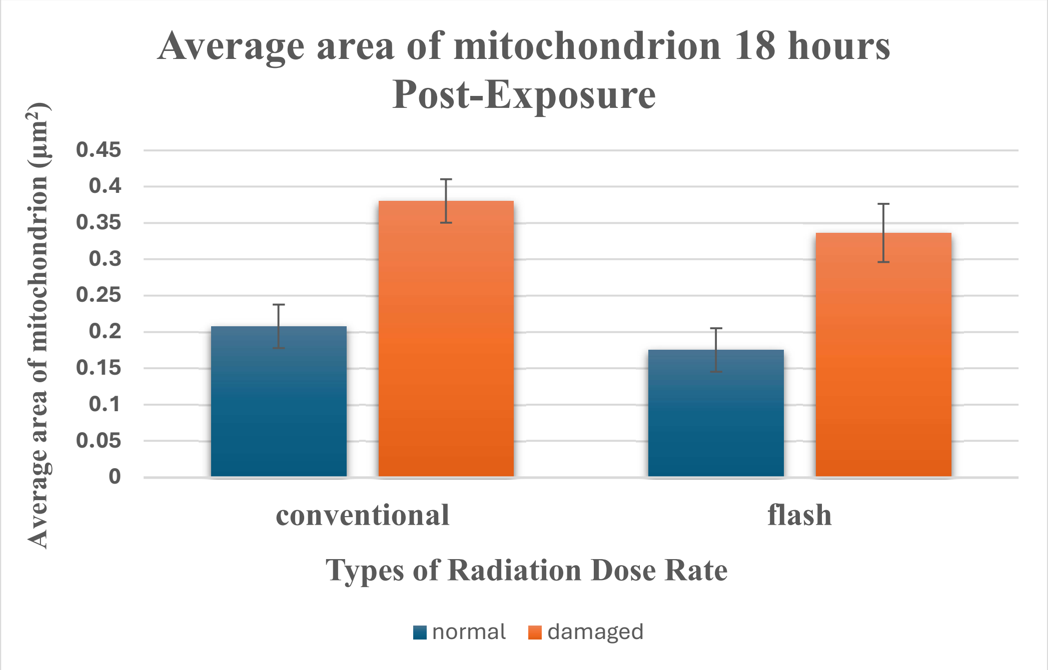

Figure 3.12. Comparison of normal and damaged mitochondria areas between conventional dose rate and FLASH 18 hours after exposure.

The relative area difference between damaged and normal mitochondria is 81% for conventional dose rate and 92% for FLASH.

In this case, comparing the average areas of damaged mitochondria of conventional dose rare versus FLASH, the t-test [39] showed no statistically significant difference between the two.

Furthermore, the t-test performed on the relative differences of normal and damaged mitochondria between FLASH and conventional dose rate (with parameters values of $D_{conv} = 0.173,\ D_{FLASH} = 0.161,\ SE_{total} = 0.03,\ t_{value} = 0.4,\ f = 235$), gave $p\text{-}value$ = 0.345 [43]. This p-value corresponds to a 68.95% probability for the differences in areas to be statistically the same. Thus, an assumption cannot be made in favor of one of the two radiation rates 18 hours after exposure.

General overview

In general, the experiment indicates a post-IR increase in the area of mitochondria for both conventional dose rate and FLASH. This is in accordance with older studies [20, 44] which refer to branching, elongation and size increase of irradiated mitochondria. As shown in figures 3.8 and 3.9, while area seems to increase with post-IR time until eighteen hours for conventional dose rate, FLASH-irradiated mitochondria take a maximum area value thirty minutes post-IR and then start to decrease in size. Although there aren't many studies investigating the specific effects of FLASH proton radiation on the size of mitochondria, it is generally accepted that post-IR increase in mitochondrial size is reversible [20, 44, 45]. As a consequence, it might be the case that the maximum area value for the conventionally irradiated mitochondria would be reached in a timepoint after eighteen hours, not observed in the present study, and then a decrease would follow, similar to that observed in FLASH. This would indicate that the post-IR effects of FLASH concerning the size of mitochondria are far more short-lived than the equivalent for the conventional dose rate, despite being qualitatively similar.

Furthermore, the experiment indicates that the increase in mitochondrial area is present in both normal and damaged mitochondria, though not on the same extent. More specifically, damaged mitochondria appear generally larger than normal ones, something that can be attributed, among others, to the vacuolization and disruption of their membrane [20]. However, normal mitochondria show an increase in their size as well, reaching a maximum value of 0.207 μm^2 at 18 hours post-IR for conventional dose rate and of 0.256 μm^2 at 4 hours post-IR for FLASH. The increase in the area of the normal mitochondria should not be surprising, since, though not severely damaged, they have undergone exposure to ionizing radiation as well.

Finally, the relative difference between the areas of normal and damaged mitochondria showcase dissimilarity in FLASH and conventional dose rates. More specifically, at thirty minutes post-IR the difference in areas was greater for FLASH irradiated cells, at four hours post-IR it was greater for conventionally irradiated cells (as a greater enlargement was observed for the FLASH-irradiated normal mitochondria), while at eighteen hours post-IR there was no statistically significant difference between them. In order to get a more global understanding of the underlying phenomena though, for the reasons discussed above, further studies are encouraged to shed light on more long-term effects of FLASH proton radiation at later timepoints.

3.2. Segmentation model results

Loss and IoU graphs

The model was trained for fifty epochs. From the data acquired during training, the loss was plotted for both the training and validation processes (see Figure 3.). Furthermore, the Intersection over Union metric value was calculated and plotted for training and validation during the fifty epochs. The resulting graph is shown below in Figure 3.13.

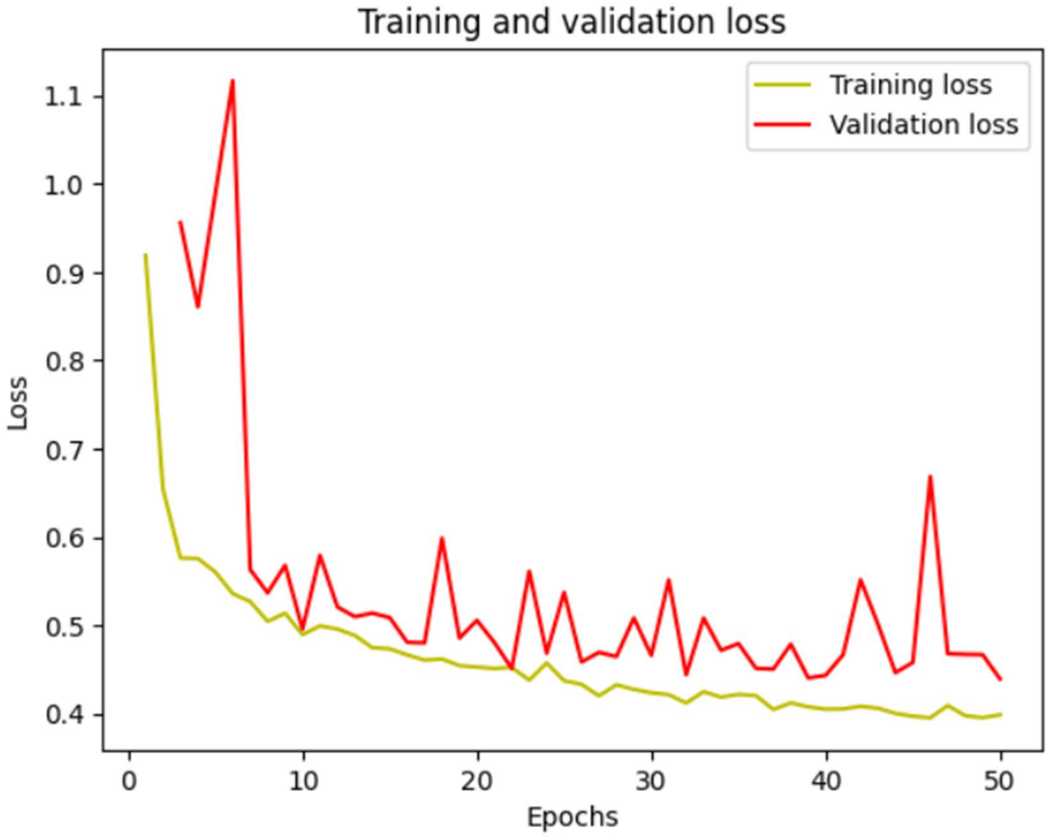

Figure 3.13. Training and validation loss over the 50 epochs

Loss is a measure of how well the model's predictions match the actual target values. In general, loss is expected to decrease over the progression of iterations. This is an indication that the model is learning useful features and adapts better in the input training data. As seen in Figure 3.13, training loss follows a quite smooth decrease from 0.981 at the first epoch, to 0.398 at the final epoch. As far as loss is concerned, its increasing or decreasing nature is more important than its absolute value, which heavily depends on the choice of the loss function used (here, Binary Cross Entropy with Jaccard loss).

Figure 3.14 shows that validation loss, although descending as well, appears to fluctuate more than the training loss, having ‘spikes’ at larger values. This behavior is expected as the training loss is used for directly optimizing the model on the training data. The weights of the network are constantly updating, therefore leading to a smoother curve for the loss. In contrast, validation loss is derived from the testing of the model on new images, unseen during training. As a result, the loss fluctuates more, but its descending nature is an indication that the model is successful with unknown data as well.

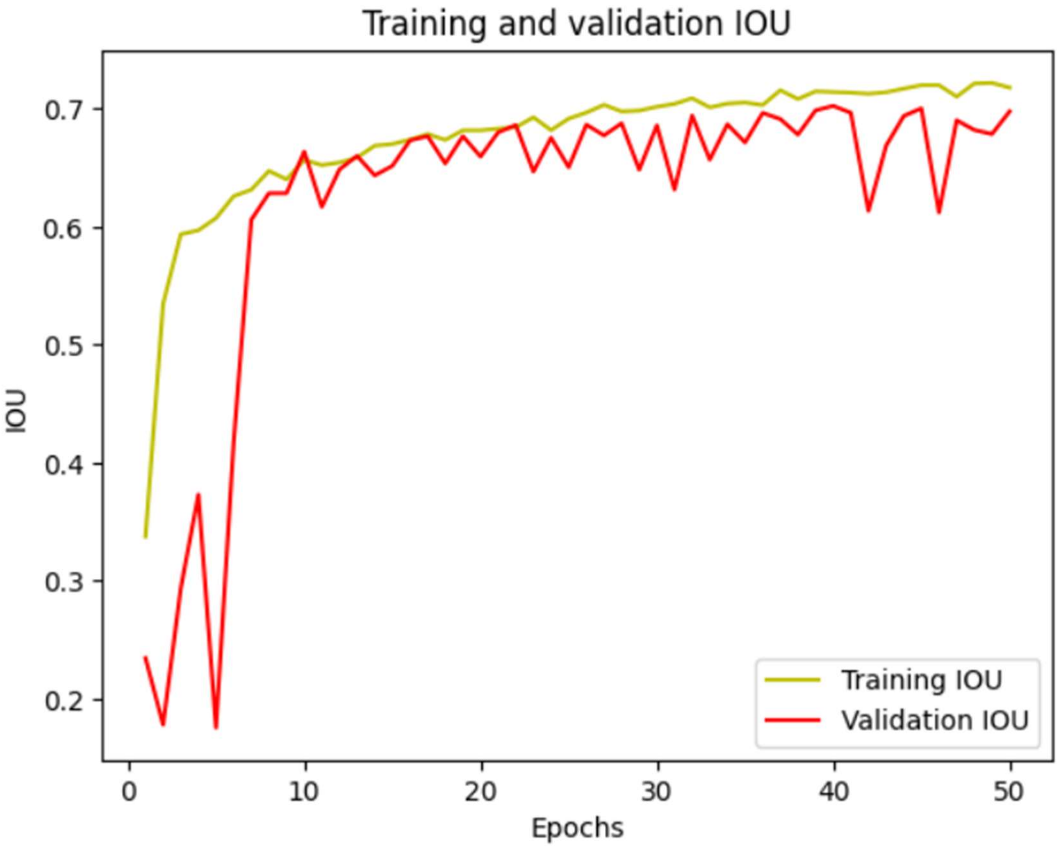

Figure 3.14. Training and validation IoU value over the 50 epochs.

Intersection over Union (IoU) calculates the ratio of the intersection area between the predicted mask and the ground truth label over their union area. It is then obvious that IoU takes values in the range [0,1], with 1 being the perfect match. As it is a measure of the accuracy of the model, it is expected to increase with the number of iterations. This is indeed the case, as indicated in Figure 3.14. Again, the training curve appears to be smoother than the validation one and this can be attributed to the different datasets that are used as reference. Training IoU starts at a value of 0.337 at epoch one and reaches 0.717 by epoch fifty, while validation IoU starts at 0.234 and reaches 0.697.

<u>Comparison of IoU for different training approaches</u>

As mentioned in the Methodology section, the model was run with three separate training approaches. In the first approach, data augmentation was removed and the model used was a simple U-Net without backbone amplification. In the second approach, data augmentation was used on this simple model, while on the third and final approach, both data augmentation and a *resnet34* backbone to the model were added.

Using a threshold of 0.5, IoU was calculated for all three cases. By thresholding the output, we ensured that the prediction masks would contain only binary values for the pixels and not a continuous spectrum of probabilities. In this way, IoU value is more relatable because a binary mask is expected as a final output as well. The measurements resulted in:

- $IoU = 0.32$ for the simple U-Net model without data augmentation
- $IoU = 0.45$ for the simple U-Net model using data augmentation
- $IoU = 0.73$ for the U-Net model with resnet34 backbone, using data augmentation

From the above results, the importance of both data augmentation and the backbone network was made obvious. More specifically, the simple model showed an IoU increase of 40% when data augmentation was used. When the backbone network was added, the increase in IoU reached 128% from the original approach and 62% from the second approach. As a result, it is fairly safe to assume that the combination of data augmentation and pre-trained network training showcases the best performance between the three.

The achieved IoU of the last approach, although very improved in relation to the other too, is not quite as high as the one achieved by the state-of-the-art models used for similar tasks, which may reach an IoU value of 0.8-0.9 [46, 47]. The reason for this could be lying on the nature of the dataset used. Except from being significantly smaller than the one used in recent studies [47], it presented much higher diversity in its instances. The images were at various focusing scales and were originating from different parts of the small intestine. In addition, the samples contained both healthy and damaged mitochondria due to radiation, something that has a visible effect on their phenotype. As a result, the combination of these factors incommoded the recognition of the mitochondrial shapes by the model. Finally, the human error factor is not to be ignored, as the entire original annotation of the shapes had been done manually.

Visualization of the results

In order to better understand the results, a random sample from the three training approaches was visualized and can be seen in the following figures 3.15 -3.17.

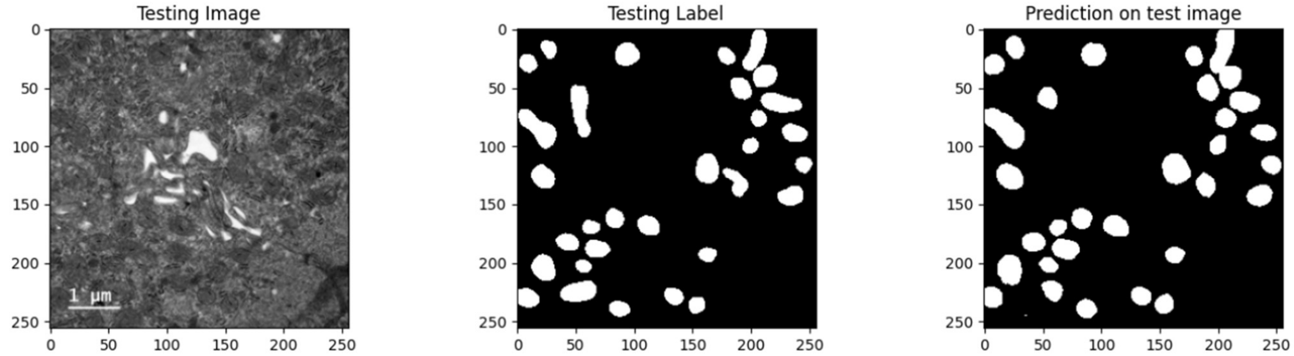

Figure 3.15. Random testing image (left), alongside its ground truth label (middle) and predicted mask (right) for the final approach. (U-Net with backbone network and data augmentation).

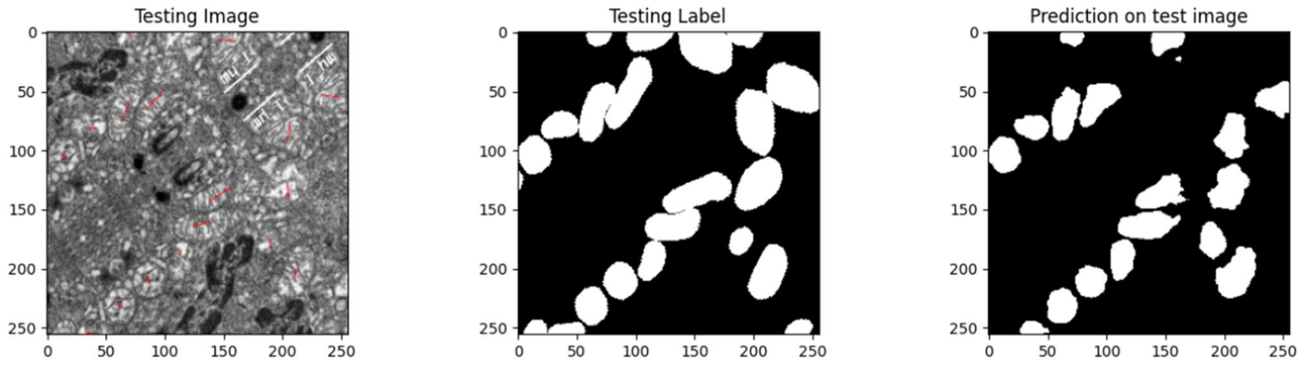

Figure 3.16. Random image, true label and predicted mask for the simple U-Net model with the use of data augmentation.

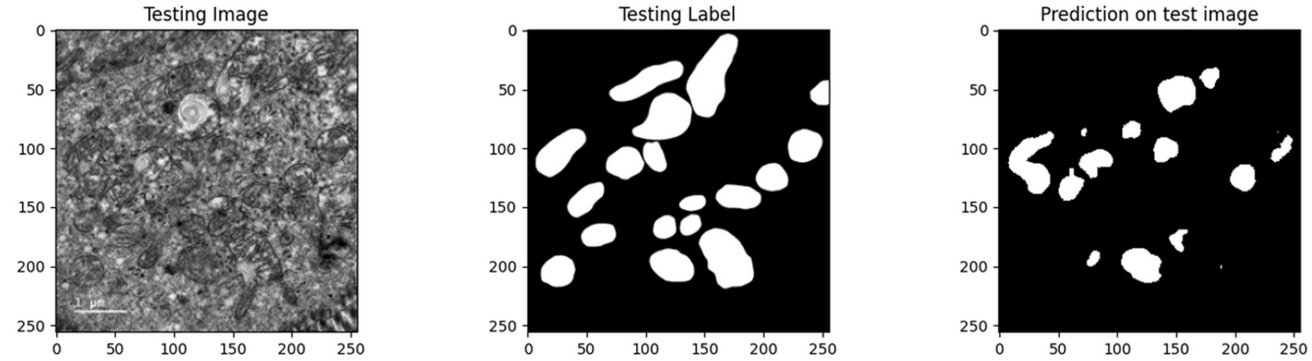

Figure 3.17. Random image, true label and predicted mask for the simple U-Net model without data augmentation.

As we can see, the final model can distinguish the shapes of mitochondria with great success and it only fails to outline some edges, or some ambiguous shapes that would have possibly challenged a human annotator as well. On the other hand, in the original approach of the simple U-Net without augmentation, shapes are barely recognizable, with a lot of information missing. The shapes of some well-outlined mitochondria can still be distinguished but the majority of them are either extracted incompletely, or not extracted at all. Somewhere in the middle of the two, the simple U-Net with data augmentation performs better than the original but not quite as efficiently as the pre-trained model. Shapes are more correctly defined than in the original, but there are still missing information and badly shaped instances. Below, some more predictions from the final model are shown in Figure 3.18, to give a more general view on its performance.

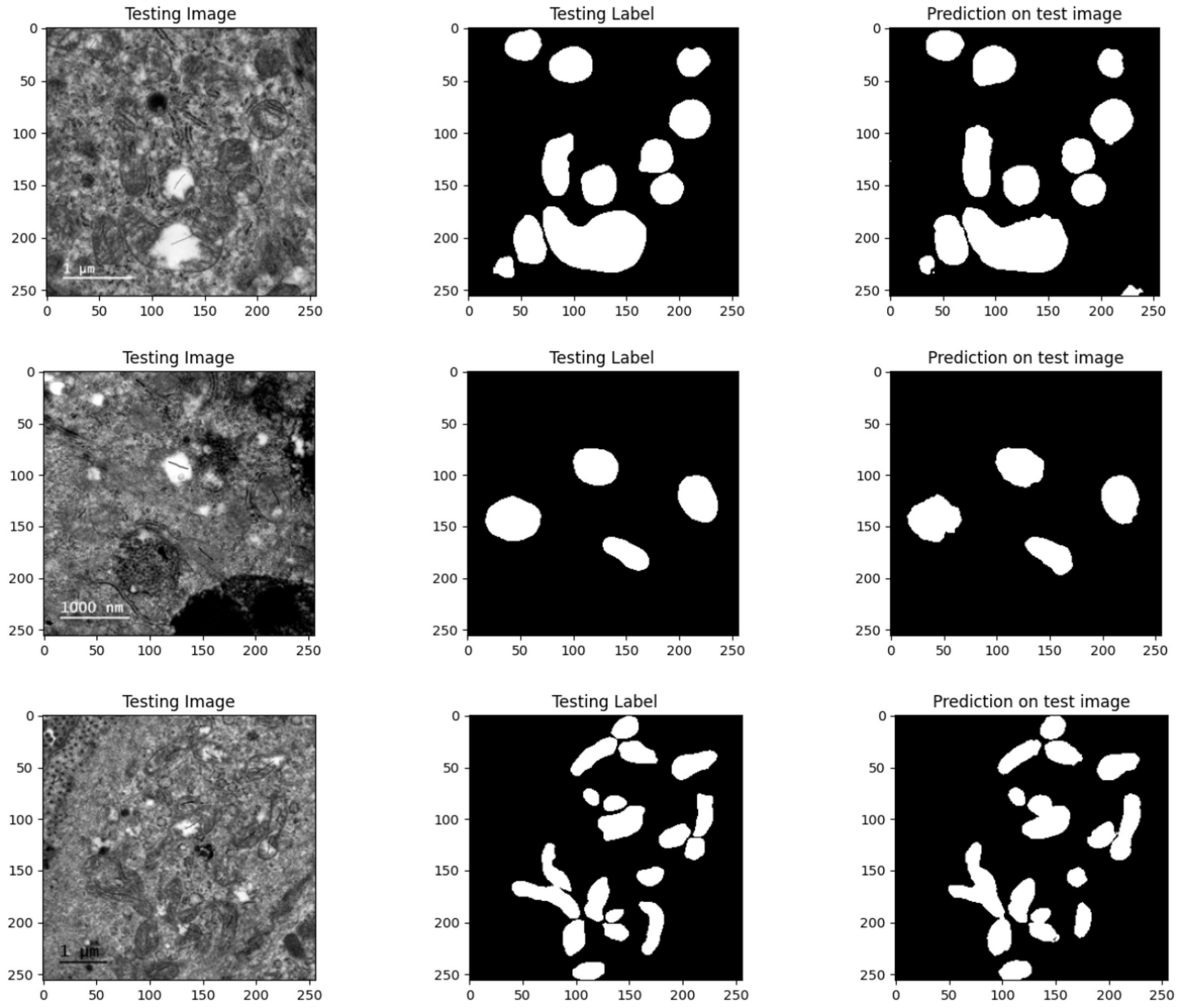

Figure 3.18. Random samples along with predictions from the final model.

Chapter 4: Conclusion

FLASH radiotherapy is a promising cancer treatment that has demonstrated better sparing of the normal tissues surrounding the tumor, compared to conventional dose rate. However, whether the FLASH effect is still present in proton radiation is a question that remains to be answered. More studies are needed in this direction, mainly to decipher the role of hypoxia in the manifestation of the FLASH effect, to define the precise timepoints that the various effects (like the increase in area of the mitochondria) take place and to quantify the actual difference from the conventional dose rate, if it exists. As for the segmentation model, although the results are quite satisfying, several steps can be made for its improvement. By training it in a larger dataset, its accuracy would be enhanced and IoU could probably reach a value equivalent with that of the state-of-the-art models. In addition, a next-level implementation could be a multi-class semantic segmentation (for example to normal and damaged mitochondria). Such an amendment could save precious time to the researchers. It could also possibly reveal new insights into the morphological differences between normal and damaged mitochondria, for example differences not visible in the human eye. What is for sure, is that there are definitely a lot of opportunities and future prospects on this field.

References

[1] Tremi I. (2022). “*Biological response of human cancer cells to ionizing radiation in combination with gold nanoparticles*” [Doctoral dissertation, National and Technical University of Athens],(Publication: https://doi.org/10.3390/cancers14205086)

[2] Griffiths, D. (2020). *Introduction to elementary particles*. John Wiley & Sons.

[3] Buckley, M. (2002). the Compton effect.

[4] Manninen, A.-L. (2014). CLINICAL APPLICATIONS OF RADIOPHOTOLUMINESCENCE (RPL) DOSIMETRY IN EVALUATION OF PATIENT RADIATION EXPOSURE IN RADIOLOGY Determination of absorbed and effective dose. (https://www.researchgate.net/publication/298709741)

[5] Chang, D. S., Lasley, F. D., Das, I. J., Mendonca, M. S., & Dynlacht, J. R. (2021). *Basic Radiotherapy Physics and Biology.* doi:10.1007/978-3-030-61899-5

[6] Byun, H. K., et al. (2021). "Physical and Biological Characteristics of Particle Therapy for Oncologists." Cancer Res Treat **53**(3): 611-620.

[7] Mohan, R. (2022). "A Review of Proton Therapy - Current Status and Future Directions." Precis Radiat Oncol **6**(2): 164-176.

[8] Lin, B., et al. (2021). "FLASH Radiotherapy: History and Future." Frontiers in Oncology **11**.

[9] Hughes, J. R. and J. L. Parsons (2020). "FLASH Radiotherapy: Current Knowledge and Future Insights Using Proton-Beam Therapy." Int J Mol Sci **21**(18).

[10] Buonanno, M.; Grilj, V.; Brenner, D.J. Biological effects in normal cells exposed to FLASH dose rate protons. Radiother. Oncol. 2019, 139, 51–55.

[11] Simmons, D.A.; Lartey, F.M.; Schuler, E.; Rafat, M.; King, G.; Kim, A.; Ko, R.; Semaan, S.; Gonzalez, S.; Jenkins, M.; et al. Reduced cognitive deficits after FLASH irradiation of whole mouse brain are associated with less hippocampal dendritic spine loss and neuroinflammation. Radiother. Oncol. 2019, 139, 4–10.

[12] Gaide, O., et al. (2022). "Comparison of ultra-high versus conventional dose rate radiotherapy in a patient with cutaneous lymphoma." Radiother Oncol **174**: 87-91.

[13] Colangelo, N.W.; Azzam, E.I. The Importance and Clinical Implications of FLASH Ultra-High Dose-Rate Studies for Proton and Heavy Ion Radiotherapy. Radiat. Res. 2020, 193, 1–4

[14] Levy, K., et al. (2020). "Abdominal FLASH irradiation reduces radiation-induced gastrointestinal toxicity for the treatment of ovarian cancer in mice." Sci Rep **10**(1): 21600.

[15] Ruan JL, Lee C, Wouters S, Tullis IDC, Verslegers M, Mysara M, Then CK, Smart SC, Hill MA, Muschel RJ, Giaccia AJ, Vojnovic B, Kiltie AE, Petersson K. “Irradiation at Ultra-High (FLASH) Dose Rates Reduces Acute Normal Tissue Toxicity in the Mouse Gastrointestinal System.” Int J Radiat Oncol Biol Phys. 2021 Dec 1;111(5):1250-1261. doi: 10.1016/j.ijrobp.2021.08.004. Epub 2021 Aug 14. PMID: 34400268; PMCID: PMC7612009.

[16] Rao, R., et al. (2020). "Comparison of FLASH vs Conventional Dose Rate Proton Radiation in Endogenous Mouse Brain Tumor Model." International Journal of Radiation Oncology, Biology, Physics **108**(3): e742.

[17] Lowe, J. S., Anderson, P. G., & Anderson, S. I. (2023). *Stevens & Lowe's Human Histology-E-Book: Stevens & Lowe's Human Histology-E-Book*. Elsevier Health Sciences.

[18] Cordova, E.D.M. (2022, March 1). “Why is histology important?.” *Get a Professor*, https://getaprofessor.com/2022/03/01/why-is-histology-important/.

[19] Rogers, Kara. "mitochondrion". *Encyclopedia Britannica*, 23 Aug. 2024, https://www.britannica.com/science/mitochondrion. Accessed 7 September 2024.

[20] Somosy, Z. (2000). *Radiation response of cell organelles. Micron, 31(2), 165–181*. doi:10.1016/s0968-4328(99)00083-9

[21] Payne, C.M., Bjore, C.G., Schultz, D.A., 1992. Change in the frequency of apoptosis after low- and high-dose X-irradiation of human lymphocytes. Journal of Leukocyte Biology 52, 433–440.

[22] Petit, P.X., Lecoeur, H., Zorn, E., Dauguet, C., Mignotte, B., Gougeon, M.L., 1995. Alterations in mitochondrial structure and function are early events of dexamethasone-induced thymocyte apoptosis. Journal of Cell Biology 130, 157–167.

[23] Somosy, Z., et al. (2002). "Morphological aspects of ionizing radiation response of small intestine." Micron **33**(2): 167-178.

[24] Yago, N., Sekiyama, S., Kurokawa, H., Iwai, Y., Sato, F., Shiragai, A., 1972. A stereological study on size and number of mitochondria in zone fasciculata of rat adrenal cortex after whole-body X-irradiation. International Journal of Radiation Biology 21, 1–10.

[25] Somosy, Z., et al. (1996). "X-irradiation-induced changes of the prelysosomal and lysosomal compartments and proteolysis in HT-29 cells." Scanning Microscopy 10, 1079-1091.

[26] Baatout, S. (Ed.). (2023). *Radiobiology textbook*. Cham, Switzerland: Springer International Publishing.

[27] Singh A and Singh H. Time-scale and nature of radiationbiological damage: approaches to radiation protection and post-irradiation therapy. Prog Biophys Mol Biol 39: 69– 107, 1983

[28] Reisz, J. A., et al. (2014). "Effects of ionizing radiation on biological molecules--mechanisms of damage and emerging methods of detection." Antioxid Redox Signal **21**(2): 260-292.

[29] Mavragani, I.V.; Nikitaki, Z.; Souli, M.P.; Aziz, A.; Nowsheen, S.; Aziz, K.; Rogakou, E.; Georgakilas, A.G. Complex DNA Damage: A Route to Radiation-Induced Genomic Instability and Carcinogenesis. *Cancers* **2017**, *9*, 91. https://doi.org/10.3390/cancers9070091

[30] Luitel, K., Bozeman, R., Kaisani, A., Kim, S. B., Barron, S., Richardson, J. A., & Shay, J. W. (2018). *Proton radiation-induced cancer progression. Life Sciences in Space Research.* doi:10.1016/j.lssr.2018.08.002

[31] Janiesch, C., Zschech, P., & Heinrich, K. (2021). *Machine learning and deep learning. Electronic Markets.* doi:10.1007/s12525-021-00475-2

[32] Badillo, S., Banfai, B., Birzele, F., Davydov, I. I., Hutchinson, L., Kam-Thong, T., ... Zhang, J. D. (2020). *An Introduction to Machine Learning. Clinical Pharmacology & Therapeutics.* doi:10.1002/cpt.1796

[33] Vieira, S., Garcia-Dias, R., & Lopez Pinaya, W. H. (2020). *A step-by-step tutorial on how to build a machine learning model. Machine Learning, 343–370.* doi:10.1016/b978-0-12-815739-8.00019-5

[34] Diffenderfer, E. S. et al. Design, Implementation, and in Vivo Validation of a Novel Proton FLASH Radiation Therapy System. Int. J. Radiat. Oncol. Biol. Phys. 106, 440–448 (2020).

[35] Project Jupyter, Home 2024, accessed August 31, 2024, < https://jupyter.org/ >

[36] Bhattiprolu, S. (2021, May 5). 216 - Semantic segmentation using a small dataset for training (& U-Net) [Video]. YouTube. https://youtu.be/-XeKG_T6tdc?feature=shared

[37] Krithika alias AnbuDevi, M. and K. Suganthi (2022). "Review of Semantic Segmentation of Medical Images Using Modified Architectures of UNET." Diagnostics **12**(12): 3064.

[38] Ronneberger, O., Fischer, P., Brox, T. (2015). U-Net: Convolutional Networks for Biomedical Image Segmentation. In: Navab, N., Hornegger, J., Wells, W., Frangi, A. (eds) Medical Image Computing and Computer-Assisted Intervention – MICCAI 2015. MICCAI 2015. Lecture Notes in Computer Science(), vol 9351. Springer, Cham. <https://doi.org/10.1007/978-3-319-24574-4_28>

[39] Dotmatics. “T test Calculator.” *GraphPad*,

https://www.graphpad.com/quickcalcs/ttest1.cfm. Accessed 8 September 2024.

[40] Guo, Z.; Buonanno, M.; Harken, A.; Zhou, G.; Hei, T.K. Mitochondrial Damage Response and Fate of Normal Cells Exposed to FLASH Irradiation with Protons. *Radiat. Res.* **2022**, *197*, 569–582.

[41] Han, J.; Mei, Z.; Lu, C.; Qian, J.; Liang, Y.; Sun, X.; Pan, Z.; Kong, D.; Xu, S.; Liu, Z.; et al. Ultra-High Dose Rate FLASH Irradiation Induced Radio-Resistance of Normal Fibroblast Cells Can Be Enhanced by Hypoxia and Mitochondrial Dysfunction Resulting From Loss of Cytochrome C. *Front. Cell Dev. Biol.* **2021**, *9*, 672929.

[42] Bogaerts, E., et al. (2022). "Potential Molecular Mechanisms behind the Ultra-High Dose Rate “FLASH” Effect." International Journal of Molecular Sciences **23**(20): 12109.

[43] Dotmatics. “P value Calculator.” *GraphPad*,

https://www.graphpad.com/quickcalcs/pvalue1.cfm. Accessed 10 September 2024.

[44] Betzold, J.M., Saeger, W., Ludecke, D.K., 1992. Ultrastructural-morphometric effects of radiotherapy on pituitary adenomas in acromegaly. Experimental and Clinical Endocrinology 100, 106–111.

[45] Maeda, S., 1982. Pathology of experimental radiation pancarditris. II. Correlation between ultrastructural changes of the myocardial mitochondria and succinic dehyrogenase activity in rabbit heart receiving a single dose of X-ray irradiation. Acta Pathologica Japonica 32, 199– 218.

[46] van Beers, F.; Lindström, A.; Okafor, E. and Wiering, M. (2019). **Deep Neural Networks with Intersection over Union Loss for Binary Image Segmentation**. In *Proceedings of the 8th International Conference on Pattern Recognition Applications and Methods - ICPRAM*; ISBN 978-989-758-351-3; ISSN 2184-4313, SciTePress, pages 438-445. DOI: 10.5220/0007347504380445

[47] Oztel, I., Yolcu, G., Ersoy, I., White, T., & Bunyak, F. (2017). *Mitochondria segmentation in electron microscopy volumes using deep convolutional neural network. 2017 IEEE International Conference on Bioinformatics and Biomedicine (BIBM).* doi:10.1109/bibm.2017.8217827

[48] Hendee, W.R., Zebrun, W., Bonte, F.J., 1963. Effects of X-irradiation on fine structure of HeLa cells. Texas Reports on Biology and Medicine 21, 546–557.

Appendix I

Table 1: Average percentages of mitochondria per μm^2, with their variances and standard errors.

	(%)	CONVENTIONAL	FLASH
		30 minutes	
normal	Average	90.03	83.98
	Variance	2.00	2.50
	St. Error	±3.00	±4.60
damaged	Average	9.86	15.96
	Variance	2.00	2.50
	St. Error	±3.00	±4.60
		4 hours	
normal	Average	60.82	65.90
	Variance	5.00	3.00
	St. Error	±5.00	±6.20
damaged	Average	39.12	34.00
	Variance	5.00	3.00
	St. Error	±5.00	±6.20
		18 hours	
normal	Average	31.00	38.00
	Variance	7.00	7.50
	St. Error	±5.00	±5.70
damaged	Average	68.93	61.67
	Variance	7.00	7.50
	St. Error	±5.00	±5.70

Table 2: Average areas of mitochondria, with their variances and standard errors.

	(μm^2)	CONVENTIONAL	FLASH
		30 minutes	
normal	Average	0.15	0.23
	Variance	0.006	0.024
	St. Error	±0.02	±0.04
damaged	Average	0.25	0.43
	Variance	0.037	0.088
	St. Error	±0.05	±0.07
		4 hours	
normal	Average	0.17	0.26
	Variance	0.003	0.035
	St. Error	±0.01	±0.04
damaged	Average	0.32	0.31
	Variance	0.025	0.030
	St. Error	±0.04	±0.04
		18 hours	
normal	Average	0.21	0.18
	Variance	0.015	0.019
	St. Error	±0.03	±0.03
damaged	Average	0.38	0.34
	Variance	0.027	0.041
	St. Error	±0.03	±0.04

Appendix II

The complete code used for the Mitochondria Segmentation task is presented below. The data pipeline and model evaluation are heavily inspired by the work of Dr Sreenivas Bhattiprolu [36].

```
import os
import cv2
from PIL import Image
import numpy as np
from matplotlib import pyplot as plt


image_directory = 'E:\\Electron Microscopy Photos\\diplomatiki\\Image_folder'
mask_directory = 'E:\\Electron Microscopy Photos\\diplomatiki\\Mask_folder'

# Data pre-processing

SIZE = 256  #dimension of resizing
image_dataset = []  #empty lists to store the processed data
mask_dataset = []

images = os.listdir(image_directory)
for i, image_name in enumerate(images):
    if (image_name.split('.')[1] == 'tif'):

        image_path = os.path.join(image_directory, image_name)
        image = cv2.imread(image_path, 3)

        # Check if the image was correctly read
        if image is None:
            print(f"Error reading image: {image_name}")
            continue

        image = Image.fromarray(image)
        image = image.resize((SIZE, SIZE))
        image_dataset.append(np.array(image))

#Iterate through all images in Uninfected folder, resize to 64 x 64
#Then save into the same numpy array 'dataset' but with label 1

masks = os.listdir(mask_directory)
for i, mask_name in enumerate(masks):
    if (mask_name.split('.')[1] == 'tif'):
        mask_path = os.path.join(mask_directory, mask_name)
        mask = cv2.imread(mask_path, 0)

        # Ensure that the mask is binary
        _, mask = cv2.threshold(mask, 127, 1, cv2.THRESH_BINARY)

        mask = Image.fromarray(mask)
        mask = mask.resize((SIZE, SIZE))
        mask_dataset.append(np.array(mask))

#making images an numpy array
image_dataset = np.array(image_dataset)
#same for masks, but we expand one dimension to include channel
mask_dataset = np.expand_dims(np.array(mask_dataset), 3)
print(f"Total images: {len(image_dataset)}, Total masks: {len(mask_dataset)}")
```

```
#inspection of the data after pre-processing

print(image_dataset.shape)
print(mask_dataset.shape)
print("Pixel values in the mask are: ", np.unique(mask_dataset))

#importing segmentation models class from keras

import segmentation_models as sm

BACKBONE = 'resnet34' # defining the pre-trained network
preprocess_input1 = sm.get_preprocessing(BACKBONE)

# preprocess (normalize) input images to suit the requirements of the network

images1=preprocess_input1(image_dataset)

#train-test split

from sklearn.model_selection import train_test_split
X_train, X_test, y_train, y_test = train_test_split(images1,
                                                    mask_dataset,
                                                    test_size = 0.25,
                                                    random_state = 42)


#Sanity check, view few mages

import random
import numpy as np
image_number = random.randint(0, len(X_train))
plt.figure(figsize=(12, 6))
plt.subplot(121)
plt.imshow(X_train[image_number, :,:, 0], cmap='gray')
plt.subplot(122)
plt.imshow(np.reshape(y_train[image_number], (256, 256)), cmap='gray')
plt.show()

#Defining dictionaries to be used as inputs to image generator

seed=24
from keras.preprocessing.image import ImageDataGenerator

img_data_gen_args = dict(rotation_range=90,
                     width_shift_range=0.3,
                     height_shift_range=0.3,
                     shear_range=0.5,
                     zoom_range=0.3,
                     horizontal_flip=True,
                     vertical_flip=True,
                     fill_mode='reflect')

mask_data_gen_args = dict(rotation_range=90,
                     width_shift_range=0.3,
                     height_shift_range=0.3,
                     shear_range=0.5,
                     zoom_range=0.3,
                     horizontal_flip=True,
                     vertical_flip=True,
                     fill_mode='reflect',
```

```
                     preprocessing_function = lambda x: np.where(x>0, 1, 0).astype(x.
dtype)) #Binarize the output again.

# Defining image and mask generators for training and testing.

image_data_generator = ImageDataGenerator(**img_data_gen_args)

train_image_generator = image_data_generator.flow(X_train, seed=seed)
valid_img_generator = image_data_generator.flow(X_test, seed=seed)

mask_data_generator = ImageDataGenerator(**mask_data_gen_args)

train_mask_generator = mask_data_generator.flow(y_train, seed=seed)
valid_mask_generator = mask_data_generator.flow(y_test, seed=seed)

# Combine the generators for images and masks to a single generator

def combined_image_mask_generator(image_generator, mask_generator):
    train_generator = zip(image_generator, mask_generator)
    for (img, mask) in train_generator:
        yield (img, mask)

combined_train_generator = combined_image_mask_generator(train_image_generator,
                                                         train_mask_generator)

combined_validation_generator = combined_image_mask_generator(valid_img_generator,
                                                              valid_mask_generator)

x = train_image_generator.next()
y = train_mask_generator.next()
for i in range(0,1):
    image = x[i]
    mask = y[i]
    plt.subplot(1,2,1)
    plt.imshow(image[:,:,0], cmap='gray')
    plt.subplot(1,2,2)
    plt.imshow(mask[:,:,0])
    plt.show()

# define the model using pre-trained weights

model = sm.Unet(BACKBONE, encoder_weights='imagenet')
model.compile('Adam', loss=sm.losses.bce_jaccard_loss, metrics=[sm.metrics.iou_score]
)
print(model.summary())

#Fit the model
history = model.fit(combined_train_generator,
                    validation_data=combined_validation_generator,
                    steps_per_epoch=50,
                    validation_steps=50, epochs=50)
model.save('my_model.h5')

#plot the training and validation accuracy and loss at each epoch
loss = history.history['loss']
val_loss = history.history['val_loss']
epochs = range(1, len(loss) + 1)
plt.plot(epochs, loss, 'y', label='Training loss')
plt.plot(epochs, val_loss, 'r', label='Validation loss')
plt.title('Training and validation loss')
plt.xlabel('Epochs')
plt.ylabel('Loss')
```

```
plt.legend()
plt.show()



acc = history.history['iou_score']
#acc = history.history['accuracy']
val_acc = history.history['val_iou_score']
#val_acc = history.history['val_accuracy']

plt.plot(epochs, acc, 'y', label='Training IOU')
plt.plot(epochs, val_acc, 'r', label='Validation IOU')
plt.title('Training and validation IOU')
plt.xlabel('Epochs')
plt.ylabel('IOU')
plt.legend()
plt.show()

#IOU
y_pred=model.predict(X_test)
y_pred_thresholded = y_pred > 0.5

intersection = np.logical_and(y_test, y_pred_thresholded)
union = np.logical_or(y_test, y_pred_thresholded)
iou_score = np.sum(intersection) / np.sum(union)
print("IoU socre is: ", iou_score)

test_img_number = random.randint(0, len(X_test)-1)
test_img = X_test[test_img_number]
test_img_input=np.expand_dims(test_img, 0)
ground_truth=y_test[test_img_number]
prediction = model.predict(test_img_input)
prediction = prediction[0,:,:,0]

# Binarize the prediction
threshold = 0.7
binary_prediction = (prediction >= threshold).astype(np.uint8)

plt.figure(figsize=(16, 8))
plt.subplot(231)
plt.title('Testing Image')
plt.imshow(test_img[:,:,0], cmap='gray')
plt.subplot(232)
plt.title('Testing Label')
plt.imshow(ground_truth[:,:,0], cmap='gray')
plt.subplot(233)
plt.title('Prediction on test image')
plt.imshow(binary_prediction, cmap='gray')

plt.show()
```